Spherical Surface Parameterization and its Application to Geometric Morphometric Analysis of the Braincase

---

Dissertation

zur

Erlangung der naturwissenschaftlichen Doktorwürde
(Dr. sc. nat.)

vorgelegt der

Mathematisch-naturwissenschaftlichen Fakultät

der

Universität Zürich

von

Matthias Specht

von

Flawil SG

Promotionskomitee

Prof. Dr. Christoph Zollikofer (Vorsitz, Leiter der Dissertation)
Prof. Dr. Renato Pajarola
Prof. Dr. Carel van Schaik
Prof. Dr. Hugo Bucher
Prof. Dr. Pete Lestrel

Zürich, 2007

Die vorliegende Arbeit wurde von der Mathematisch-naturwissenschaftlichen Fakultät der Universität Zürich auf Antrag von Prof. Dr. Christoph Zollikofer, Prof. Dr. Renato Pajarola und Prof. Dr. Pete Lestrel als Dissertation angenommen.

Abstract

The quantitative comparison of the form of the endocast, which is the internal surface of the braincase, is one of the central issues in paleoanthropology (i.e., the study of human evolution based on fossil evidence). The major difficulty is that there are only few anatomical locations (so-called landmarks) defining biological correspondence between individual endocasts. Such point homologies, however, are the basis of the most powerful methods of morphometric analysis, the geometric morphometric toolbox. As a consequence, methods of geometric morphometrics are only of limited use in the analysis of endocranial form, and the morphometric analysis of such three-dimensional surfaces, which are poor in landmarks, is an open and lively discussed problem.

In a quite different field, computer graphics, the parameterization of a surface embedded in the space $\mathbb{R}^3$ is a well-known problem. For that purpose, the surface is mapped onto a two-dimensional parameter domain such as the plane or the sphere. The parameterization of a triangulated surface is a basic step in many applications in the area of geometry processing such as texture mapping, morphing, remeshing and data compression. Conformal, i.e., angle-preserving parameterizations, represents a special case.

This thesis uses these techniques and methods to propose a new approach to the problem of quantitative comparison of endocranial surfaces with only few point homologies. For this purpose, concepts from geometric morphometrics are fused with concepts from computer graphics. Triangulated endocranial surfaces are conformally mapped to the unit sphere. The resulting spherical parameterizations are calibrated according to user-defined biological constraints. The result is a consistent coordinate system: a position on the unit sphere corresponds to a biologically homologous position on each surface in the sample. The sphere is a well-known, two-dimensional domain, and spherical functions can be expanded into a series of spherical harmonic functions. Thereby, a three-dimensional Fourier descriptor is produced, which permits shape analysis in frequency space.

The integration of the new surface representations into the software *MorphoTools* permits the various statistical analyses, scientific visualization of the results and comparison with classic geometric morphometric methods. To test the new method, neurocrania of humans and great apes (gorillas, chimpanzees and bonobos) are analyzed.

Keywords: Scientific Visualization, Surface Parameterization, Geometric Morphometrics, Morphing, Brain, Endocast, Conformal Map, Spherical Parameterization, Computer-Assisted Paleoanthropology.

Kurzfassung

Der quantitative Vergleich der Form des Neuroendocraniums (Innenfläche des Hirnschädels; "Endocast"; Endocranium) ist ein zentrales Problem in der Paläoanthropologie (d.h. der Erforschung der menschlichen Evolution anhand fossiler Funde). Das Hauptproblem dabei ist, dass es nur wenige anatomische Fixpunkte (sog. Landmarken) auf dem Neurocranium gibt, die biologische Übereinstimmung zwischen individuellen Neurocrania definieren. Die leistungsstärksten Methoden der Geometrischen Morphometrie basieren allerdings auf solchen Punkthomologien und können deshalb nicht, oder nur bedingt, angewendet werden. Die biologische Analyse solcher dreidimensionalen Oberflächen, die arm an Landmarken sind, ist ein Problem, für das es bisher noch keine befriedigende Lösung gibt und das zurzeit rege diskutiert wird.

In einem ganz anderen Forschungsgebiet, der Computergrafik, ist die Parametrisierung einer Fläche, die im Raum $\mathbb{R}^3$ eingebettet ist, ein wohlbekanntes Problem. Die Fläche wird dazu auf einen geeigneten zweidimensionalen Parameterraum, wie z.B. die Ebene oder die Sphäre, abgebildet. Die Parametrisierung einer triangulierten Oberfläche ist grundlegend für viele Anwendungen im Bereich Geometry-Processing, wie Texture Mapping, Morphing, Remeshing und Datenkompression. Ein Spezialfall sind konformale (d.h. winkeltreue) Abbildungen.

Die vorliegende Arbeit befasst sich mit der Anwendung dieser Techniken und Methoden auf das Problem, Oberflächen mit nur wenigen Punkthomologien quantitativ und biologisch relevant zu vergleichen. Dazu werden Konzepte aus der Geometrischen Morphometrie und aus der Computergrafik verschmolzen. Triangulierte endocraniale Oberflächen werden konformal auf die Einheitssphäre abgebildet. Die sphärischen Parametrisierungen werden unter Einbezug von biologischen Bedingungen kalibriert. Das Resultat ist ein einheitliches Koordinatensystem: Eine bestimmte Position auf der Einheitskugel entspricht biologisch derselben Position auf jeder der zu vergleichenden Flächen. Die Sphäre ist eine wohlbekannte zweidimensionale Domäne, und sphärische Funktionen lassen sich in eine Reihe von sphärischen harmonischen Funktionen entwickeln. Dadurch wird ein dreidimensionaler Fourierdeskriptor erzeugt, der die Gestaltanalyse im Frequenzraum erlaubt.

Die Einbindung der neuen Oberflächenrepräsentationen in die Software *MorphoTools* ermöglicht die Anwendung statistischer Analysen, wissenschaftliche Visualisierungen der Resultate sowie den Vergleich mit rein landmarkbasierten Methoden. Als Test für die neue Methode werden Neurocrania von Menschen und Menschenaffen (Gorillas, Schimpansen und Zwergschimpansen) analysiert.

Acknowledgments

This work started out at the MultiMedia Laboratory (MML) of the Computer Science Department of the University of Zürich with Prof. Dr. Peter Stucki as a co-initiator of the project, and continued and finished at the Morpholab of the Anthropological Institute of the University of Zürich. I thank Prof. Dr. Christoph Zollikofer, who founded the Morpholab during my PhD studies, for his constant support of my work. Together with Dr. Marcia Ponce de León, he "modernized" paleoanthropology, laying foundation to the new research field named *computer-assisted paleoanthropology*, and his own relaxed but serious way of approaching scientific problems has been a constant source of inspiration for me.

I thank Renaud Lebrun for the very fruitful collaboration on MorphoTools, and for his help with endocast segmentation and landmark annotation. Dr. Jody Weissmann was helping me a lot whenever I was lost in mathematical problems, and I owe him big time.

My thanks go to Dr. Joan Glaunès, which provided his source code for calculating deformations on the sphere.

I thank all my colleagues at the Morpholab for providing a stimulating and lively working environment, and for the very interesting and often completely off-topic discussions: Peter Holdener, Dr. Tea Jashashvili, Dr. Juan Manuel Jiménez-Arenas, Walther Fuchs, Fabian Hilti, Naoki Morimoto, Dr. Kristian Carlson and Susanne Suter.

Particular thanks are due to my friends from the Corebounce Association, Pascal Müller, Dr. Stefan Müller Arisona and Dr. Simon Schubiger-Banz. They always helped me with scientific and academic advice when I needed it, and the late-night coding and paper writing sessions and live performances proved that science can be fun.

This work would not have been possible without the constant support from my wife, Diana. She and our daughter Lara Valentina made sure I don't forget the "real life" out there.

Finally, I thank my parents, who always supported me and have been there when I needed them.

This work was financially supported in part by Swiss NSF grants 205321-102024/1 and 205320-109303/1, and the A. H. Schultz foundation.

Contents

Chapter 1

Introduction

Two major features discriminate our own species *(Homo sapiens)* from our closest living relatives, the chimpanzees *(Pan troglodytes)* and the bonobos *(Pan paniscus)*: we walk on two legs and have comparatively big brains. It is still a matter of debate how and why during human evolution brain size was increased, and what is the principal difference between a human and a chimpanzee brain, or between the braincase of a fossil hominid and a modern human. One important prerequisite to tackle these questions is to quantify the internal form of the bony case containing the brain, the so-called cranial *endocast* (see figure 1.1), because the braincase is the only comparative data source in fossil humans and in ape specimens housed in collections worldwide.

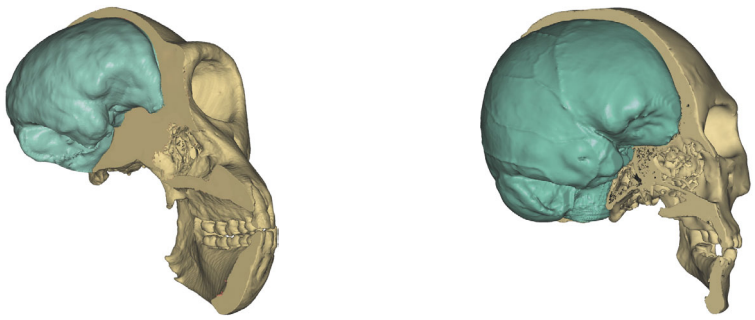

Figure 1.1: Brain endocasts. The endocasts (light green) of a chimpanzee braincase (left) and the one of a modern human (right).

Quantification and comparison of biological form, especially that of the endocast, is a notoriously difficult task. This is because the geometry of biological forms is typically more complex than that of standard Euclidean bodies and graphic primitives, such that classical ruler-based measurements - e.g., linear distances between reference points - only capture a small fraction of the relevant morphological information. Free-form object

representation by surface triangulation into a triangle mesh is an important first step to quantify biomedical objects (Hemmy et al., 1994). However, once we have reconstructed a series of endocranial free-form surfaces, how can we perform quantitative comparative analyses of their shape?

Any biologically sensible comparison relies on the definition of so-called homology relationships (Rieppel, 1989). Homology denotes biological equivalence through evolutionary and developmental history. For example, the left half of braincase A is homologous to the left half of braincase B, and a point on the tip of the nose of individual A is homologous to the tip of the nose of individual B. Interestingly, close analogies exist between the definition of homology in biology and the concept of parameterization in computer graphics, and as a matter of fact, such parallels have been exploited fruitfully during the past decade (Zollikofer et al., 1995, 1998). For example, defining a set of three-dimensional anatomical points of reference (landmarks) on a skull A, and defining a homologous point set on a second skull B permits definition of a three-dimensional spline function that morphs skull A into skull B. This spline function thus quantifies the biologically relevant difference in form between the two skulls and can be used to visualize local versus global differences in the form of the two objects (Bookstein, 1989a).

Measuring and comparing biological form with the aid of a spline is a fundamental concept that gave rise to the rapidly expanding field of geometric morphometrics (Bookstein, 1991). Compared to traditional morphometrics, the new methods are much more powerful for statistical shape analysis and permit visualization of results directly in the original space of the organisms instead of abstract multivariate space (Rohlf and Marcus, 1993; Adams et al., 2004). Geometric morphometric methods became popular in various biological research areas, for instance in paleoanthropology, where the new research field of *computer-assisted paleoanthropology* emerged (Zollikofer et al., 1995, 1998).

However, landmark-based geometric-morphometric comparisons between biological shapes have their limitations. Landmarks are typically defined at meeting points between three or more adjacent structures (type I), or at extremal locations (type II) (Bookstein, 1990, 1991). While, for example, the face or facial skeleton of humans and apes is rich in well-defined anatomical landmarks such as the tip of the nose, the center of the eye, meeting points between cranial structures, foramina etc., the braincase and even the brain itself is not. Establishing point-to-point correspondence between endocranial surfaces is difficult for various reasons. First, only few type I/II landmarks can be identified on the cranial vault, both inside and outside. Second, the relationship between endocranial structures and structures of the brain surface is often unknown. And third, established methods of brain mapping (establishment of a homology atlas) rely upon different definitions of biological correspondence relationships, e.g., through developmental homology or through functional equivalence (Van Essen, 2002).

One approach to tackle this problem is to fill landmark-depleted regions with additional points of reference, so-called semilandmarks, that are defined according to ad-hoc geometric criteria (Bookstein, 1997; Andresen and Nielsen, 2001). While such analyses convey more information about the geometry of the objects under investigation, it remains unclear whether this adds to the biologically relevant information.

An opposite approach consists in applying landmark-free methods, which compare

forms by quantifying non-localized differences between them. A classic instance is elliptic Fourier analysis (EFA) (Kuhl and Giardina, 1982), in which a closed outline in two or three dimensions is described by the Fourier spectrum of the *x,y(,z)*-components of a path (or its first derivative) along the outline. These methods are well-suited to compare biological forms on which locations of homology between specimen are difficult to define (Lestrel, 1997). As a tradeoff, however, form differences identified with EFA are difficult to interpret in terms of biological difference, because it is no longer possible to determine where exactly on the morphology the relevant differences between forms are located.

The aim of this thesis is to develop morphometric methods that unite the strengths of landmark and semilandmark-based approaches with the strengths of the Fourier approach in order to establish mathematically and biologically consistent quantitative descriptions of the morphology of endocranial surfaces.

The geometric morphometrics toolbox is so far lacking a method to apply a Fourier analysis to a *surface*. However, in the fields of *computer graphics* and *computer vision*, solutions for this problem do exist (Brechbühler et al., 1992). The fundamental step is to parameterize the surface on a convenient parameter domain (such as the plane or the unit sphere). Mesh parameterization is important for many applications in geometry processing, including texture mapping, morphing, remeshing, data compression and shape analysis (Sheffer et al., 2006). In mesh parameterization, the main objective is to find a continuous invertible mapping between the mesh surface and the parameter domain, which minimizes the distortion incurred in the transition in some meaningful sense (Floater and Hormann, 2005). An example is creating geographic maps. A variety of mapping methods exist with different properties. For instance, the Mercator projection, often used to draw world maps, preserves angles, but not areas, resulting in extreme area distortion at the poles (i.e., Greenland and Antarctica are drawn much too large). The Lambert projection preserves areas at the cost of giving up the preservation of angles. Visually speaking, there is an interesting connection between texturing a surface with minimal distortion and parameterizing a biological surface with minimal error.

Of special concern here are *conformal* mappings, which minimize angular distortion, and the concept of *consistent mesh parameterization*, i.e., the simultaneous parameterization of several surfaces on a common parameter domain such that a given set of user-specified features match. A consistent parameterization introduces a common coordinate system on all surfaces and the parameter domain. If the parameter domain is a natural and well-studied mathematical space, in our case the unit sphere, it is straight-forward to sample the surfaces over the domain in any desired fashion and apply established function analysis methods to compare the surfaces. Of special interest is the expansion of the spherical signals describing the surface in 3D space into a Fourier series of spherical harmonics.

In this thesis, I specifically examine how concepts of mesh parameterization can be combined with concepts of geometric morphometrics to obtain consistent quantitative descriptions of relatively "featureless" structures which are homeomorphic to the sphere (i.e., genus-zero surfaces) such as the braincase. I combine the advantages of homology-driven landmark-based analysis with the advantages of landmark-free approaches, resulting in a surface analysis pipeline whose biological significance is proportional to the ho-

mology information incorporated during the data sampling process.

1.1 Geometric Morphometrics Pipeline

Let us look at the processes involved in a typical geometric morphometric analysis in a more formal way. Figure 1.2**A** gives a schematic overview of a landmark-based analysis. Three major steps may be discerned:

Sampling. In computer-assisted paleoanthropology, the most common data sources are volumetric data sets obtained with *computer tomography* (CT). Usually the structures contained in the volume data are segmented into triangle meshes representing surfaces, and biological information is introduced by manually determining homologous points (landmarks) on the surfaces. Only the coordinates of the landmarks are then used for further analyses, while between-landmark regions are not considered.

Analysis. For landmark data, two approaches exist to perform comparisons. The first is based on superimposing the landmark configurations in a common coordinate system (Rohlf, 1990; Bookstein, 1991), and the other is based on sets of inter-landmark distances, not requiring a common coordinate system (Lele and Richtsmeier, 1991). In both cases, the next step is to apply statistical methods to detect patterns of shape variability in the sample.

Visualization. The main advantage of using a common coordinate system is that, if the statistical analysis method is invertible, results obtained in feature space can be re-transformed and visualized in real space. However, the landmarks only contain a small fraction of the geometric information contained in the segmented surfaces. Landmarks can be connected to form wireframe visualizations (O'Higgins and Jones, 1998) which are coarse approximations of the actual shapes. A powerful tool to visualize patterns of shape variation are thin plate splines (TPS) (Bookstein, 1989a). Any of the original surfaces can be deformed such that the source landmarks match a target configuration (typically a point in feature space, such as the consensus or a position along a trajectory). However, because of the *a posteriori* nature of this deformation, each of the original surfaces deforms to a slightly different solution, thus this choice is an arbitrary one.

1.2 The Problem and the Proposed Solution

This thesis addresses the question of how landmark sampling techniques can be extended to include more information about the shape under examination. This is a topic of intensive research in the geometric morphometrics community (Moyers and Bookstein, 1979; Cutting et al., 1995; Bookstein, 1997; Andresen and Nielsen, 2001; Bookstein, 2005).

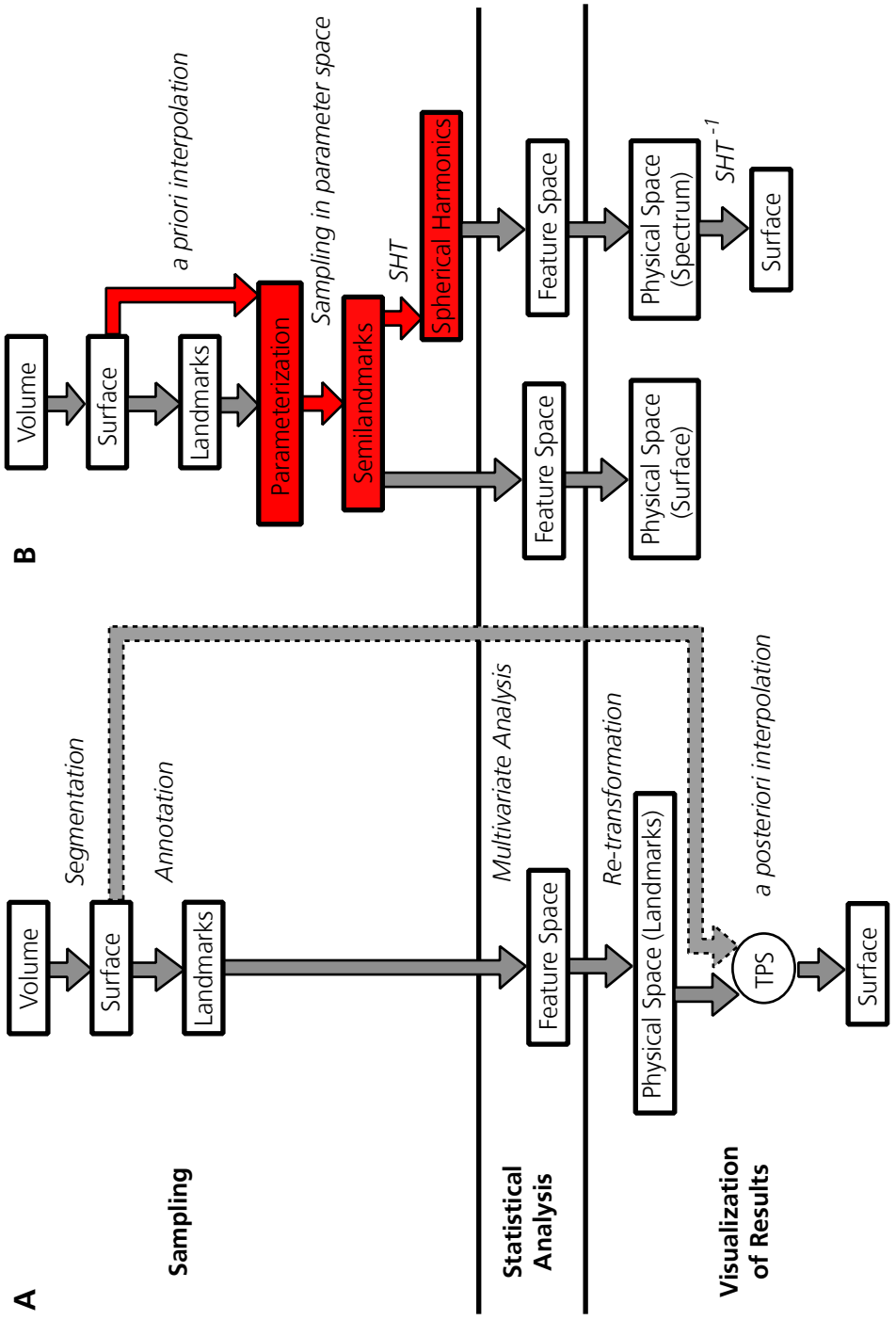

Figure 1.2: Geometric morphometrics pipeline. The pipeline consists of three major stages: *Sampling, Analysis* and *Visualization*. **A**: A typical landmark-based analysis is shown. For visualization purposes, missing geometric information is interpolated in an *a posteriori* fashion, using thin plate splines (TPS), to render complete surfaces. **B**: The geometric morphometrics pipeline is extended (red). Mesh parameterization methods permit *a priori* surface interpolation, prior to the actual quantification (sampling). Thus, a user-specified amount of geometric information is made available to the following analysis and visualization stages. This also circumvents the need for (ambiguous) *a posteriori* surface interpolation in the visualization step. SHT stands for spherical harmonics transform.

The key problem is a dearth of knowledge about the relation between biologically relevant aspects of organismic form and its geometrically relevant properties.

In general, the result of the segmentation step is a set of triangle-meshes with no restrictions on topology. In order to be suited for further processing, a mesh should be a *manifold*. This means the neighborhood of every point on the mesh locally approximates a plane, i.e., no singularities like self-intersections must occur. In many cases, the object of interest is *homeomorphic* to, or can be approximated by, a closed two-dimensional manifold.

This thesis deals with the special case of closed genus-zero surfaces (i.e., surfaces with no handles)[1] which are homeomorphic to a sphere, e.g., the endocast of the braincase.

Parameterizing the surfaces on the unit sphere permits to consistently interpolate the surface in-between the biologically homologous points of reference, the landmarks. The spherical signals can (1) be sampled to obtain semilandmarks and (2) be transformed into Fourier series of spherical harmonics coefficients. Thus, two comprehensive numerical representations are obtained. These representations can be analyzed with standard multivariate techniques, as in landmark-based analysis (Dryden and Mardia, 1998). For visualization, an advantage is that no *a posteriori* surface interpolation is necessary, which avoids the ad-hoc choice of a reference surface.

1.3 Thesis Overview

The thesis is subdivided into seven chapters. Chapter 2 presents the foundations of the new surface parameterization method. This includes introductions to geometric morphometrics and mesh parameterization, reviews of morphometrics on the sphere and endocast morphometrics, and an overview on MorphoTools, the application framework where the geometric morphometrics analysis and visualization part of this thesis has been implemented.

Chapter 3 presents homology-calibrated spherical parameterization as a new method to quantify surfaces of biological structures. First, different approaches to parameterize a genus zero surface on the sphere are compared. Next, a method is proposed to combine surface parameterization with landmark-based information in order to constrain the parameterization.

Chapter 4 deals with sampling the surfaces over the spherical domain and applying standard analysis and visualization methods from the geometric morphometrics toolbox on the new surface representation.

Chapter 5 presents the implementation of the parameterization and the geometric morphometrics methods. Special attention is given to spherical parameterization and sampling algorithms used to calculate the semilandmarks and Fourier surface representations. An overview on the MorphoTools architecture is followed by a detailed description of the extensions necessary to handle the new representations.

[1] Roughly speaking,the *genus* is the number of holes in a surface. Surfaces with the same genus are topologically equivalent (or homeomorphic), e.g., a bottle has genus zero and is homeomorphic to a sphere, and a coffee cup has genus one and is homeomorphic to a torus.

In chapter 6, the new methods of shape representation are applied to endocranial morphology. Specifically, endocasts of modern humans and great apes are compared, patterns of bilateral endocranial asymmetry are analyzed, and the shape transformation from a chimpanzee to a human braincase is analyzed in more detail.

Chapter 7 contains a recapitulation of the basic ideas presented in this thesis and discusses its results in both a technical and a biological context. The solutions and problem areas are highlighted and an outlook on possible directions for future research and tool development is given.

Chapter 2

Background

This chapter provides the reader with the necessary background information required to understand the principal topics of this thesis. Taking into account the trans-disciplinary approach, it provides a brief introduction to geometric morphometrics and an overview of its most important methods. Then, the focus is moved to computer graphics. An introduction to mesh parameterization is given, with emphasis on spherical parameterization. Morphometrics on the sphere is reviewed next. SPHARM, a Fourier descriptor based on spherical harmonics, and smooth deformations on the sphere are discussed. The following section reviews previous work concerning endocast analysis. MorphoTools, the software framework which was used to implement the analysis and visualization algorithms, is presented in the concluding section.

2.1 Geometric Morphometrics

Morphometrics (from the Greek: "morphe" = form or shape, "metron" = measure) covers methods of extracting measurements from shapes, i.e., quantifying shape. Typically, the shapes under examination are biological structures, and the goal in the broadest sense is to test biological hypotheses about patterns of form variability. Therefore, morphometric methods are explorative tools to examine biological forms. A typical workflow comprises the following steps:

1. Establishing hypotheses about shape variability
2. Sampling shape measurements
3. Comparing shape measurements
4. Interpreting the results in the light of the hypotheses

The initial step for the quantitative sampling of a form is to establish a biological hypothesis, on the basis of which sampling procedures are defined. These procedures

define a correspondence relationship between geometry and biology. Typically, anatomical points of reference, so-called *anatomical landmarks*, are used to establish biological correspondence (i.e., homology) between specimens. Distances, such as cranial length, height or breadth, or angles between landmarks are measured and used for multivariate statistical analyses, such as regression analysis, principal components analysis, linear discriminant analysis etc. During this process, data are transposed from physical (or real) space, in which the organisms exist, to a multivariate feature space of the morphometric analysis. Finally, the results are interpreted in terms of the biological hypothesis. Because in general, there is no way back from the feature space to the physical space, interpretation of the results in terms of real-space morphological variation is often difficult.

Traditional multivariate morphometric methods typically deal with sets of distance or angular measurements between anatomical landmarks, mostly due to technical limitations in data acquisition and processing (Blackith and Reyment, 1971). Modern approaches aim to integrate as much geometric information as possible into multivariate analyses. An important property of some of these new methods is the possibility of real-space visualization of the results obtained in feature space. This facilitates immediate, visual interpretation of the results and literally illustrates the visual and explorative character of morphometrics. These developments had a big impact on the paleoanthropological community (Rohlf and Marcus (1993); Zollikofer et al. (1995, 1998); Ponce de León and Zollikofer (2001); Adams et al. (2004) to just name a few), because results of studies can be communicated in a comprehensive quantitative form that is intuitively understandable. These modern approaches are called *geometric morphometrics* methods in general. They can be divided into two categories:

Landmark-based approaches. Like in classical morphometrics, these approaches rely on the definition of anatomical landmarks denoting locations of biological homology. The difference is that the Cartesian coordinates of every landmark (or the full set of inter-landmark distances) is used in the multivariate analysis, rather than an arbitrary subset of inter-landmark distances or angles (Bookstein, 1990, 1991; Lele and Richtsmeier, 1991; Richtsmeier and Lele, 1993).

Outline-based approaches. These approaches quantify forms by their 2D outline, or by 3D curves. Outlines are regularly sampled in equidistant intervals. These methods tend to quantify shape by the geometry and do not necessarily rely on point-to-point-homologies to be defined. A well-established approach is to transform real-space geometric properties into the multivariate space of harmonic functions (Fourier analysis) (Zahn and Roskies, 1972; Kuhl and Giardina, 1982; Lestrel, 1997).

It is interesting to have a closer look at this division. At the core, these two approaches represent different ways to *sample* the shape under investigation. Landmark-based approaches use the coordinates of the landmarks to represent the shape. Approaches based on the outline use the same concepts as in digital signal processing; the outline is encoded into a periodic signal, where the amount of geometric information contained in the signal is a function of the sampling rate. This is desirable from an information theo-

retical point of view, but, because there is no localized biological homology information in the sampled data, the results are often difficult to interpret. However, these methods permit intuitive analysis and visualization of organismic structures where only little biological homology information is available, because the whole form is included in the sampling and therefore in the results.

The question of how biological information can be identified in the geometry of a shape, and compared between specimen in a sample, has no general answer. Usually, the concept of homology is used. Here, homology is defined as follows:

Definition 1. ***Homology*** *denotes biological equivalence of structures through evolutionary and developmental history (Owen, 1843).*

For example, the left half of braincase A is homologous to the left half of braincase B, and the bregma (the junction of the sagittal and coronal sutures at the top of the skull) of individual A is homologous to the bregma of individual B.

Landmark approaches are based on the assumption that structures of *biological homology* can be reduced to infinitesimal points; for example, cranial sutures meet in one point (e.g., bregma, lambda). Landmarks are typically defined at meeting points between three or more adjacent structures (type I), or at extremal locations (type II) (Bookstein, 1990, 1991). It is a matter of debate whether it is good practice to ignore other geometric properties of homologous structures, such as curvature. Actually, it seems that even the biological definition of homology is a controversial issue (Rieppel, 1989; Lestrel, 1997).

Here, the concept of corresponding point homologies is considered as a valid approach to locate biological information, and the terms “landmark” and “point homology” are considered equivalent.

Another important point which needs to be clarified is the exact definition of the terms *form*, *shape* and *size*. These notions have both a geometric and a biological significance (Bookstein, 1989b). The following geometric definition is widely accepted:

Definition 2. ***Form = Shape + Size***

Size represents the geometry-free component of form (a scaling factor), while *shape* represents the purely geometric component of form (Mosimann, 1988).

The following section gives an overview of the geometric morphometrics methods relevant for this thesis.

2.1.1 A Landmark-Based Approach: Shape Space Analysis

Shape space analysis is a *Procrustes analysis* followed by a *deformation analysis*. The basic idea is that the shape of a specimen can be quantified as its deviation from a reference shape. This approach has several advantages. It corresponds to the way we perceive shapes and thus is visually intuitive. At the same time it is biologically sensible because shape transformation is an important aspect of ontogenetic and evolutionary change (Zollikofer and Ponce de León, 2005).

Thompson's Deformation Grids

Visualizing geometric relations between two organismic forms was pioneered by D'Arcy W. Thompson in his classic book *On Growth and Form* (1917). He visualized the geometric relations between two organismic forms by overlaying one form with a rectangular grid, attaching the grid to selected anatomic landmarks, and deforming it to fit homologous landmarks in the second form. The result is emergence of a comprehensive picture of shape transformation, based on corresponding landmarks (see figure 2.1).

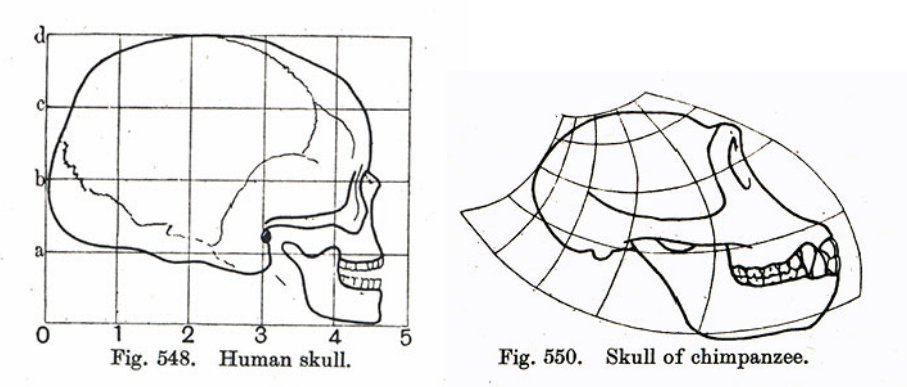

Figure 2.1: Thompson's illustration of the transformation of a human skull to a chimpanzee skull. Reproduced from Thompson (1917), with permission of the publisher.

Essentially, Thompson's method establishes an explicit link between the geometric transformation of one form into another one and the biological notion of a correspondence relation (e.g., homology). The concept has been formalized and developed into an explicit mathematical framework (Kendall, 1981; Rohlf, 1990; Bookstein, 1991; Dryden and Mardia, 1998), such that it is now possible to render form change visualizations in the style of Thompson's drawings with computer graphics tools (figure 2.2).

Kendall's Shape Space

David Kendall explored the mathematical and geometric properties of shape spaces in which each possible configuration consisting of K landmarks is represented as a single multidimensional point (Kendall, 1981, 1984, 1985). Similarity of shapes is measured as a distance between points. Shape spaces have the geometric properties of a sphere, or its multidimensional extension, a hypersphere. This is Kendall's most significant finding from the viewpoint of morphometric application. On the sphere, distances between shapes are measured along great circle segments in the same way as we measure distances between geographic locations on the earth. The non-linearity of shape spaces lead

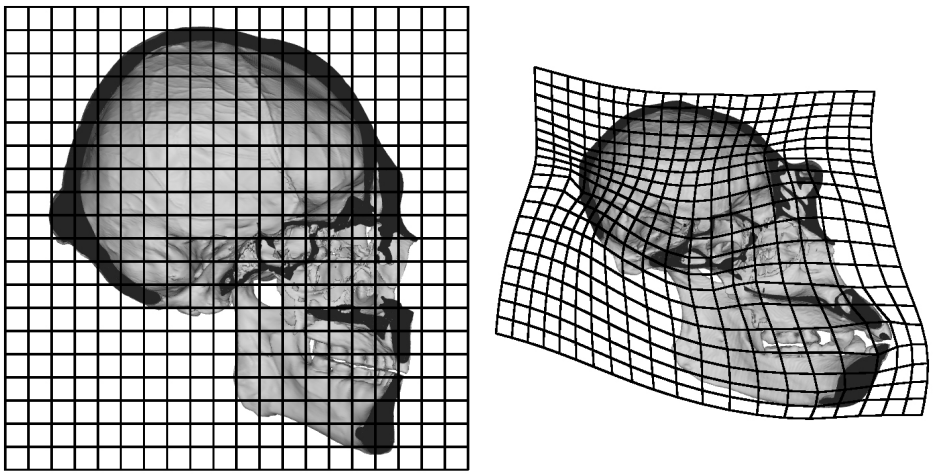

Figure 2.2: Deformation grid showing the transformation from a human skull to a chimpanzee skull. Thin plate splines were used to deform the grid; this is the formalized version of Thompson's approach.

to practical difficulties, the most critical one being the non-applicability of linear multivariate statistical procedures. In practice, a linearized, Euclidean version of Kendall's shape space is constructed by projecting a restricted spherical area to the tangential plane through a given point of reference. In the area close to the reference, the linear distances in the tangent plane are close approximations of the spherical distances. Extending the concepts to shape hyperplanes being tangential to shape hyperspheres leads to the notions of *linearized shape space*, or *tangent shape space* (Dryden and Mardia, 1998).

Procrustes Superimposition

In order to compare the shapes of specimens represented by K landmarks, we first need to find a reference configuration of the K landmarks. The comparisons can then be performed against the reference configuration, which serves as a "fixed point", where the tangential hyperplane representing the linearized shape space touches the hypersphere. The hyperplane is called *linearized Procrustes space*. Data in linearized Procrustes space can be analyzed with classic (i.e., linear) multivariate methods. If no reference shape is defined by a specific biological hypothesis, it makes sense to calculate a sample mean shape, or *consensus*, by means of generalized least-squares fitting procedures (Rohlf, 1990).

The most common size measure for landmark configurations is the *centroid size* (Bookstein, 1991), which is a scaling factor S, defined as follows:

$$S = \sqrt{\sum_{i=1}^{K} (\mathbf{p}_i - \mathbf{c})^2}; \qquad \mathbf{c} = \frac{1}{K} \sum_{i=1}^{K} \mathbf{p}_i, \tag{2.1}$$

where **c** is the centroid (i.e., the center of mass of the landmark configuration), and $(\mathbf{p}_i - \mathbf{c})^2$ the squared distance of landmark $\mathbf{p}_i$ from the centroid.

The expression *Procrustes superposition* denotes various methods of finding a consensus, of which *Generalized least-squares fitting* (GLS) is the most straight-forward method and comparable to regression analysis. In GLS, size is normalized by scaling all specimens to centroid size = 1. Positional differences are eliminated by superimposing the centroids of all specimens' landmark configurations. Differences in orientation are removed by rotating specimens around their centroids until the sum of squared distances between specimens, landmark by landmark, is minimized (see appendix B.1).

The linearized *Procrustes distance* between two landmark configurations L_1 and L_2 is defined as

$$d = \sqrt{\sum_{i=1}^{K} (L_1(i) - L_2(i))^2}, \tag{2.2}$$

where $L_1(i)$ is the i^{th} landmark of L_1.

Again, GLS is only one approach to Procrustes superposition (Rohlf and Slice, 1990). Superposition is a non-trivial problem where different optimality criteria yield different solutions.

Since we now operate in linearized shape space (determined by the superimposed landmark configurations and the reference shape), we can apply standard multivariate procedures such as PCA to reduce dimensions (see appendix B.3). Typically, the first few principal components (PC) reveal biologically relevant patterns.

Real-Space Visualization with Thin Plate Splines

Returning to Thompson's approach, the question is: how can differences between the shapes of two specimen be visualized? Or, more generally, how can patterns of shape variation in a sample be transformed from shape space to real space? Because all information contained in a landmark configuration is retained during the transformation from real space to shape space to PCA space, it is possible to transform a point from PCA space back into real space.

However, a set of landmarks alone gives a poor visual representation of patterns of shape change. A more comprehensive visual impression is obtained when the effects of landmark displacement are interpolated over the the entire space. This can be realized with spline functions. Thin plate splines (TPS) (Duchon, 1976; Meinguet, 1979; Bookstein, 1989a; Wahba, 1990) are used to interpolate the deviation of corresponding landmarks between two landmark configurations (in 2D or 3D). TPS are a reasonable choice because they minimize bending energy (the name thin plate spline refers to a physical analogy involving the bending of a thin sheet of metal).

With the aid of splines, it is straight-forward to construct 2D deformation grids in the style of Thompson (see figure 2.2). They provide an intuitive depiction of how subregions of the organismic structure under investigation are rearranged relative to each other. While this is a concise visualization in the case of two dimensions, the extension to

three-dimensional cuboid grids is problematic, because our visual attention is inevitably directed towards undesired boundary effects at the edges of the cuboid (Zollikofer and Ponce de León, 2002). Another problem is that deformation grids represent an external frame of reference without explicit biological meaning.

A more natural frame of reference is the organismic structure itself. Using spline functions, any specimen's graphical representation can be deformed such that the landmarks match a target configuration, for instance the consensus configuration or a series of synthetic landmark configurations along a PC axis. Advanced visualization techniques use false color mapping and glyph annotation to display local properties of the deformation, such as direction and magnitude of deformation (Zollikofer and Ponce de León, 2002).

A problem of spline-based visualization is that the choice of the specimen to be used for visualization and deformation is relatively arbitrary. For instance, consider an analysis of a sample of human and chimpanzee skulls. Let LM_H be a 3D landmark configuration of a human skull, LM_T that of a chimpanzee skull and LM_C the consensus configuration. To construct a consensus surface (i.e., the average between chimpanzees and a humans), any given specimen might be deformed such that its landmarks match the ones of the consensus. But landmark-based deformation of a human skull surface to the consensus results in a different surface than the analogous deformation of a chimpanzee surface to the consensus (figure 2.3).

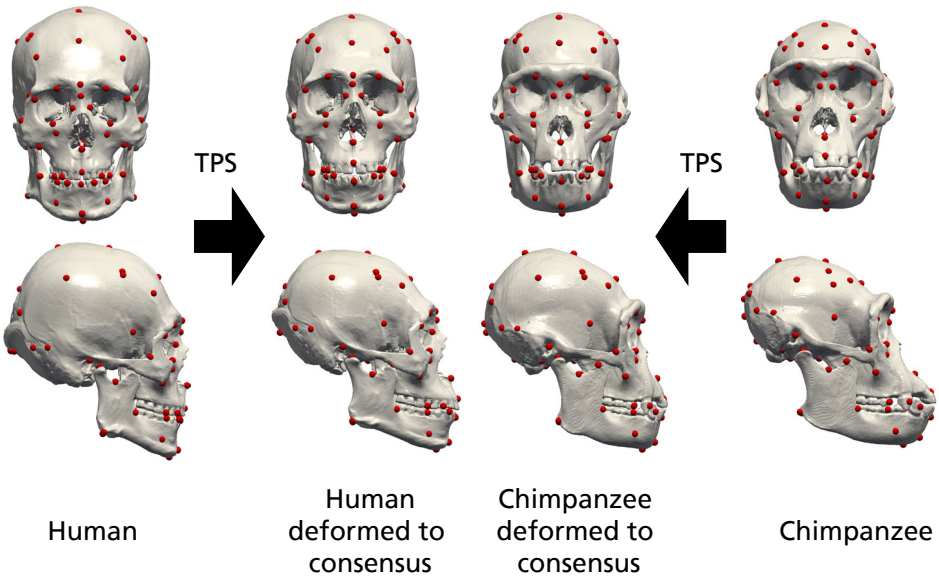

Figure 2.3: The arbitrariness of *a-posteriori* deformations. Human (left) and chimpanzee (right) skulls with 80 landmarks are deformed such that the landmarks match the consensus configuration. Thin plate splines were used to deform the surfaces. Because the target landmark configuration is the same in both cases (i.e., the consensus configuration), the surfaces in the middle approximate "the same" consensus surface; however, they clearly look different.

2.1.2 Outline-Based Approaches

These methods are all based on the same basic idea: to sample the (closed) outline of a form in regular steps. Usually, the outline is divided into N segments with equal length (see figure 2.4**A**). Different approaches for the analysis of the sampled forms exist. Let us assume that we have (x, y) coordinates of a set of N equally-spaced points p_k along outlines of M objects of interest.

Eigenshape Analysis

The Eigenshape analysis (Lohmann, 1983) is based on the $\phi^*(t)$ form of the Zahn and Roskies (1972) shape function, which is defined as follows:

1. For every point p_k, the net angular change in direction of a tangent $\phi(t_k)$ to the outline at p_k (see figure 2.4**B**) is calculated as one steps around its outline. Variable t is ranging from 0 to 2π, thus covering a circle in N steps $t_k = (k-1)/N \cdot 2\pi$.

2. $\phi(t)$ is circle-normalized:

$$\phi^*(t) = \phi(t) - t. \tag{2.3}$$

This representation is invariant to size, translation and rotation of the object, but depends on the location of the starting point and the direction of sampling along the outline (clockwise or counterclockwise). Various procedures to choose a consistent starting point have been suggested, the most obvious being to use a reference point such as a (homologous) landmark (Rohlf, 1986). Sampling the M outlines results in a set of M $\phi^*(t)$ vectors, which can be packed into the columns of a $N \times M$ matrix $\mathbf{Z}$. Multivariate analysis techniques can be applied to detect patterns of shape variation. In standard eigenshape analysis, a singular value decomposition (SVD) of matrix $\mathbf{Z}$ is applied to find the orthogonal directions of maximal shape variance.

Fourier analysis

A sampled outline can be seen as a sampled periodic signal $\phi^*(t)$, which can be transformed to a Fourier series by a discrete Fourier transform:

$$F(n) = F_n = \sum_{k=0}^{N-1} \phi^*(t_k) e^{-2\pi i k n/N}, \qquad n \in [0, N[\tag{2.4}$$

The complex coefficients F_n and the $\phi^*(t)$ contain exactly the same information, but in different spaces. We can rewrite $\phi^*(t)$ as

$$\phi^*(t) = A_0 + \sum_{n=1}^{N-1} (a_n \cos nt + b_n \sin nt), \tag{2.5}$$

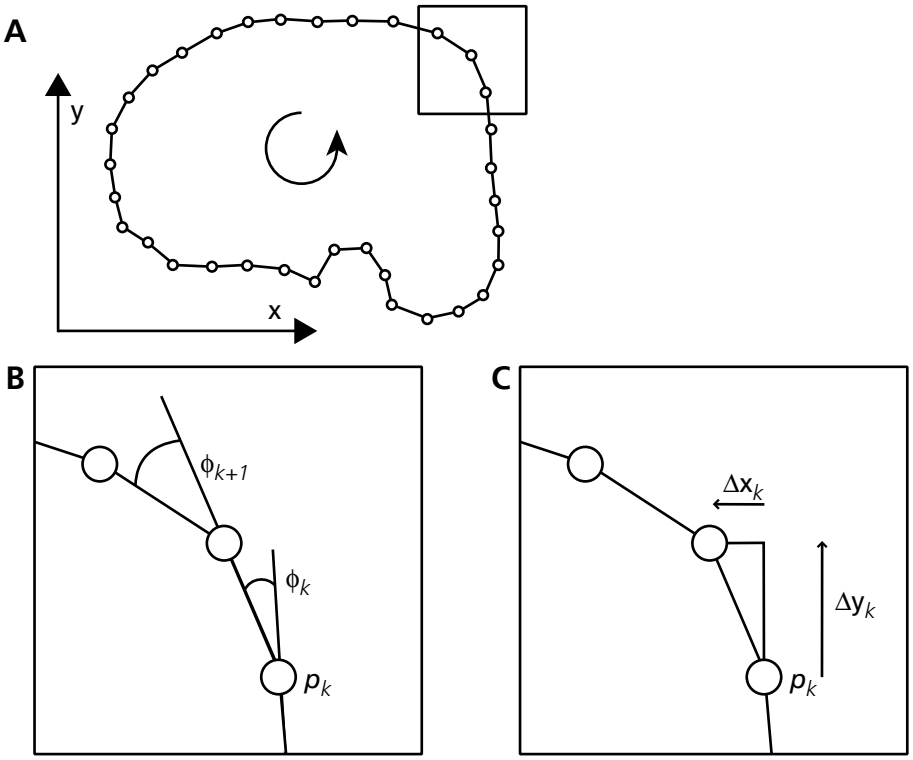

Figure 2.4: Outline sampling. **A**: The outline is sampled at N equally spaced points p. **B**: The $\phi(t)$ sampling measures the net angular change at every point p_k. **C**: Differential outline sampling for elliptic Fourier analysis. The deviations in x and y direction are sampled independently.

or, in polar coordinates,

$$\phi^*(t) = A_0 + \sum_{n=1}^{N-1} A_n \cos(nt - \alpha_n), \tag{2.6}$$

where A_n is the amplitude and α_n the phase angle for the n-th harmonic (Zahn and Roskies, 1972).

This approach permits analysis of outline shape variation at different levels of scale: low frequencies denote more global, large-scale, and higher frequencies more local, small-scale patterns of variation.

The representation (2.6) is invariant to translation, rotation and size of the outline, as well as position of the starting point p_0 on the outline. A major drawback is, however, the fact that curves reconstructed from Fourier space representations are not guaranteed to be closed and are sensitive to noise (Rohlf and Archie, 1984).

Elliptic Fourier Analysis

The *elliptic Fourier analysis* (EFA) is based on Fourier decompositions of first differences of x and y coordinates as functions of path length around the outline (Kuhl and Giardina, 1982). Elliptical Fourier functions (EFFs) represent a parametric formulation because the x and y coordinates are expressed as independent functions of the variable t.

First, the periodic signals $x(t)$ and $y(t)$ are transformed into their respective sequences of differences, as shown in figure 2.4**C**:

$$\triangle x_k = x_{((k+1) \bmod N)} - x_k, \qquad k \in [0, N[\tag{2.7}$$

$$\triangle y_k = y_{((k+1) \bmod N)} - y_k. \tag{2.8}$$

The $\triangle x$ and $\triangle y$ can then be decomposed into two Fourier series (Kuhl and Giardina, 1982), and $x(t)$ and $y(t)$ can be written as

$$x(t) = A_0 + \sum_{n=1}^{N} a_n \cos nt + \sum_{n=1}^{N} b_n \sin nt, \tag{2.9}$$

and

$$y(t) = C_0 + \sum_{n=1}^{N} c_n \cos nt + \sum_{n=1}^{N} d_n \sin nt, \tag{2.10}$$

EFF can be extended to 3D space curves, where a third coordinate z is added respectively.

The resulting Fourier descriptors are sensitive to size, translation and orientation of the outline as well as to the choice of the starting point. Several approaches for size-normalization, superposition and choice of the starting point have been suggested:

First-order ellipse Kuhl and Giardina (1982) suggested to use the first-order ellipse (i.e., the first harmonics of the two Fourier series). This approach is completely geometry-based. The original object is translated, rotated and scaled such that the ellipse center lies in the origin and the semimajor axis of the ellipse coincides with the x axis and has length 1. Then, the parameter space (i.e., the unit circle described by t) is rotated such that the starting point lies on $(1, 0)$.

Landmarks Another, more biology-based approach is to use landmarks for Procrustes superposition and size normalization of the original shapes (Baylac and Friess, 2005).

Comparison

It is interesting to identify the differences between the $\triangle x, \triangle y$ and the $\phi^*(t)$ samplings, and their consequences.

The sampling scheme of the $\phi^*(t)$ and the $\triangle x, \triangle y$ methods is the same, in the sense that the same discrete set of points is used for the measurements, but the *amount of information* sampled is different: one value per sampling point in the $\phi^*(t)$ sampling,

but two values for the $\triangle x, \triangle y$ sampling. It was already pointed out that the $\phi^*(t)$ is independent of size. The size is implicitly contained in the constant arc length between two sampling points. In order to be able to reconstruct the original form, we need to know this quantity. If the arc length would not be constant, we would have to store all the arc lengths between two successive sampling points. This information is contained in the $\triangle x, \triangle y$ notation; therefore, EFA does not strictly require equidistant sampling.

In a comprehensive theoretical comparison, Rohlf (1986) concluded that, using the same uniform sampling scheme for all methods (eigenshape analysis, Fourier analysis of the $\phi^*(t)$ representation and EFA), all lead to the same results. In an earlier, more practical comparison, however, Rohlf and Archie (1984) deduced that the EFA is the most generally useful method, and EFA found many applications in biology (Lestrel, 1997).

The expansion into a Fourier series transforms the outline from physical space into frequency space. The shapes are now represented by their spectrum, and differences between shapes by their frequency. A specimen's Fourier series is inherently ordered following a large-to-small scale scheme, i.e., the first few harmonics give a global approximation of the original curve, and the higher frequencies describe local detail.

2.1.3 Combinatorial Approaches

To summarize, we may discriminate between two extremes: methods which are based on homologous point sets on the one hand, and methods based on a comprehensive sampling of the geometry with only little biological information on the other. Several approaches exist which try to bridge the gap by combining the two. Besides the approach mentioned above (landmark-based Procrustes superposition, followed by EFA), more specific approaches exist.

Semilandmarks (Bookstein, 1997) are an extension of landmark-based shape space analysis. Additional points of reference are added in-between landmarks, denoting biological homology on outlines (or surfaces). The semilandmarks are positioned according to geometric optimality criteria, e.g., minimum bending energy or minimal Procrustes distance (Andresen and Nielsen, 2001; see Perez et al., 2006, for a comparison of the two). Whatever the criterion is, it is based on geometry, not on biology. Semilandmarks are thus often referred to as *sliding landmarks* because their position along the boundary structure does not contain biological information.

Extended Eigenshape Analysis: MacLeod (1999) extended the eigenshape analysis to include landmarks. Instead of sampling the whole outline in an equi-distant manner, the outline is divided into a set of outline segments bounded by the landmarks. Then, each outline segment is sampled separately. The sampling points along each segment divide that arc in sub-segments of equal length.

2.1.4 The Problems Addressed in this Thesis

So far, no morphometric method has been proposed which extends concepts of 2D outline analysis to a 3D surface. For morphometric analysis and visualization of surfaces such as the braincase, where landmarks denoting biological homology are sparse, such methods are essential.

Visualization based on the few available landmarks and using thin plate splines is unsatisfactory (see section 6.2.3). While semilandmark methods have been extended to 3D (Andresen et al., 2000; Andresen and Nielsen, 2001; Gunz et al., 2005), these methods have several shortcomings. The most critical is the ad-hoc definition of the positions of the semilandmarks. It is apparent that the number and initial position of the semilandmarks influence their final position, which is typically found in an iterative relaxation procedure. As a result, it is difficult to assess the biological significance and statistical value of the additional points.

In contrast, the outline-based approaches reviewed above are mathematically more rigorous because they use a well-defined parameter space, the unit circle. The goal here is to extend the outline-based approaches to a surface in 3D, where the analogous parameter domain is the unit sphere. This approach consists of the following tasks:

- Parameterize a closed surface such as an endocast on the unit sphere.
- Use homologous landmarks to increase the biological information contained in the parameterization.
- Use the parameterization to transform the surfaces described by triangular meshes to a Fourier series.
- Use the parameterization for comprehensive analysis and visualization of patterns of shape variability and shape transformation.

2.2 Mesh Parameterization

The most popular way to quantitatively describe a surface of arbitrary topological complexity is a *triangle mesh*, or more generally, a *polygon mesh*. In biological applications, meshes are often acquired automatically by 3D surface scanners or semi-automatically from 3D volume data obtained with computed tomography (CT) or magnetic resonant imaging (MRI). One advantage of triangle meshes is the simplicity of the description (i.e., explicit tables of vertices, their 3D coordinates, and edges and faces connecting them). Another advantage consists in the fact that modern rendering hardware is optimized for drawing triangles[1]. The major downside, however, is the difficulty to apply digital geometry processing algorithms, such as, for instance, texturing, data compression, scattered data approximation, remeshing and morphing (Schröder et al., 2001; Praun et al., 2001; Alexa, 2002; Sheffer et al., 2006).

[1] Modern graphics cards such as the NVIDIA Quadro FX can draw $\backsim 10^8$ triangles per second.

A solution to this problem is to parameterize the meshes on a convenient *parameter domain*, such as the plane or the sphere. A parameterization of a surface is a piecewise linear and bijective (and therefore diffeomorphic) mapping from a parameter domain to the surface. Usually, the parameter domain is a surface itself, i.e., the parameterization maps one surface into another.

Mapping a closed surface without holes (i.e., genus-0) to the plane received considerable attention (Eck et al., 1995; Floater, 1997; Sander et al., 2001, to just name a few). One special case is the mapping of a sphere to the plane, which had been studied for millennia in cartography (Ptolemy; Mercator; Lambert), a good introduction can be found in Floater and Hormann (2005). For the present purposes, however, a genus-0 surface needs to be mapped onto the sphere. This special case also received much attention in the last few years (Alexa, 2000; Gotsman et al., 2003; Praun and Hoppe, 2003; Gu et al., 2004; Zhou et al., 2004; Saba et al., 2005) .

Parameterizations almost always introduce *distortion* in angles and/or areas. A "good" (i.e., optimized) mapping is one which minimizes these distortions in some sense, depending on the optimization criteria. Many different criteria have been proposed. For example, consider the variety of projections used for drawing world maps (e.g., azimuthal, cylindrical, conformal, mercator etc.).

Aside from distortion, the *validity* of the parameterization is an important criterion. The parameterization must be a manifold, i.e., no triangle flips and self-intersections must occur.

The following sections give an introduction to parameterization methods with a focus on mappings to planar domains. Then, these concepts are extended to the spherical case, and finally, methods of consistent mesh parameterization are reviewed.

2.2.1 Differential Geometry Background

This section introduces basic concepts and notations of differential geometry (Kreyszig, 1968; Floater and Hormann, 2005; Botsch et al., 2006).

Let a surface $S \subset \mathbb{R}^3$ have the parametric representation

$$\mathbf{f}(u,v) = \begin{pmatrix} x(u,v) \\ y(u,v) \\ z(u,v) \end{pmatrix}, \qquad (u,v) \in \mathbb{R}^2 \tag{2.11}$$

where x, y, z are smooth, i.e., sufficiently often differentiable functions in u and v. The partial derivatives

$$\mathbf{f}_u = \frac{\partial \mathbf{f}}{\partial u} \quad \text{and} \quad \mathbf{f}_v = \frac{\partial \mathbf{f}}{\partial v} \tag{2.12}$$

span the tangent plane to S at $\mathbf{f}$. If $\mathbf{f}_u$ and $\mathbf{f}_v$ are linearly independent at every point, i.e., $\mathbf{f}_u \times \mathbf{f}_v \neq 0$, then the representation $\mathbf{f}$ is a *regular* parameterization.

The *first fundamental form* of $\mathbf{f}$ defines an inner product on the tangent space of S and characterizes many properties of $\mathbf{f}$. It is defined as the square of the element of arc

ds:

$$ds^2 = \mathbf{f}_u \cdot \mathbf{f}_u du^2 + 2\mathbf{f}_u \cdot \mathbf{f}_v du dv + \mathbf{f}_v \cdot \mathbf{f}_v dv^2,$$

We can write

$$g_{\alpha\beta} = \mathbf{f}_\alpha \cdot \mathbf{f}_\beta, \tag{2.13}$$

where $\alpha = u, v$ and $\beta = u, v$, and arrange the coefficients in a symmetric matrix

$$\mathbf{I} = \begin{bmatrix} g_{uu} & g_{uv} \\ g_{uv} & g_{vv} \end{bmatrix}. \tag{2.14}$$

The first fundamental form becomes

$$ds^2 = (du\ dv)\mathbf{I}\begin{pmatrix} du \\ dv \end{pmatrix}. \tag{2.15}$$

Often, the matrix $\mathbf{I}$ is itself called the first fundamental form. If $\mathbf{f}$ is regular, then matrix $\mathbf{I}$ has a strictly positive determinant

$$g = \det \mathbf{I} = g_{uu}g_{vv} - g_{uv}^2, \tag{2.16}$$

which is the discriminant of the quadratic form.

Matrix $\mathbf{I}$ (or its eigenvalues λ_1, λ_2) tells how distances (or angles and area) are translated from the parametric domain to distances on the surface. There are three interesting cases:

1. **Isometry** (preservation of distances)

$$\mathbf{f} \text{ is isometric} \Leftrightarrow \mathbf{I} = \begin{bmatrix} 1 & 0 \\ 0 & 1 \end{bmatrix} \Leftrightarrow \lambda_1 = \lambda_2 = 1, \tag{2.17}$$

2. **Conformality** (preservation of angles)

$$\mathbf{f} \text{ is conformal} \Leftrightarrow \mathbf{I} = \begin{bmatrix} \eta(u,v) & 0 \\ 0 & \eta(u,v) \end{bmatrix} \Leftrightarrow \lambda_1/\lambda_2 = 1, \tag{2.18}$$

   where $\eta(u, v)$ is called the *conformal factor*,

3. **Preservation of area**

$$\mathbf{f} \text{ is equi-areal} \Leftrightarrow \det \mathbf{I} = 1 \Leftrightarrow \lambda_1\lambda_2 = 1. \tag{2.19}$$

The first fundamental form can also be written as

$$\mathbf{I} = J^T J, \tag{2.20}$$

where J is the Jacobian of $\mathbf{f}$. For planar mappings (i.e., $\mathbb{R}^2 \rightarrow \mathbb{R}^2$), the Jacobian J is a square matrix, and it follows that singular values σ_1 and σ_2 of J are just the square roots of λ_1 and λ_2.

2.2.2 Degrees of Freedom of Equi-Areal and Conformal Maps

An isometric mapping may be called "ideal" because it preserves angles, areas and distances. Unfortunately isometric mappings only exist in very special cases. Isometric mappings to the plane are only possible if S is developable, such as a cone or a cylinder.

Practical approaches to surface parameterization therefore attempt to find a mapping which is either *conformal*, *equi-areal* or minimizes some combination of angle distortion and area distortion. Equi-areal mappings assign the same amount of parameter space to every surface element (*uniformity*). Conformal mappings, on the other hand, locally preserve geometry and have less degrees of freedom (DF) than mappings which preserve area. This can be seen in the above conditions for the mappings: The property of conformality (2.18) puts *two* conditions on the three coefficients g_{uu}, g_{uv}, g_{vv} of the first fundamental form:

$$g_{uu} = g_{vv} (= \eta(u,v)), \tag{2.21}$$

$$g_{uv} = 0, \tag{2.22}$$

while the property of area preservation 2.19 places only *one* condition,

$$g_{uu} g_{vv} - g_{uv}^2 = 1, \tag{2.23}$$

on them. If both properties (i.e., all three conditions) are used, we obtain

$$g_{uu} = g_{vv} = 1, \tag{2.24}$$

$$g_{uv} = 0, \tag{2.25}$$

which satisfies condition 2.17 and gives an isometric mapping.

The fact that conformal mappings have less DF than equi-areal mappings has important implications here because uniquely defined parameterizations are required in order to avoid ambiguity. The near-uniqueness of conformal mappings is a consequence of the Riemann mapping theorem, as we will see in section 2.2.4.

Ambiguity of Equi-areal Mappings

Here, the ambiguity of equi-areal mappings is demonstrated with an example originally proposed by Floater and Hormann (2005).

Let us look at the mappings

$$\mathbf{f}(x,y) = \begin{pmatrix} u(x,y) \\ v(x,y) \end{pmatrix} \tag{2.26}$$

from the unit disk D into itself. Using the mapping

$$\mathbf{g}(r,\theta) = \begin{pmatrix} r\cos\theta \\ r\sin\theta \end{pmatrix}, \tag{2.27}$$

we can express the mapping $\mathbf{f}$ in polar coordinates:

$$\mathbf{f}_p = \mathbf{f} \circ \mathbf{g}. \tag{2.28}$$

Because of the chain rule, the following equivalence holds for the Jacobians:

$$J(\mathbf{f} \circ \mathbf{g}) = J(\mathbf{f}) \cdot J(\mathbf{g}), \tag{2.29}$$

where

$$J(\mathbf{f}) = \begin{bmatrix} u_x & u_y \\ v_x & v_y \end{bmatrix}, \qquad J(\mathbf{g}) = \begin{bmatrix} \cos\theta & -r\sin\theta \\ \sin\theta & r\cos\theta \end{bmatrix}. \tag{2.30}$$

The determinant can be written as

$$\det J(\mathbf{f} \circ \mathbf{g}) = (u_x v_y - u_y v_x) \cdot r = u_r v_\theta - u_\theta v_r, \tag{2.31}$$

and therefore

$$\det J(\mathbf{f}) = u_x v_y - u_y v_x = \frac{u_r v_\theta - u_\theta v_r}{r}. \tag{2.32}$$

Now, let us look at the mapping

$$\mathbf{f} : D \to D \tag{2.33}$$

defined by

$$r(\cos\theta, \sin\theta) \mapsto r\left(\cos(\theta + \phi(r)), \sin(\theta + \phi(r))\right), \tag{2.34}$$

for $r \in [0, 1]$ and $\theta \in \,]-\pi, \pi]$;

$$\phi : [0, 1] \to \mathbb{R} \tag{2.35}$$

is an arbitrary function. Each circle of radius r, with center at the origin, is mapped onto itself through rotation by the angle $\phi(r)$, as shown in figure 2.5.

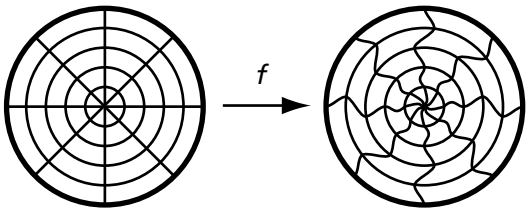

Figure 2.5: An equi-areal mapping from the unit disk into itself (modified from Floater and Hormann, 2005).

Assuming ϕ is differentiable, $\mathbf{f}$ is differentiable as well, and differentiating

$$\begin{pmatrix} u(r,\theta) \\ v(r,\theta) \end{pmatrix} = \begin{pmatrix} r\left(\cos(\theta + \phi(r))\right) \\ r\left(\sin(\theta + \phi(r))\right) \end{pmatrix} \tag{2.36}$$

leads to

$$u_r v_\theta - u_\theta v_r = r \tag{2.37}$$

irrespective of ϕ. Insertion into (2.32) gives $\det J(\mathbf{f}) = 1$, which means that $\mathbf{f}$ is equi-areal (see equation 2.19), independent of the chosen function ϕ.

2.2.3 Discrete Mappings

In practice, a smooth surface S is approximated by a piecewise linear surface $S_{\mathcal{T}}$ in the form of a triangle mesh. This is the union of a set $\mathcal{T} = \{T_1, T_2, ..., T_N\}$ of triangles T_i such that the triangles share common sets of vertices and edges V and E. Given a mesh $S_{\mathcal{T}}$ with vertices $\mathbf{v}_i \in \mathbb{R}^3$, a piece-wise linear mapping can be characterized by a second triangle mesh $S^*_{\mathcal{T}}$, which has the same connectivity as $S_{\mathcal{T}}$ (fig. 2.6**A**). The vertices $\mathbf{f}(\mathbf{v}_i)$ of $S^*_{\mathcal{T}}$ are located in the parameter domain, e.g., $\mathbf{f}(\mathbf{v}_i) \in \mathbb{R}^2$ for mappings to the plane. The piecewise linear mapping $\mathbf{f} : S_{\mathcal{T}} \rightarrow S^*_T$ maps every vertex $\mathbf{v}_i$ to $\mathbf{f}(\mathbf{v}_i)$ and defines a bivariate linear mapping

$$\mathbf{f}_i : \mathbb{R}^2 \rightarrow \mathbb{R}^2, \qquad \mathbf{f}_i(T_i) = T^*_i$$

for every triangle T_i. If no degenerate triangles and pairwise intersections of triangles exist, $S^*_{\mathcal{T}}$ represents a valid, bijective mapping. If local coordinate systems for triangles T are used, distortion can be measured for these atomic linear maps $\mathbf{f}_i$ (fig. 2.6**B**) using their Jacobians. The characteristics of $\mathbf{f}$ can be approximated by the sum of the characteristics of the $\mathbf{f}_i$. This is often used to define some energy functional, which is then minimized to achieve an optimal mapping. Various functionals have been proposed, for minimization of either angle or area distortion or a combination of both. Examples for maps with minimal angle distortion are (Eck et al., 1995, see section 2.2.4), the "most isometric parametrization" (MIPS) (Hormann and Greiner, 2000) and the "angle-based flattening" method by (Sheffer and de Sturler, 2001). (Maillot et al., 1993) and (Surazhsky and Gotsman, 2003) define area-distortion energies. Combinatorial approaches are the "stretch" metric from Sander et al. (2001) (see section 2.2.5) and the extended MIPS method with a user-controllable parameter to balance between area and angle distortion from Degener et al. (2003).

2.2.4 Conformal and Harmonic Mappings

Conformal mappings preserve angles and are connected to complex function theory. For example, planar mappings $\mathbf{f} : \mathbb{R}^2 \rightarrow \mathbb{R}^2$ can be seen as functions $\mathbf{f}$ of a complex variable,

$$w = \mathbf{f}(z), \tag{2.38}$$

that preserve local angles. An analytic (i.e., complex differentiable) function is *conformal* at any point where it has a nonzero derivative.

As shown previously (section 2.2.2), conformal mappings have less DF than equiareal mappings. The *Riemann mapping theorem* (Riemann, 1851) states that any simply connected region R of the complex plane $\mathbb{C}$ can be conformally mapped into any other simply connected region D (such as the unit disk) in $\mathbb{C}$. Moreover, if z_0 is a point in R, then there is a *unique* analytic function $\mathbf{f}$ mapping R to the unit disk such that $\mathbf{f}(z_0) = 0$ and the derivative $\mathbf{f}'(z_0) > 0$.

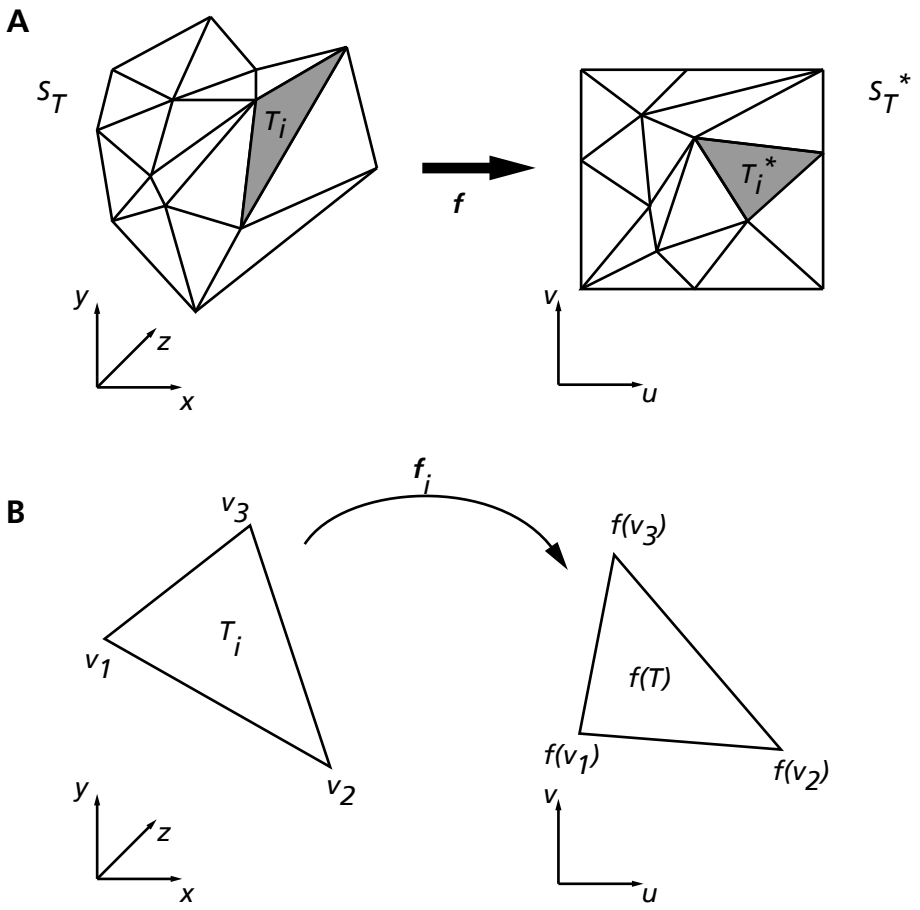

Figure 2.6: **A**: A piecewise linear mapping. The two meshes share the same connectivity, and individual triangles are mapped from a 3D mesh (left) to a planar mesh (right). **B**: each mapping $\mathbf{f}_i$ is a linear map ("atomic map").

A conformal mapping $\mathbf{f}$ satisfies the Cauchy-Riemann equations, which, with $z = x + iy$ and $w = u + iv$, are

$$\frac{\partial u}{\partial x} = \frac{\partial v}{\partial y}, \qquad \frac{\partial u}{\partial y} = -\frac{\partial v}{\partial x}. \tag{2.39}$$

By differentiating one of the equations with respect to x and the other one with respect to y (and vice versa), followed by equalization of the composite partial derivatives, we obtain the two Laplace equations

$$\triangle\, u = 0, \qquad \triangle\, v = 0, \tag{2.40}$$

with the Laplace operator $\triangle = \frac{\partial^2}{\partial x^2} + \frac{\partial^2}{\partial y^2}$.

A mapping $(u(x,y), v(x,y))$ which satisfies the two Laplace equations above is called a *harmonic mapping*. A conformal mapping is also harmonic (but not all harmonic mappings are conformal), implying the following relationship:

$$\textbf{isometric} \Rightarrow \textbf{conformal} \Rightarrow \textbf{harmonic}. \tag{2.41}$$

Harmonic mappings minimize the Dirichlet energy

$$E_D(\mathbf{f}) = \frac{1}{2}\int_S ||\text{grad } \mathbf{f}||^2 = \frac{1}{2}\int_S (||\nabla u||^2 + ||\nabla v||^2) \tag{2.42}$$

where ∇ is the gradient operator

$$\nabla \mathbf{f} = \left(\frac{\partial \mathbf{f}}{\partial x}, \frac{\partial \mathbf{f}}{\partial y}\right). \tag{2.43}$$

E_D can be seen as a measure for deformation. Harmonic mappings are much easier to calculate (at least approximately) than conformal mappings, and are often used to parameterize a closed genus-0 surface on a planar domain such as a disc or a square. However, the surface must be cut open, and the *boundary condition* (i.e., the form of the cut on the surface and the form of the boundary domain) makes the difference between a harmonic and a conformal map (Jin et al., 2004; Floater and Hormann, 2005).

Extension to mappings from a general surface S to the plane, $\mathbf{f} : \mathbb{R}^3 \rightarrow \mathbb{R}^2$ shows that the above properties of conformal and harmonic maps remain essentially the same. Instead of the Laplace operator $\triangle$, the *Laplace-Beltrami* operator $\triangle_S$:

$$\triangle_S = \frac{1}{\sqrt{g}}\left(\frac{\partial}{\partial u}\left(\frac{g_{22}}{\sqrt{g}}\frac{\partial}{\partial u} - \frac{g_{12}}{\sqrt{g}}\frac{\partial}{\partial v}\right) + \frac{\partial}{\partial v}\left(\frac{g_{11}}{\sqrt{g}}\frac{\partial}{\partial v} - \frac{g_{12}}{\sqrt{g}}\frac{\partial}{\partial u}\right)\right), \tag{2.44}$$

which generalizes the Laplace operator, is used (Floater and Hormann, 2005).

Discrete Harmonic Map

A finite element method to approximate a planar harmonic map was introduced by Eck et al. (1995). The boundary of the surface is mapped first, followed by finding a piecewise linear mapping of the surface which minimizes the Dirichlet energy. Equation 2.42 is used to find a linear system of equations

$$\sum_{j \in N_i} w_{ij}(\mathbf{f}(\mathbf{v}_j) - \mathbf{f}(\mathbf{v}_i)) = 0, \qquad \mathbf{v}_i \in V \tag{2.45}$$

where $\mathbf{f} : \mathbb{R}^3 \rightarrow \mathbb{R}^2$ is the mapping from the original mesh to the plane (figure 2.6), N_i denotes the set of neighboring vertices of vertex $\mathbf{v}_i$, and the weights

$$w_{ij} = \cot \alpha_{ij} + \cot \beta_{ij} \tag{2.46}$$

are calculated from the angles α_{ij} and β_{ij} opposite to the edge $\mathbf{v}_i\mathbf{v}_j$ (figure 2.7).

The linear system for the $\mathbf{f}(\mathbf{v}_i)$ is uniquely solvable because the associated matrix is symmetric and positive definite. Iterative methods like conjugate gradients can be used to solve the system, and in practice, good visual results are achieved with this method.

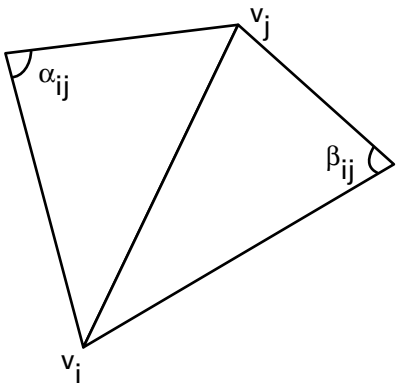

Figure 2.7: Harmonic weights. Angles α_{ij} and β_{ij} contributing to the weight w_{ij} of the edge between $\mathbf{v}_i$ and $\mathbf{v}j$.

2.2.5 Stretch

In practice, a reasonable balance is intended between angle and area preservation. An interesting approach is the one proposed by Sander et al. (2001), which defines two scalar functionals that measure the *stretch* of a planar mapping based on the singular values $\sigma_{1,2}$ of the Jacobian J of the atomic map $\mathbf{f}_i : \mathbb{R}^2 \rightarrow \mathbb{R}^2$, with $\mathbf{f}|_{T_i} = \mathbf{f}_i$:

$$L^2(\mathbf{f}_i) = \sqrt{\frac{\sigma_1^2 + \sigma_2^2}{2}}, \tag{2.47}$$

$$L^\infty(\mathbf{f}_i) = \sigma_1, \tag{2.48}$$

with $\sigma_1 > \sigma_2$. L^2 and L^∞ measure the root-mean-square (RMS) and the worst-case stretch, respectively, over all directions in the parameter domain.

Then, one of the two global functionals is optimized:

$$L^2(\mathbf{f}) = \sqrt{\frac{\sum\limits_{T_i \in T} (L^2(\mathbf{f}_i^{-1}))^2 A(T_i)}{\sum\limits_{T_i \in T} A(T_i)}} \tag{2.49}$$

where $A(T_i)$ is the area of triangle T_i, or

$$L^\infty(\mathbf{f}) = \max_{T_i \in T} L^\infty(\mathbf{f}_i^{-1}), \tag{2.50}$$

by iteratively optimizing the position of each vertex $\mathbf{v}_i$ within the kernel K_i of the star-shaped polygon formed by the neighbors of $\mathbf{v}_i$ (figure 2.8). The *kernel* of a polygon is defined by the set of points within the polygon from which the whole polygon is visible. For a star-shaped polygon, a kernel always exists, and the kernel always forms a convex polygon.

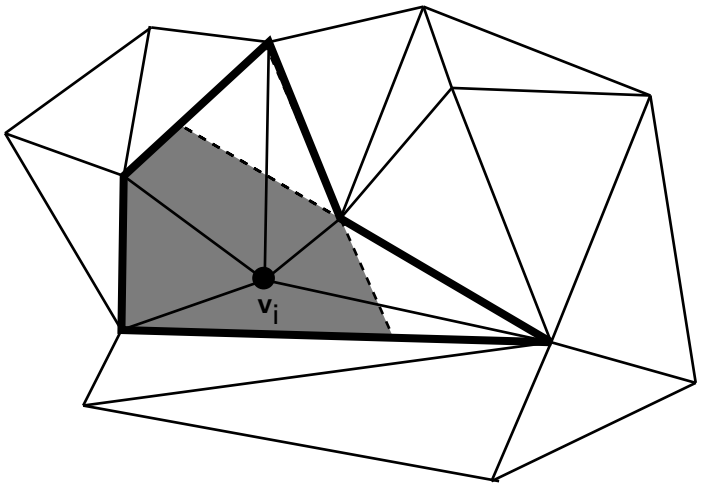

Figure 2.8: Polygon kernel. The neighbors of vertex $\mathbf{v}_i$ in a mesh form a star-shaped polygon (fat line). The kernel of the polygon is the convex area within, from where the whole polygon is visible.

In each iteration, a set of directions is randomly chosen, then the best position along these directions is determined, and the position which yields smallest local stretch is selected. Because $\mathbf{v}_i$ stays inside K_i, and represents a valid embedding, the final parameterization is guaranteed to be a valid embedding.

Stretch quantifies how distances in the parameter domain are scaled onto the surface. Large stretch implies that the reconstruction of the surface signal from a uniform sampling in the parameter domain will lose high frequency detail.

The stretch metric can be written as an explicit composition of angle and area distortion (Friedel et al., 2005).

2.2.6 Extension to the Spherical Domain

In the most common case, a disk-like surface in $\mathbb{R}^3$ is parameterized over a planar domain in $\mathbb{R}^2$ such as the unit disk or a square. However, for genus-0 surfaces, the unit sphere is a more natural parameter domain than planar domains since the meshes do not need to be cut, i.e., topology is preserved. The problem is similar to the planar case, with the additional constraint that all vertices lay on the unit sphere, i.e.,

$$|\mathbf{v}_i| = 1. \tag{2.51}$$

Moreover, this mapping implies a change from Euclidean to spherical geometry. Each mesh edge is mapped to a *great circle arc*, and each mesh triangle is mapped to a *spherical triangle* bounded by such arcs (fig. 2.9).

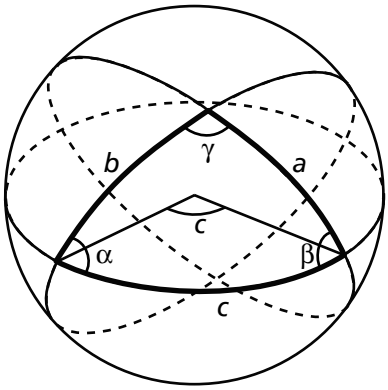

Figure 2.9: Spherical geometry. A spherical triangle, bounded by the arcs a, b, c, with the angles α, β, γ.

The lengths of the side arcs are denoted with a, b, c and measured in radians. The angles α, β, γ define the area A of the spherical triangle:

$$A = \alpha + \beta + \gamma - \pi, \tag{2.52}$$

where $\pi \leq \alpha + \beta + \gamma \leq 3\pi$. For large triangles, there are substantial differences between the planar and the spherical version. However, the numerical differences decrease when the mesh resolution is increased, i.e., triangle areas are reduced.

Global Conformal Parameterization

Gu and Yau (2002) showed that *harmonic maps from a closed genus-0 surface to the sphere are also conformal*. Intuitively, this follows from the missing boundary conditions (because no cut is necessary to open the mesh, no boundary has to be fixed in the plane). These authors also proposed an iterative algorithm which exploits this fact and yields a globally conformal parameterization (Gu and Yau, 2003).

The algorithm is based on the fact that a mapping $\mathbf{f} : S \rightarrow S^2$ from a closed surface S to the unit sphere S^2 is harmonic if, for every point $\mathbf{v}_i$ on the surface, the vector $\triangle_S f(\mathbf{v}_i) \in \mathbb{R}^3$ is orthogonal to the tangent plane of S^2 at $\mathbf{f}(\mathbf{v}_i)$, where $\triangle_S$ is the *Laplace-Beltrami* operator (see eq. 2.44).

A harmonic (and therefore conformal) map from a mesh $s_{\mathcal{T}}$ to the unit sphere S^2 can be discretely approximated by projecting the neighborhood of $\mathbf{v}_i$ to the tangential plane at its spherical image $\mathbf{f}(\mathbf{v}_i)$ and then build a system of (non-linear) equations, similar to equation 2.45:

$$\sum_{j \in N_i} w_{ij} (\Pi_{\mathbf{f}(\mathbf{v}_i)}(\mathbf{f}(\mathbf{v}_j)) - \mathbf{f}(\mathbf{v}_i)) = 0, \qquad \mathbf{v}_i \in V \tag{2.53}$$

where the w_{ij} are defined as in (2.46), and $\Pi_{\mathbf{v}}(\mathbf{u})$ is the component of $\mathbf{u}$ which is perpendicular to the tangential plane at $\mathbf{v}$. Gu and Yau (2003) use a steepest-descent algorithm to iteratively reposition the mesh vertices on the sphere until the tangential part of $\triangle_{S_\mathcal{T}}\mathbf{f}(\mathbf{v}_i)$ vanishes. The solution minimizes the so-called *harmonic energy*, which is defined as

$$E_{Harmonic}(\mathbf{f}) = \sum_{\{\mathbf{v}_i,\mathbf{v}_j\}\in E} w_{ij}|\mathbf{f}(\mathbf{v}_i) - \mathbf{f}(\mathbf{v}_j)|^2, \tag{2.54}$$

and it is called *global conformal* because it approximates conformality everywhere on the mesh.

If some of the weights w_{ij} become negative, topological correctness is no longer guaranteed. This problem is known from some planar mappings (convex combination maps, see (Floater and Hormann, 2005)), and arises when the sum of the two opposite angles α_{ij} and β_{ij} (see fig. 2.7) is greater than π, because:

$$w_{ij} = \cot\alpha_{ij} + \cot\beta_{ij} = \frac{\sin(\alpha_{ij}+\beta_{ij})}{\sin\alpha_{ij}\sin\beta_{ij}} \tag{2.55}$$

from which follows

$$w_{ij} > 0 \Leftrightarrow \alpha_{ij} + \beta_{ij} < \pi. \tag{2.56}$$

Therefore, the discrete harmonic map is not guaranteed to be bijective if the input mesh contains obtuse angles. Preprocessing has been suggested (Gu and Yau, 2003) and is used in practice to reduce the number of obtuse angles in the mesh, but it has been an open problem to achieve a triangulation of a non-planar surface containing only acute angles (Gu and Yau, 2003), which has been solved just recently by (Li and Zhang, 2006).

All bijective conformal maps from a closed genus-0 surface S to the sphere form the Möbius group, which has only six DF. A Möbius transform $\mathbf{f} : \mathbb{C} \to \mathbb{C}$ (where $\mathbb{C}$ is the complex plane), is defined as

$$\mathbf{f}(z) = \frac{az+b}{cz+d}, \qquad a,b,c,d \in \mathbb{C}, \qquad ad - bc \neq 0 \tag{2.57}$$

A conformal map to the sphere can be composed with any conformal mapping from the sphere onto itself to form a new conformal map. Three DF are the rotations around the coordinate axes and the others involve some sort of area (and distance) distortion. More precisely, it is changed by a scaling factor (the so-called conformal factor η in eq. 2.18), depending on the position on the surface. Thus, a number of conformal maps from $S_\mathcal{T}$ to the sphere exist, and the difference between them is the distribution of local area distortion.

In order to find a unique solution, additional constraints are needed. Haker et al. (2000) fix three points on the sphere and Gu and Yau (2002) propose the zero-mass center constraint

$$\int_{S_\mathcal{T}} \mathbf{f} d\sigma_{S_\mathcal{T}} = 0, \tag{2.58}$$

where $d\sigma_{S_\mathcal{T}}$ is the area element on $s_\mathcal{T}$. (2.58) defines a solution $\mathbf{f}$ which is unique up to the three rotations. Intuitively, the zero mass-center condition prevents extreme area-distortion ("non-uniformity"). However, it does not necessarily lead to the most uniform conformal parameterization. A way to find it has been proposed by Jin et al. (2004).

Let us point out an interesting parallel between the definitions of shape and size in geometric morphometrics (def. 2) and the concepts of angle and area distortion in surface parametrization. While in geometric morphometrics, size is just a scaling factor, the same is true for the area distortion in conformal maps. Conformally mapped triangles preserve their shapes, but get scaled by some factor.

Stretch on the Spherical Domain

The stretch metric has been generalized to the spherical domain by Praun and Hoppe (2003). Consider a mapping $\mathbf{f} : S_\mathcal{T} \rightarrow S^2$ from a surface $S_\mathcal{T}$ to the unit sphere S^2, let J be the Jacobian of this map, and $\sigma_{1,2}$ be its singular values. The stretch of a triangle T_i mapped to the spherical triangle T_i^* is defined as:

$$L^2(T_i) = \sqrt{\frac{1}{A_{T_i}} \iint\limits_{(u,v)\in T} \left(\frac{1}{\sigma_1^2} + \frac{1}{\sigma_2^2}\right) dA_{T_i}(u,v)}, \tag{2.59}$$

where (u, v) is a local orthonormal coordinate frame on T_i, and $dA_{T_i}(u, v)$ is the differential mesh triangle area. Because the Jacobian J (and thus σ_1 and σ_2) is not constant over a triangle, numerical integration is used to approximate L^2. The triangle is subdivided until the longest edge is shorter than a threshold, and the spherical stretch is approximated by the planar stretch.

Praun and Hoppe provide the following suggestions to avoid numerical problems:

1. Prior to numerical integration, spherical triangles with one angle close to π are split into two triangles with two angles close to $\frac{\pi}{2}$.

2. The correction term

$$\varepsilon \cdot \left(\frac{A_{T_i}}{4\pi}\right)^{\frac{p}{2}+1} \sigma_1^p \tag{2.60}$$

is added to the integrand in equation 2.59. Suitable parameter values are $\varepsilon = 10^{-4}$ and $p = 6$.

The same authors presented an algorithm based on a coarse-to-fine strategy, which is *guaranteed* to find a topologically correct (manifold) mapping of a genus-0 mesh $S_\mathcal{T}$ to the sphere. Figure 2.10 gives a pictorial explanation of the procedure. The key idea is to reduce $S_\mathcal{T}$ to a tetrahedron by performing a series of *edge collapses*, and thus constructing a *progressive mesh* (Hoppe, 1996). Because a tetrahedron is always convex, it can be embedded in the unit sphere by translating it such that the origin lies inside and then projecting the four vertices to the sphere, i.e., normalizing them (see eq. 2.51). Then,

the removed vertices can be re-inserted with *vertex splits*, the opposite operation to edge collapses, in inverse sequence. Analogous to the planar case (see section 2.2.5), every vertex is inserted into the spherical polygon kernel of its neighbors (which is defined in analogy to the planar case). After inserting a new vertex, the vertices in the neighborhood of the new vertex are optimized sequentially. In order to optimize a vertex, the sum of the stretch of the adjacent triangles is minimized. This is done by performing a set of great-circle searches in random directions within the kernel of the neighbors. Each time the number of vertices doubles, all vertices are optimized in sequence. This is repeated for all vertices whose neighbor vertices moved more than a threshold, until all vertices settle. Because every vertex always stays inside the kernel of its neighbors, the embedding is valid throughout all steps.

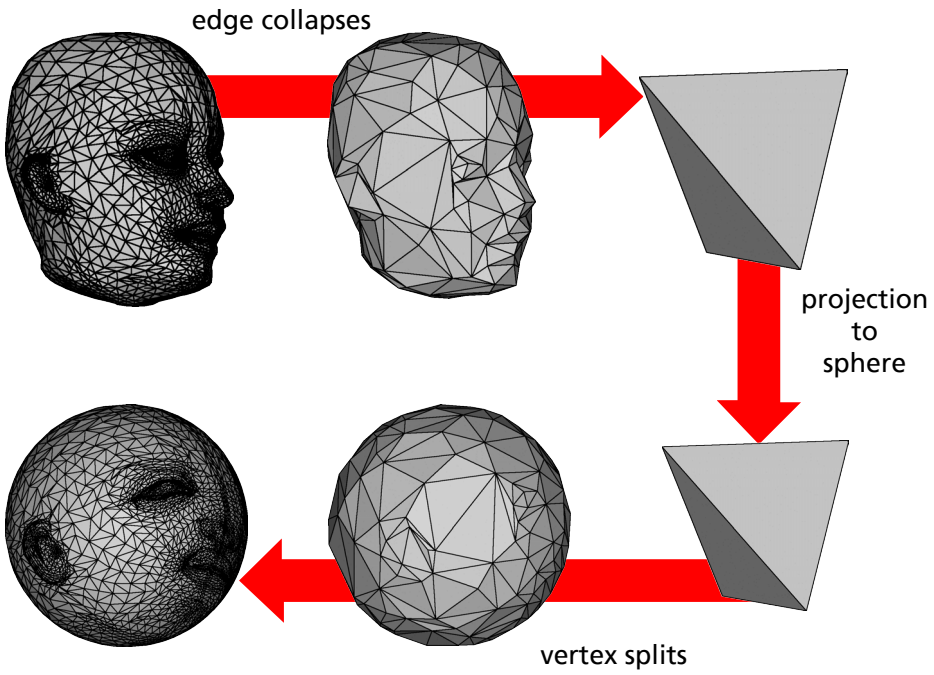

Figure 2.10: Progressive mesh-based spherical parameterization. A mesh is reduced to a tetrahedron by a sequence of edge collapses. The tetrahedron is projected to the sphere and vertices are re-inserted using vertex splits.

2.2.7 Consistent Mesh Parameterization

Parameterizations which map a set of triangle meshes to a common parameter domain, such that semantically matching features are mapped on the same position, are called *consistent*. Consistent parameterization is important for many digital geometry processing (DGP) applications, because it permits consistent remeshing, such that all models have the same connectivity and sampling pattern. Consistent remeshing is an important prerequisite for statistical applications, such as the calculation of an average model, or PCA.

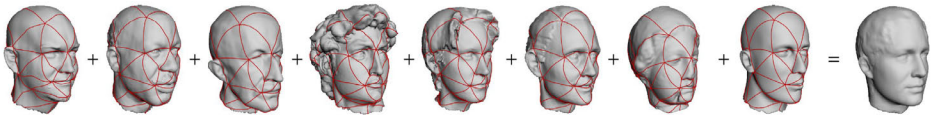

Figure 2.11: Consistent remeshing used for average head calculation. Figure reprinted from (Praun et al., 2001) with permission granted by the authors.

In the pioneering work of Praun et al. (2001), a set of genus-0 surfaces is consistently parameterized with respect to a (user-specified) base domain (fig. 2.11). They apply their algorithm on a set of human heads and a "mammal" data set of human, cow and horse models. On the head data set, they compute the first three "eigenheads", i.e., a set of eigenvectors of the variance/covariance matrix of the sample, which seem to to indicate hair on the front of the skull, hair on the back of the skull and smiling. Application on the mammal data set include texture transfer, for instance from a human body to the one of a horse, and shape blending, e.g., constructing whimsical creatures like a 50% cow, 25% human, 25% horse being.

Later work (Schreiner et al., 2004; Kraevoy and Sheffer, 2004) presented techniques which do not require the connectivity of the base domain to be defined by the user and are able to handle models of higher genus. However, these methods are limited to two or three surfaces to be parameterized because they avoid a simple common parameter domain.

Asirvatham et al. (2005) use the sphere as a common parameter domain. They employ a variant of the spherical parameterization algorithm from Praun and Hoppe (2003) to map a set of genus-0 surfaces to the sphere such that manually labeled features match. The surface in-between the feature points, however, is parameterized using random searches to minimize the stretch metric until a local minimum is found (see section 2.2.6). This gives visually satisfactory results but is not adequate for comparative analysis because no well-defined global optimum is reached.

This is a central issue for this thesis and is addressed in chapter 3.

2.3 Morphometrics on the Sphere

2.3.1 Spherical Harmonic Shape Descriptor

This section provides a review of the spherical harmonic shape descriptor (SPHARM) introduced by Brechbühler et al. (1992) and developed further in Brechbühler (1995) and Quicken et al. (2000). It is an extension of the elliptic fourier descriptor for 2D outlines (Kuhl and Giardina, 1982) to 3D surfaces.

Parameterization. In analogy to the 2D case, a genus-0 surface is parameterized on the unit sphere. While it is straight-forward to sample an outline in a uniform manner and to parameterize it on the unit circle (i.e., construct a distance-preserving mapping), we saw in the last section that it is not possible in general to parameterize a surface on the unit sphere without introducing distortion of distances. Brechbühler et al. (1992) parameterize the surface of a voxel volume onto the sphere by solving a nonlinear optimization problem. The special properties of the uniform quadrilateral structure (squares) of the voxel surface are exploited in order to equalize areas and minimize deviation from right angles of surface elements.

Expansion into a Fourier Series. Using the spherical parameterization, the surface is then expanded into a series of spherical harmonics. The spherical harmonics

$$Y_\ell^m(\theta, \phi) \tag{2.61}$$

are a set of orthonormal basis functions defined on the sphere with spherical coordinates $\theta \in [0, \pi]$ (the polar coordinate) and $\phi \in [0, 2\pi[$ (the azimuthal coordinate). Y_ℓ^m denotes the spherical harmonic function of degree $\ell \geqslant 0$ and order $m, |m| \leqslant \ell$ (see appendix A; fig. A.1 gives a visual impression).

The spherical parameterization is used to represent the surface as three spherical functions

$$\mathbf{f}(\theta, \phi) = \begin{pmatrix} x(\theta, \phi) \\ y(\theta, \phi) \\ z(\theta, \phi) \end{pmatrix}.$$

Using the spherical harmonics transform (SHT, see appendix A.1), $\mathbf{f}$ can be expanded into the series

$$\mathbf{f}(\theta, \phi) = \sum_{\ell \geq 0} \sum_{|m| \leq \ell} \mathbf{c}_\ell^m Y_\ell^m(\theta, \phi),$$

where the coefficients

$$\mathbf{c}_\ell^m = \begin{pmatrix} c_{\ell x}^m \\ c_{\ell y}^m \\ c_{\ell z}^m \end{pmatrix}$$

in the series are 3D vectors with complex components (real numbers for $m = 0$). The $\mathbf{c}_\ell^m$ are called the Fourier coefficients of $\mathbf{f}$, or the SPHARM descriptor of the surface.

Canonical Position. In analogy to the 2D case, where the first-order ellipse is used to align the outlines, the first-order ellipsoid, defined by $\mathbf{c}_1^m$, is used to align both the original surface and the spherical parameterization in a canonical way (see fig. 2.12). The details are described in appendix A.2. This procedure is sometimes called to produce a rotation-*invariant* descriptor, as it *normalizes*, or *standardizes*, the position according to some criteria (the directions of the main axes of the first order ellipsoid), while true invariance means *independence* of position without the need to define a criterion. The same is valid for size and translation normalization. Dividing all coefficients by the length of the longest main axis results in size-normalized descriptors, and ignoring the zero-order coefficients $\mathbf{C}_0^0$, which describe a translation, moves the centroid of the object to the origin.

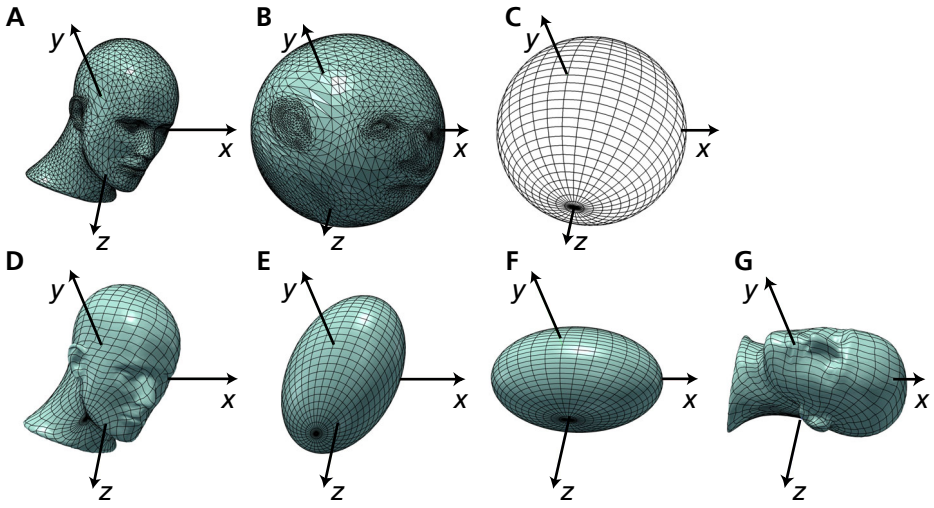

Figure 2.12: Canonical positioning using spherical harmonics. Top row: the original mesh (**A**) is parameterized on the sphere (**B**) and sampled with a spherical coordinate grid (**C**). The samples are then transformed to a set of spherical harmonic coefficients. Bottom row: Full reconstruction (**D**) and "first-order ellipsoid" (**E**), i.e., reconstruction from all coefficients up to degree 1. The ellipsoid is then used to canonically position both the original mesh and its spherical parameterization, such that the longest main axis points toward the x-axis and the shortest one along the z-axis, and the poles lie on the z-axis. The corresponding reconstructions are shown in **F** and **G**.

Application. The mathematical properties of the spherical harmonics, such as the natural large to small scale ordering, and the canonical positioning defined above, permit a wide range of applications.

Segmentation Kelemen et al. (1997) demonstrate the usage of the SPHARM model for automatic segmentation of the hippocampus from MRI volume data.

Medical imaging The SPHARM shape descriptor is widely used to analyze differences in brain regions. For instance, Gerig et al. (2001) compared brain ventricles of monozygotic (identical) and dizygotic (non-identical) twins; pathologies of the hippocampus were analyzed in (Shen et al., 2004, 2005; Gutman et al., 2006).

Shape compression and filtering Similar to Fourier-based image compression, a geometry can be compressed by removing high frequencies (i.e., truncating the $\mathbf{c}$ at a certain ℓ). More generally, filters can be designed to attenuate or amplify certain frequencies (Zhou et al., 2004).

Limitations The SPHARM descriptor is completely defined by the geometry of the objects under examination. For geometric morphometric applications, the main interest lies in the exact localization of the differences, and how this can be interpreted in terms of underlying biological processes. Therefore, inclusion of landmark data is necessary.

Moreover, the canonical positioning based on the first-order ellipsoid has its limitations, for instance when objects are similar to the sphere (e.g., the human brain) or the shape variability in the sample set is large (e.g., inter-specific analysis) (see also Shen et al., 2005; Huang et al., 2005). These issues will be addressed by examining how biological information can be introduced into the shape descriptor.

2.3.2 Deformation on the sphere

Smooth deformations of the spherical domain are relevant here because they permit to impose constraints on the spherical parameterization with biological features.

For Euclidean geometry, i.e., deformations of $\mathbb{R}^3$ into $\mathbb{R}^3$, thin plate spline (TPS) interpolation is the tool of choice because it minimizes bending energy. Unfortunately, TPS are not directly applicable to the spherical geometry, and operating in a linearized tangent space, as in shape space analysis (see section 2.1.1) is not possible either. The variability of biological forms is usually constrained to a small local area on the hypersphere which represents the Kendall shape space of all possible shapes. In the present situation, landmarks are distributed over *the whole sphere*, so the whole sphere must be considered for calculation of the deformations. Figure 2.13 shows an example.

This problem was addressed by Glaunès et al. (2004). The *landmark matching problem* can be defined as follows: Given a set of N initial landmarks $\mathbf{x}_1, ..., \mathbf{x}_N$ and a set of target landmarks $\mathbf{y}_1, ..., \mathbf{y}_N$, where the $\mathbf{x}_i$ and $\mathbf{y}_i$ are in some domain Ω, find a smooth deformation such that landmarks $\mathbf{x}_i$ match landmarks $\mathbf{y}_i$. This is equivalent to finding an optimal diffeomeorphism $\mathbf{d} : \Omega \to \Omega$ such that $\forall i : \mathbf{d}(\mathbf{x}_i) = \mathbf{y}_i$.

For the Euclidean case (the plane), the landmark matching problem can be solved with TPS interpolation (Bookstein, 1991). TPS are inspired by radial basis functions from approximation theory and model the deformation map between the initial and target landmarks by a vector field $\mathbf{v}$ such that $\mathbf{y}_i = \mathbf{x}_i + \mathbf{v}(\mathbf{x}_i)$. The vector field is a sum of spline vector fields centered at each point $\mathbf{x}_i$. This leads to a linear system of equations, which can readily be solved.

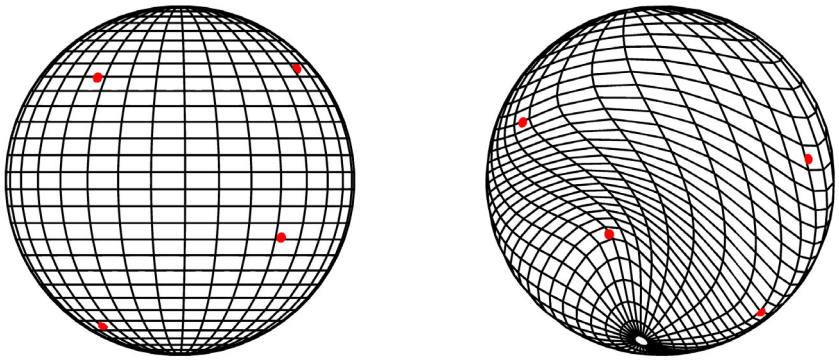

Figure 2.13: Large deformation on the sphere. The spherical domain is smoothly deformed such that a set of source landmarks (left) match a set of target landmarks (right).

For deformations on the sphere (i.e., $S^2 \rightarrow S^2$), this method can be seen as a infinitesimal version of the spherical problem, defined in the tangent space. It provides a method for the interpolation of vector fields on the sphere and is used to build an initial deformation map.

Glaunès et al. set up a time-dependent vector field on the sphere, based on the trajectories from the $\mathbf{x}_i$ to the $\mathbf{y}_i$. Similar to the planar case, the vector field $\mathbf{u}(x,t)$ is the interpolation of the trajectories $\mathbf{x}_1(t), ..., \mathbf{x}_N(t),\ t \in [0,1]$ over the whole sphere. The end points of the trajectories are the corresponding target landmarks, i.e., $\mathbf{x}_1(1) = \mathbf{y}_1, ..., \mathbf{x}_N(1) = \mathbf{y}_N(1)$. The quantity

$$\int_0^1 ||u(\cdot,t)||_V^2 dt \tag{2.62}$$

defines the energy of the N trajectories. Using the above-mentioned TPS operations in the tangent space, the trajectories are initialized to the geodesics (note: geodesics have zero bending energy in spherical geometry). A gradient descent method is then used to iteratively minimize the energy (2.62). The resulting smooth deformation is unique.

2.4 Endocast Morphometrics: A Short Review

Because brain evolution is a central topic of paleoanthropology, and because the endocast of the braincase is the only available source of information about fossil brain structure, quantitative endocranial shape analysis is of great interest (Holloway, 1978; Falk, 1986, 1987, 1992; Bruner et al., 2003; Bruner, 2004). Looking at our closest living relatives, the great apes, it is clear that the human brain is much larger. Because it can readily be measured, endocranial volume and inferred brain size are the principal quantitative data considered in the paleoanthropological literature about hominid brain evolution (Holloway

et al., 2004). But the question as to which areas of the brain expanded most during human evolution is a question of shape, rather than size.

The field of *paleoneurology* is concerned with the study and analysis of fossil endocasts. Most previous work consists of qualitative analysis of plaster endocranial casts (Holloway, 1975; Holloway et al., 2004). A major boost for the analysis of inner structures was the introduction of 3D CT scans, which permits non-invasive construction of virtual endocasts (Conroy et al., 1990; Tobias, 2001; Schoenemann et al., 2007).

The ultimate goal for paleoanthropologists is to find a mapping between function in the human brain and structure of the endocranial surface. It is clear that this is a complex task; however, medical imaging techniques now permit to quantify the brain-bone interface in living subjects. One fundamental question, namely how the brain surface is related to the endocranial surface, was studied by (Symington, 1916) and (Connolly, 1950). However, this essential topic has received relatively little attention until recently (Zollikofer and Ponce de León, 2000). *Brain mapping* is a term used for a number of techniques used to build a relationship between structure and function in the human brain (Friston, 1998; Sereno, 1998; Van Essen, 2002; Gu et al., 2004).

Few quantitative approaches to analyze endocranial shape variation were proposed, partly because of the incomplete fossil record, and partly because of difficulties in quantification of endocranial morphology. Holloway (1981) presented a pioneering approach using a polar stereo-plotting technique[2], and Bruner (2004) analyzed fossil endocasts of the species *Homo* with traditional morphometric measurements and landmark-based 2D techniques.

To summarize, endocranial shape analysis has to deal with three issues:

1. Relationships between endocranial structures and structures on the brain surface are often unknown, because the space between the brain surface and the enclosing bone is filled with meningeal tissue and cerebrospinal fluid.

2. Because of the smooth geometry, it is difficult to define and place point homologies on the endocast.

3. There is a lack of geometric morphometric methods to effectively analyze shape variation of structures exhibiting a smooth geometry, such as the endocast. Therefore, often 2D techniques are used which do not properly account for the 3D structure of the data.

This thesis addresses the second and the third point. It investigates how whole landmark-depleted closed surfaces can be quantified in a biologically meaningful way, and how the obtained data can be statistically analyzed and the results be visualized.

[2]Interestingly, his drawings look very similar to projections of spherical coordinate grids obtained in the applications chapter, shown for example in figure 6.3**F**.

2.5 MorphoTools: Tools for Data Analysis and Exploration

MorphoTools is a computer application framework for the interactive morphometric analysis of 3-dimensional biomedical object data. As discussed in the previous sections, a diversity of morphometric methods is available to investigate form variation in organismic structures. However, it is often difficult for researchers to specify which method is best used to test a given biological hypothesis and how multivariate morphometric results shall be analyzed and visualized in a comprehensive manner. There is therefore a need for interactivity and flexibility in the choice of computer-based methods for morphometric analysis and visualization.

The principal aim of MorphoTools is to provide specific, but platform-independent computation and visualization tools, which help users in the biosciences devise and perform interactive morphometric analyses of 3-dimensional organismic structures exhibiting a complex and variable topology. Users are enabled to specify their hypotheses in terms of one or more morphometric models, sample the adequate data and perform the corresponding morphometric analyses. The results can then be visualized using various rendering paradigms, which permit quantitative comparisons between the outcomes of alternative analyses. Combining and uniting these tasks within an adaptive application framework promotes an iterative approach to the process of hypothesis-building, analysis and interpretation of morphometric data.

The design of MorphoTools as an open framework is based on principles of sustainability, re-usability, extendability and portability, thus complying with the comparatively large time range of bioscientific research projects ($\backsim$ 10 years). This lays the basis for the seamless incorporation of future developments in morphometric analysis and scientific visualization.

2.5.1 Motivation

In view of the diversity of the biomathematical foundations of the morphometric methods mentioned before, it is important to realize that their application to empirical data sets reveals a number of commonalities (see fig. 2.14). Each morphometric analysis starts with a research hypothesis. This implies that the morphometric methods must be chosen and tuned to user-specified requirements in order to guarantee the adequate operationalization of the research hypothesis. Once the analysis has been carried out, the morphometric and statistical results must be converted back into a form which permits their interpretation in terms of the initial hypothesis. Obviously, the link between hypotheses, methods and results is a preliminary one. In a typical research process, the results of a first run are used to refine the hypotheses, fine-tune the methods and obtain better results, resulting in an essentially iterative approach.

Combining three-dimensional data acquisition techniques with morphometric analysis and visualization in a transdisciplinary approach has proven effective in many areas of biomedical research. Over past decades, a variety of software tools have been developed (see Morpheus, Morphometrika and other programs at the morphometrics home-

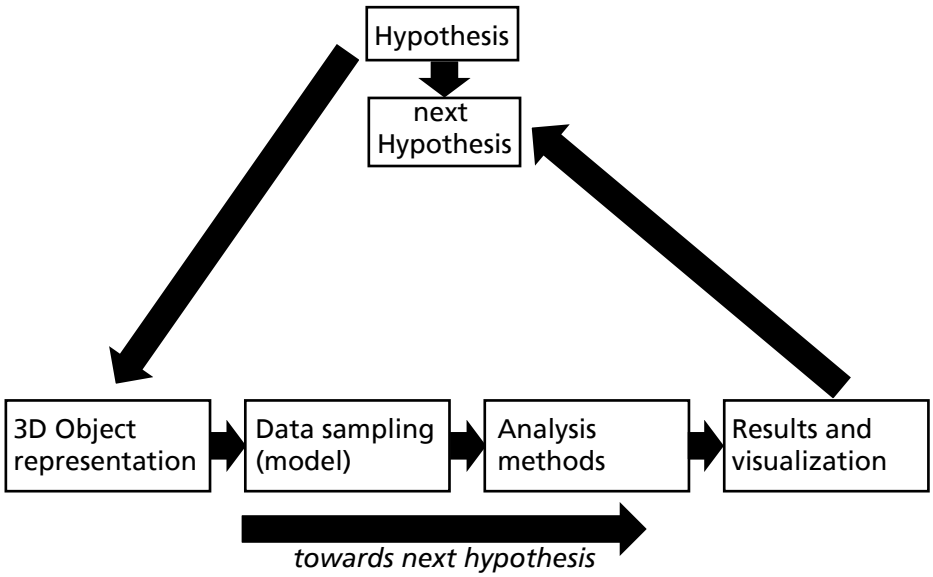

Figure 2.14: Hypothesis refinement cycle.

page at Stony Brook[3], WinEDMA[4] and Morphologika[5]) which focus on one or more of these points, and which can be applied to specific research issues from anthropology and medicine (Richtsmeier and Chevrud, 1986; Richtsmeier and Lele, 1990; Richtsmeier, 1993; Richtsmeier and Walker, 1993; Bookstein and Green, 1994; Cutting et al., 1995; Bookstein, 1996, 1997; Richtsmeier et al., 1998; Bookstein et al., 1999; Andresen et al., 2000; Andresen and Nielsen, 2001).

2.5.2 Research Goals

From the perspective of computer science, the most challenging aspect of MorphoTools consists in the development and implementation of concepts, which facilitate the application of morphometric methodologies following user-defined goals. Traditionally, morphometric methods and software tools determine to a large extent the scope of hypotheses that can be tested and of analytical methods that can be used. MorphoTools reverses this order: researchers specify hypotheses and use MorphoTools to devise methods of data sampling, analysis and visualization and, on the basis of the obtained results and interpretations, refine hypotheses and results in subsequent steps of iteration.

Two stages in the geometric morphometrics pipeline (see fig. 1.2) are most important for this:

[3]See `http://life.bio.sunysb.edu/morph/` for more information.
[4]See `http://www.getahead.psu.edu/` for more information.
[5]See `http://www.york.ac.uk/res/fme/resources/software.htm` for more information.

Data sampling and the treatment of unknown or incomplete data. In anthropological studies, incompleteness comes in an obvious form, the lack of actual data, for example in fragmentary fossils, and in a less obvious form, the lack of knowledge about data. For example, in developmental or evolutionary studies of morphology, the exact homology relation (i.e., developmental and/or evolutionary correspondence) between biological structures is often unknown or only partially known and depends on a-priori hypotheses. Morphometric analyses typically start with the assumption that geometric homology reflects biological homology to some degree. Here, new software tools to specify such hypotheses explicitly in terms of data sampling procedures (such as the methods developed in this thesis), and tools to refine hypotheses and tests during iterative analyses remain to be developed. This issue can directly be addressed in terms of scientific computation and visualization. The establishment of homology relations between specimens of a sample can be formulated as a problem of data registration (Rohlf and Slice, 1990; Toennies et al., 1990; Andresen and Nielsen, 2001). The level of detail at which biological structures are sampled to obtain data for morphometric analyses is closely related to problems of data reduction and/or parameterization of free-form objects.

Visualization of multidimensional data resulting from the morphometric analysis of biological structures. Morphometry, whether traditional or geometric, relies upon multivariate analytical techniques and thus yields results represented in multidimensional, abstract data spaces. The back-translation of the results of a multivariate analysis into the three dimensions of physical space and into biological meaning is far from trivial and involves the implementation of hypothesis-driven visualization procedures that permit the assessment of multivariate results from a variety of user-defined perspectives (Zollikofer and Ponce de León, 2002). The visualization of morphometric results establishes a direct link between the biosciences and computer graphics. However, the aims of these two fields are slightly different: While the primary goal of geometric morphometrics is to quantify differences in form between 3D objects using the paradigm of shape transformation (Rohlf and Slice, 1990; Bookstein, 1991), the methods of 3D morphing in computer graphics aim at blending between two or more, possibly textured, objects in an aesthetically appealing way (Lazarus and Verroust, 1998; Alexa, 2002). Nevertheless, the methods used in both fields are similar: a common parameterization (such as achieved with the methods developed in this thesis) is sought for multiple objects. In this area, further research is necessary to exploit the potential of existing morphing methods in the framework of morphometric applications.

2.5.3 Implementation Sketch

From a technical point of view, the geometric morphometrics pipeline is mapped to a *visualization pipeline* (Schroeder et al., 2003), which is similar to a data-flow graph in software engineering, as shown in figure 2.15**A**. Each node in the pipeline performs a dedicated computation task and has a number of input parameters. These parameters control biological, statistical or visual characteristics of the analysis, such as the set of

landmarks included in an analysis, the multi-dimensional position in feature space that is to visualize, and various visualization parameters used to render the resulting structure. When a parameter is changed, the concerned sub-graph is updated immediately ("closed-loop feedback") and the effect of the parameter change is visible instantly.

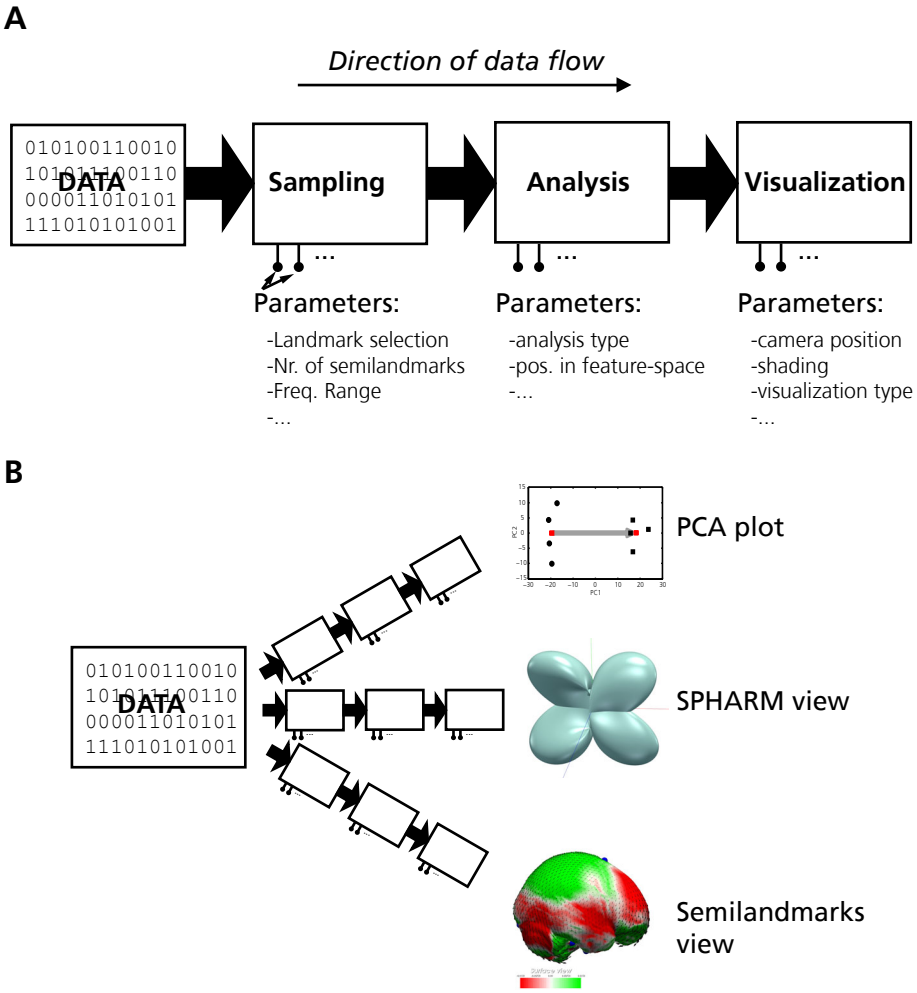

Figure 2.15: Visualization pipelines. **A**: Simple visualization pipeline, representing the geometric morphometrics pipeline. Data is passed on from node to node in the direction of the arrows. Changing a parameter of a node causes recalculation of its output and propagation to all nodes depending on that data. This represents a closed-loop approach for interactive data exploration. **B**: Different geometric morphometric analyses are mapped to different data visualization pipelines and provide different views on the data, therefore permitting comparative data exploration.

Several different types of geometric morphometric analysis can be incorporated into the data-flow graph at the same time. A hypothesis can be mapped to multiple visualization pipelines by choosing different sampling models and different techniques of statistical analysis and visualization of the results, thus providing different views on the data (see fig. 2.15**B**).

Data exploration does not stop at the change of well-known and predefined parameter sets but reaches into more technical domains such as designing and implementing novel data processing and visualization algorithms. Therefore, MorphoTools is designed and implemented as an *open research platform* which facilitates implementation of new methods.

The software has been designed and developed as a part of this PhD thesis and has been used to explore the usability for geometric morphometric analysis of the new samplings obtained via the spherical parameterization. It is currently further developed in the PhD thesis of Renaud Lebrun. He focuses on implementing advanced interactive statistical methods for landmark data to find answers to specific biological questions.

Chapter 3

Consistent Homology-Calibrated Spherical Parameterization

In this chapter the main contribution of this thesis is presented. A formal model for consistently parameterizing a set of genus-0 surfaces on the sphere with the aid of additional biological information in the form of landmarks is established. The problem of surface parameterization is complex and can be solved in different ways, with different advantages and disadvantages. It is not obvious which parameterization strategy is the best for our application. Therefore, we define a set of metrics which characterize the quality of the parameterizations obtained. These metrics are then used to compare two fundamentally different of parameterization strategies and to examine the effect of adding biological information.

3.1 Consistent Homology-Calibrated Spherical Parameterization

Figure 3.1 gives a pictorial explanation of the procedure. We have a set of N_S endocranial surfaces M_i, represented as triangle meshes. On every surface, a set L_i of N_L points $\mathbf{l}_{i,j}$ is manually labeled. The sets L_i indicate biological correspondence across the surfaces. Our goal is to find a piecewise linear, bijective mapping $\mathbf{h}_i$ from each surface M_i to the sphere S^2

$$\mathbf{h}_i : M_i \rightarrow S^2 : (x, y, z) \mapsto (\theta, \phi), \qquad i \in [1, N_S], \tag{3.1}$$

where θ, ϕ are spherical coordinates (see fig. 3.4), such that:

1. for all surfaces, corresponding points of biological homology are mapped onto the same position $\mathbf{p}_j$ in parameter space, i.e.,

$$\mathbf{h}_1(\mathbf{l}_{1,j}) = \mathbf{h}_2(\mathbf{l}_{2,j}) = ... = \mathbf{h}_{N_S}(\mathbf{l}_{N_S,j}) = \mathbf{p}_j \tag{3.2}$$

2. the surface between the landmarks is mapped in an "optimal" way, where optimality criteria will be defined below.

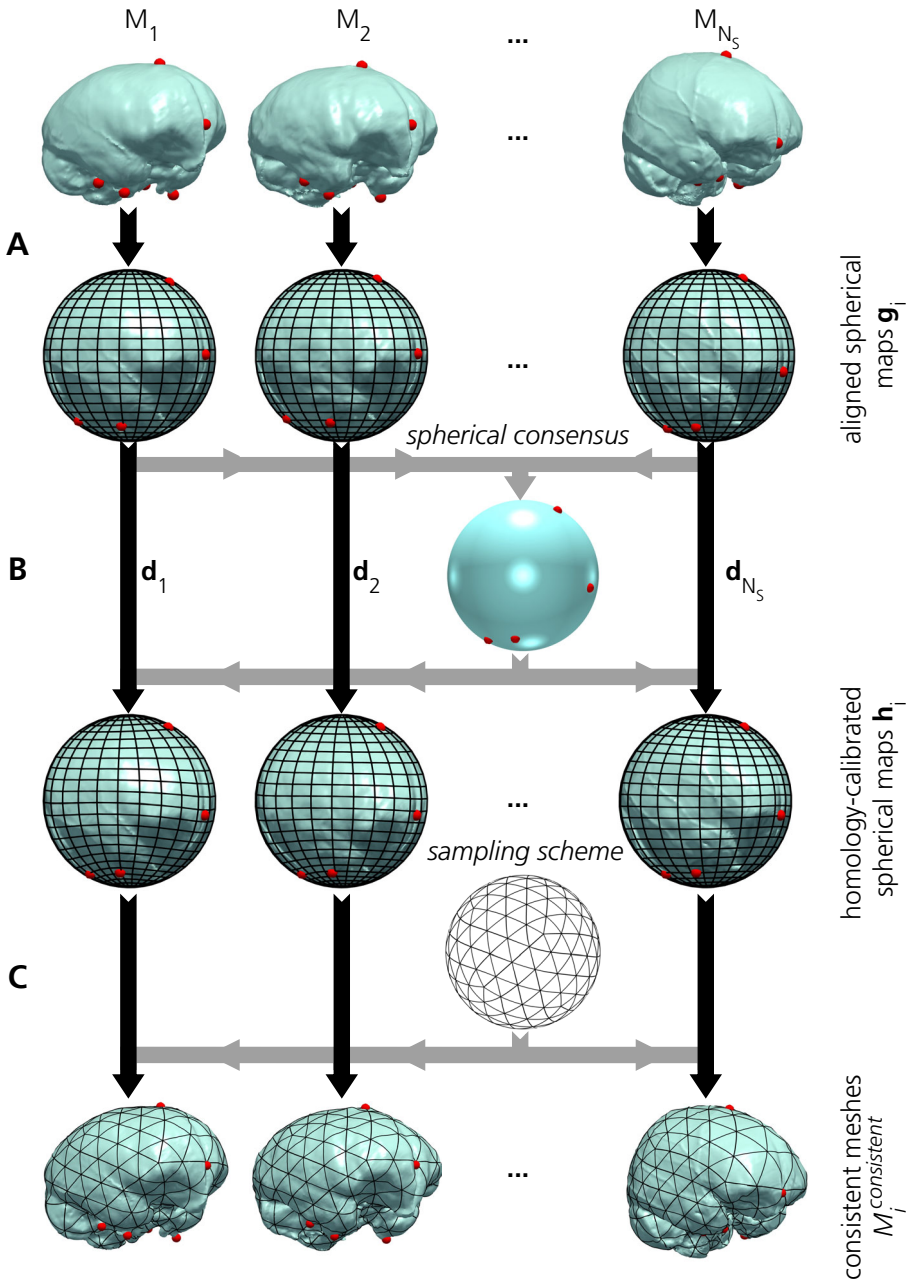

Figure 3.1: Pictorial overview of the calculation of our consistent spherical parameterization. **A**: The original surfaces are mapped to the sphere. **B**: the maps are deformed such that the biological features (homologies) match their spherical consensus. **C**: The spherical domain is sampled, e.g., with a Loop-subdivided spherical icosahedron, to consistently remesh the original surfaces.

3.1.1 Spherical Parameterization

The first step of our pipeline is to find piecewise linear and bijective mappings (i.e., homeomorphisms) $\mathbf{f}_i$ from the original triangle meshes M_i to the unit sphere S^2:

$$\mathbf{f}_i : M_i \rightarrow S^2 : (x, y, z) \mapsto (\theta, \phi), \qquad i \in [1, N_S] \tag{3.3}$$

This step poses a major challenge, since such a parameterization is not straightforward like sampling an outline in a equidistant fashion (which can be seen as parameterizing an outline on the unit circle). To compute a valid (i.e., manifold - no flipped triangles) spherical parameterization of a non-star-shaped closed surface is a demanding task itself. We saw in section 2.2 that a variety of valid parameterizations exist, based on different optimization strategies. The optimization criteria define the properties of the resulting parameterization. For now, we only assume the $\mathbf{f}_i$ to be valid spherical parameterizations.

3.1.2 Calibration of the Parameter Domain

In order to fulfill requirement 1 (eq. 3.2), we need to find good target positions for the images of the landmarks on the sphere and then deform the spherical maps $\mathbf{f}_i$ such that the images of the landmarks match on the sphere. To minimize the average distortion introduced by the deformation, we evaluate mean landmark positions from the spherical maps $\mathbf{f}_i$.

We rigidly align the spherical parameterizations $\mathbf{f}_i$ by generalized least squares minimization (GLS) of the spherical landmark distances to obtain the aligned sets $\mathbf{g}_i$. The procedure is shown in fig. 3.2. We use an algorithm based on (Gower, 1975) and adapted to

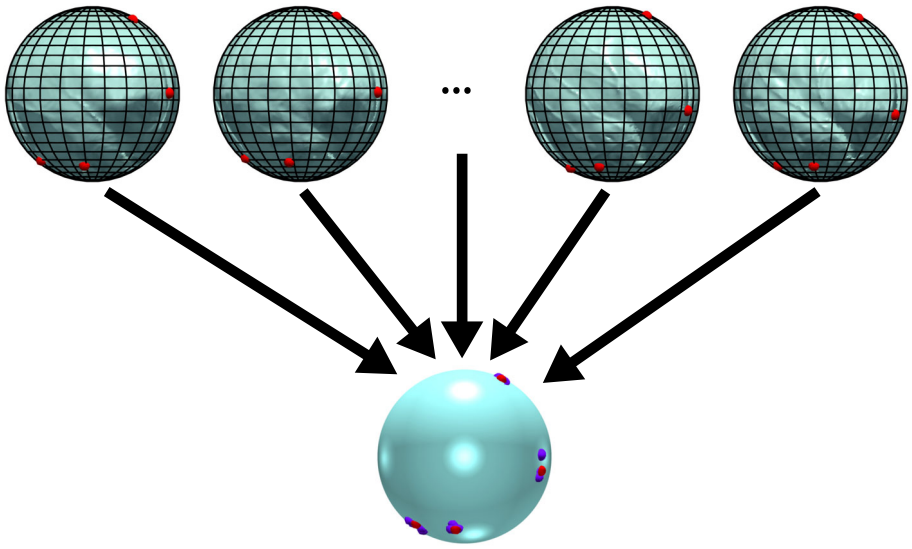

Figure 3.2: GLS-alignment of the spherical parameterizations and calculation of the spherical consensus.

spherical geometry (see appendix B.1). The *spherical consensus* $C = \{\mathbf{c}_1, \mathbf{c}_2, ..., , \mathbf{c}_{N_L}\}$ is the set of mean landmarks projected onto the unit sphere

$$\mathbf{c}_j = normalize\left(\sum_{i=1}^{N_S} \mathbf{g}_i(\mathbf{l}_{i,j})\right), \qquad j \in [1, N_L] \tag{3.4}$$

The aligned maps $\mathbf{g}_i$ must now be deformed such that the mapped landmark sets match C. We use the algorithm from Glaunès et al. (2004) to construct a unique deformation map $\mathbf{d}_i : S^2 \mapsto S^2$ such that

$$\mathbf{d}_i(\mathbf{g}_i(\mathbf{l}_{i,j})) = \mathbf{c}_j \qquad \forall \text{ points } \mathbf{l}_{i,j} \tag{3.5}$$

for each surface by integration of vector fields that minimize a quadratic smoothness energy, based on geodesic distances, under the landmark constraint $L_i \rightarrow C$ on the sphere.

The spherical maps $\mathbf{g}_i$ can be deformed with the deformation diffeomorphisms $\mathbf{d}_i$:

$$\mathbf{h}_i = \mathbf{d}_i \circ \mathbf{g}_i, \tag{3.6}$$

thus constraining the geometry with the biological data. Because both $\mathbf{d}_i$ and $\mathbf{g}_i$ are bijective, $\mathbf{h}_i$ is bijective as well, and so is $\mathbf{h}_i^{-1}$.

3.1.3 Sampling and Remeshing

A spherical parameterization $\mathbf{h}$ of a triangle mesh M denotes a triangulation of the sphere and defines a bijective, piecewise linear mapping from the sphere to the surface.

A position $\mathbf{s}$ on the sphere is approximated by a position $\mathbf{s}'$ on the mesh $\mathbf{h}$. The location of $\mathbf{s}'$ in its containing triangle can be expressed by its *homogeneous barycentric coordinates* (see fig. 3.3) with respect to the vertices $\mathbf{v}_0^*, \mathbf{v}_1^*, \mathbf{v}_2^*$ of the triangle

$$\mathbf{s}' = a \cdot \mathbf{v}_0^* + b \cdot \mathbf{v}_1^* + c \cdot \mathbf{v}_2^* \tag{3.7}$$

where

$$a + b + c = 1. \tag{3.8}$$

The corresponding position $\mathbf{p}$ on the original surface, in the triangle $\mathbf{v}_0, \mathbf{v}_1, \mathbf{v}_2$ is defined by the same coordinates ($\mathbf{p} = a \cdot \mathbf{v}_0, b \cdot \mathbf{v}_1, c \cdot \mathbf{v}_2$).

Equiangular Sampling Grid

A natural way to describe positions on the sphere are *spherical polar coordinates* (see fig. 3.4). θ is the polar angle (or zenith, colatitude) with $\theta \in [0, \pi]$ and ϕ the azimuthal angle with $\phi \in [0, 2\pi[$. The angle iso-lines form an orthogonal grid, which permits intuitive navigation on the sphere and can be used to sample the surface.

According to the Nyquist sampling theorem (Nyquist, 2002), a band-limited function f of bandwidth B can be reconstructed from at least $2B$ samples without aliasing.

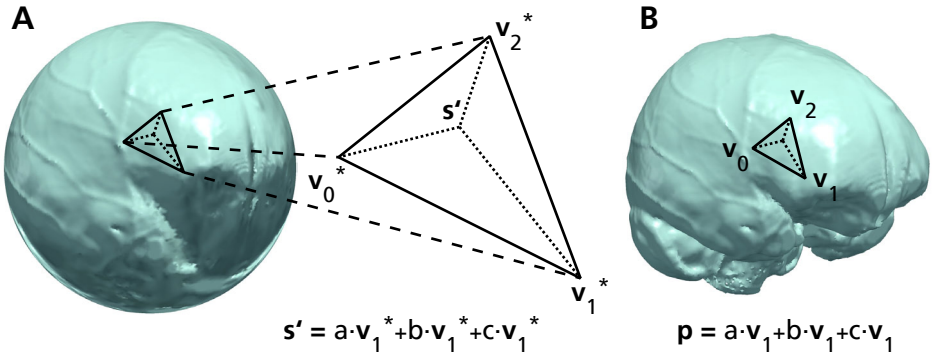

Figure 3.3: Sampling the surface on the spherical domain using barycentric coordinates. **A**: A position **s** on the sphere is approximated by the closest point $\mathbf{s}'$ on the spherical triangle mesh **h**. The barycentric coordinates a, b, c define the position of $\mathbf{s}'$ relative to the triangle corners $\mathbf{v}_0^*, \mathbf{v}_1^*, \mathbf{v}_2^*$. **B**: The barycentric coordinates are used to find the corresponding position **p** on the original mesh M.

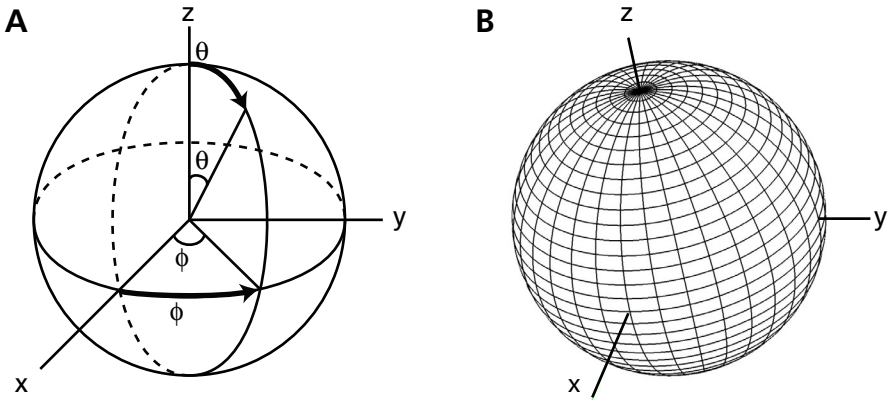

Figure 3.4: **A**: Spherical polar coordinates. θ is the polar angle (or zenith, colatitude) with $\theta \in [0, \pi]$ and ϕ the azimuthal angle with $\phi \in [0, 2\pi[$. **B**: The angle iso-lines form an orthogonal grid, which permits intuitive navigation on the sphere and can be used to sample the surface.

Therefore, an equiangular sampling grid with bandwidth B can be constructed (see also appendix A.1):

$$\theta_j = \frac{\pi(2j+1)}{4B}, \phi_k = \frac{2\pi k}{2B}. \tag{3.9}$$

In practice, it is not trivial to estimate the bandwidth of piecewise linear functions. In the next section, we will show how this can be done by looking at the reconstruction error.

Quasi-equidistant Sampling Scheme

In equiangular grids, point density is changing and there are singularities at the poles. Equi-spaced sampling schemes for the sphere provide an alternative. Unfortunately, there are no such patterns except those given by the five platonic solids. However, subdividing an icosahedron and projecting the new vertices to the sphere gives a good approximation (fig. 3.5). At subdivision level 0, we start with an icosahedron with 12 vertices and 20 triangles. Increasing the subdivision level results in addition of a new vertex in the center of every edge (like in Loop-subdivision, (Loop, 1987)), thus doubling the sampling rate and quadrupling the number of vertices. The new vertices are connected as shown in figure 3.5**A**, and are projected to the sphere. The bandwidth B of the sampled signal can be calculated from the subdivision level. At level l, there are $4^l \cdot 20$ triangles and $\frac{4^l \cdot 20}{2} + 2$ vertices in the mesh. Similar to (3.9), we define the bandwidth

$$B = \sqrt{\frac{N_{vertices}}{4}} = \sqrt{\frac{4^l \cdot 5 + 1}{2}}. \tag{3.10}$$

Note that the intuitive definition of coordinates such as azimuth and colatitude is not possible with this sampling scheme.

In the following, both sampling schemes will be applied, and its respective advantages will be assessed.

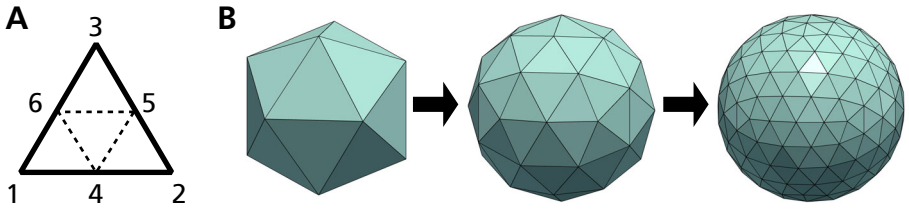

Figure 3.5: **A**: Loop-subdivision-scheme. The triangle 1-2-3 is subdivided by inserting new vertices 4,5,6 at the edge centers and is replaced by the 4 triangles 1-4-6, 4-2-5, 6-5-3 and 4-5-6. **B**: The subdivided icosahedron projected to the sphere. Subdivision levels are 0, 1 and 2 with 12, 42 and 162 vertices.

Remeshing

Sampling the surfaces over the spherical domain (i.e., the inverse mapping $\mathbf{h}_i^{-1}$) maps a sampling position (θ_k, ϕ_k) to a position $\mathbf{p}_k$ in R^3 onto the surface M_i. A spherical

sampling scheme, which is a tessellation of the sphere, is mapped to a mesh approximating M_i. Figure 3.1 shows the usage of the quasi-equidistant sampling scheme to obtain a set of remeshed surfaces $M_i^{consistent}$. We call them *consistent remeshes* because all $M_i^{consistent}$ share the same connectivity, and every vertex in the sampling scheme is mapped to a corresponding position on all $M_i^{consistent}$.

3.2 Evaluation of Optimization Methods

Except for the calculation of the spherical parameterizations $\mathbf{f}_i$, each step of the parameterization model presented above is uniquely defined. In this section, we compare the two different spherical parameterization strategies reviewed in section 2.2.6. First, let us define relevant criteria for the spherical parameterization.

3.2.1 Precision

The parameterization should be precise in the sense that there should be a well-defined parameterization for a given surface. Precision is measured by the variance of the position of the image vertices when a parameterization algorithm is run several times with different "environmental" factors, which play a role in the algorithm but are not supposed to influence its result, such as random seeds. Imagine a mesh M with N_v vertices being parameterized N times, resulting in spherical maps $\mathbf{f}_i, i \in [1, N]$. Applying the spherical GLS algorithm described above, we can align the $\mathbf{f}_i$ by minimizing the squared distances between the N images of every vertex and obtain the aligned maps $\mathbf{g}_i$. It is straightforward to calculate the mean Procrustes distance

$$d_{mean} = \frac{1}{N} \sum_{i=1}^{N} d_i, \tag{3.11}$$

where d_i is the Procrustes distance from parameterization $\mathbf{g}_i$ to the spherical consensus

$$d_i = \sqrt{\sum_{j=1}^{N_v} (\overline{\mathbf{v}_j} - \mathbf{v}_j^i)^2}, \tag{3.12}$$

where $\mathbf{v}_j^i$ are the vertices of the spherical mesh $\mathbf{g}_i$, and $\overline{\mathbf{v}_j}$ the corresponding vertices of the spherical consensus.

3.2.2 Accuracy

The similarity of the remeshed surface to the original mesh defines the accuracy of the parameterization. We use the *symmetric Hausdorff-distance* (Klein et al., 1996; Aspert et al., 2002) (see appendix B.2) between the two surfaces to measure the approximation error.

3.2.3 Comparison of Parameterization Methods

In order to verify the mesh parameterization theory introduced in section 2.2.6, we compare the results form the coarse-to-fine algorithm, which optimizes spherical stretch, with the global conformal parameterization.

A sample of 12 endocranial surfaces (4 gorillas, 4 humans, 4 chimpanzees) is used for the evaluation. Every surface consists of 5000 vertices and is parameterized on the sphere 5 times, each time with a different random seed. Then, precision d_{mean} is measured for every surface and the arithmetic mean is calculated for every species. The results (table 3.1) indicate that the global conformal spherical parameterization is *unique*, i.e., the precision is considerably higher than the one of the stretch-based parameterization. This result was expected from the discussion in chapter 2, because the stretch metric measures a mix of angle and area distortion, and area-preserving functionals significantly increase the DGF. Further, the nature of the algorithm (vertex-optimization in random directions within the polygon kernel) prevents it from converging to a global minimum. In contrast, the algorithm from Gu and Yau converges towards a well-defined and unique solution.

	gorilla	**human**	**chimpanzee**	**mean**
stretch	1.528	1.563	1.500	**1.530**
global conformal	<0.001	<0.001	<0.001	<**0.001**

Table 3.1: Comparison of the precision of parameterizations. The values are mean Procrustes distances, as defined in (3.11).

To measure the accuracy of the parameterizations, the surfaces are sampled on the sphere using the subdivided icosahedron sampling scheme. Various subdivision levels are used, and the symmetric Hausdorff distance between the original mesh and the sampled surface is measured. The average values for all parameterizations of the whole sample are plotted in fig. 3.6. The result confirms theoretical expectations. Increasing the subdivision level (i.e., the sampling frequency) of the sampling scheme reduces the sampling error, and because of the smaller area distortion, the stretch-based parameterization is significantly more accurate than the global conformal parameterization. For instance, a subdivision-level of 4.5, which results in a sampling scheme with bandwidth $B = 35.8$ (see eq. 3.10), results in a reconstruction error $\epsilon = 1.0\%$ of the bounding box diagonal for the stretch-minimizing parameterization. In contrast, to achieve the same accuracy using the global conformal parameterization, a subdivision-level of 6.2, i.e., a bandwith of $B = 116.2$, is needed.

Recapitulating, the global conformal parameterization is more precise, and the stretch-based parameterization is more accurate.

3.2.4 Conclusion

For our application, that is measuring and visualizing shape difference, a unique solution is essential. In order to find out whether the variability implied by the imprecision of the stretch-minimizing parameterization is large relative to shape variability between

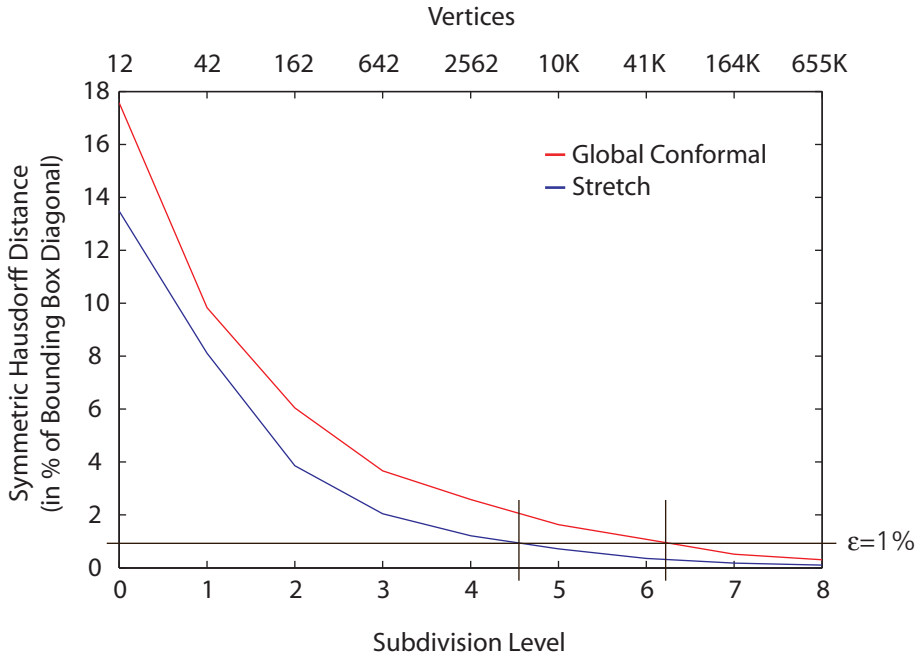

Figure 3.6: Accuracy of the parameterizations. The symmetric Hausdorff distance (average of the whole sample) between the original mesh and the sampled surface is plotted against the subdivision level of the sampling scheme. The stretch-minimizing parameterization yields a higher accuracy than the global conformal parameterization. For instance, a subdivision level of 4.5 (i.e., bandwidth $B = 35.8$) results in an error $\epsilon = 1\%$ using the stretch-minimizing parameterization. In contrast, a subdivision level of 6.2 (i.e., bandwidth $B = 116.2$) is necessary to achieve the same accuracy using the global conformal parameterization.

individuals, a PCA was applied on the gorilla-human-chimpanzee sample. The necessary theory is given in section 4.2. Figure 3.7 shows the plot of the first two PCs. The five parameterizations of each surface results in slightly different PC scores. In some cases (gorillas 3 and 4, chimpanzees 3 and 4), the variability between different parameterizations of the same surface is comparable to the variability between these individuals. Because the variability between different parameterizations is virtually zero, the global conformal parameterization is preferable.

On the other hand, an accurate parameterization (e.g., a small sampling error) is important as well. The stretch-based parameterization permits a near-uniform sampling of the surface. This results, for instance, in an accurate frequency spectrum of the shape, while over- and under-sampling of some areas will lead to a distorted spectrum.

However, there is no (obvious) way to increase the precision of the stretch-based

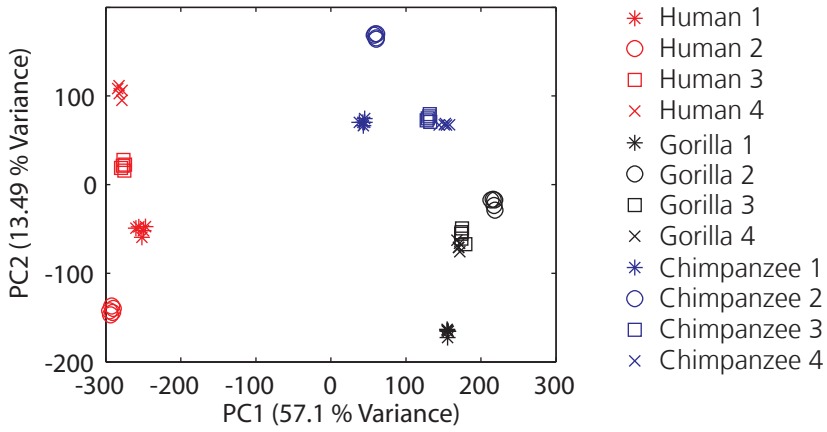

Figure 3.7: Precision of the stretch-minimizing parameterizations. Endocranial surfaces of gorillas, humans and chimpanzees were parameterized five times each, with different random seeds. A PC analysis was then applied on the semilandmarks as described in section 4.2, and PC1 is plotted against PC2. For some surfaces, such as gorillas 3 and 4 and chimpanzees 3 and 4, the variability between different parameterizations of the same surface is comparable to the variability between these individuals. This is not acceptable for measuring shape difference.

algorithm. In contrast, the reconstruction error can always be reduced by simply increasing the bandwidth of the sampling scheme. Further, the nature of our data (no extreme extrusions) and the zero mass-center condition of the global conformal parameterization prevent extreme area-distortion.

Moreover, because conformal maps locally preserve geometry, they are defined by the geometry rather than by triangulation (Gu et al., 2004). And the property of angle preservation permits visualization of shape difference by drawing an orthogonal deformation grid directly on the surface.

For these reasons, we will use the global conformal parameterization.

3.3 Geometric versus Biological Definition of Shape

The global conformal spherical parameterization is defined purely by geometric shape properties. Deforming the set of spherical parameterizations such that homologies become fixed locations on the sphere means *reducing geometric accuracy in favor of biological accuracy*. "Geometric accuracy" can be measured by the *harmonic energy* $E_{Harmonic}$ (2.54) of the parameterization (i.e., its deviation from conformality). A simple metric for "biological accuracy" is the number of landmarks used.

We performed a preliminary proof-of-concept study. The harmonic energy was measured on the 12 endocranial surfaces described in the last section after deformation to the

Landmarks	Number	Harmonic Energy
-	0	25.133
{1,2,3}	3	25.137
{1,2,3,6}	4	25.143
{9,10,11,12}	4	25.142
{3,4,5,7,8}	5	25.228
{3,13,14,15,16,17,18}	7	25.420
{3,13,14,15,16,17,18,19,20}	9	25.536
all	20	25.629

Table 3.2: Landmark sets used to measure the harmonic energy. The landmark numbers correspond to the landmarks defined in table 6.2.

spherical consensus for a number of landmark sets. We used eight different K-landmark sets from K=3 to K=20 landmarks. The landmarks are defined in table 6.2. Table 3.2 lists the landmark sets, the number of landmarks contained in each set ("biological accuracy") and the average harmonic energy of the deformed spherical parameterizations ("geometric accuracy"). The number of landmarks is plotted against the harmonic energy in figure 3.8. The harmonic energy correlates with the number of landmarks.

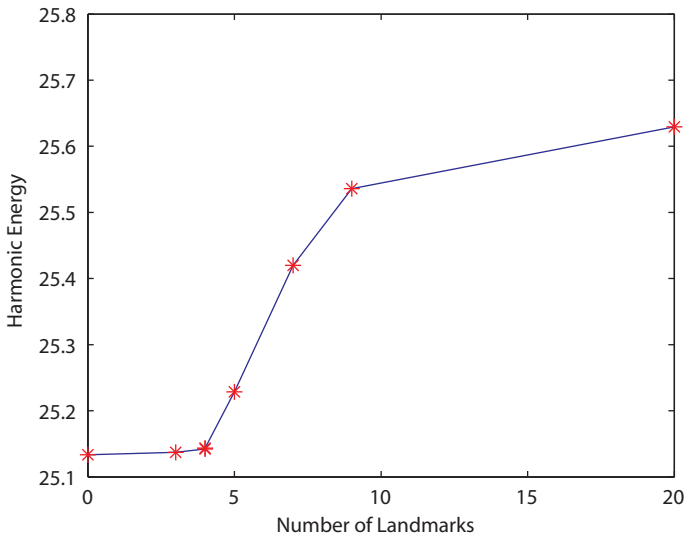

Figure 3.8: Geometry versus biology: The harmonic energy (abscissa) of the deformed spherical parameterization correlates with the number of landmarks (ordinate), indicating a decrease of "geometric accuracy" with the increase of "biological accuracy".

Chapter 4

Geometric Morphometric Analysis and Visualization

This chapter deals with how the homology-calibrated spherical parameterization can be used for statistical analysis and visualization of the results. Having the whole geometry parameterized on the sphere such that points of biological homology coincide on well-defined positions permits novel approaches to compare the shapes of specimens in a sample.

We will first present semilandmarks obtained through quasi-uniform sampling of the spherical domain. The number of semilandmarks is virtually unlimited, and the coordinates of the semilandmarks can be used for statistical analysis in the same way as the coordinates of traditional landmarks.

The second section introduces the Fourier transform of a 3D shape to the geometric morphometrics toolbox. This is of special interest since the level-of-detail ordering of the data permits a new, more visually guided interpretation of the results, and filter operations allow to focus on specific frequency components of the surface.

4.1 Size Normalization and Alignment

To measure the difference in shape, it is important to remove differences in size, position and orientation between the objects prior to the sampling of the surfaces. Classic geometric morphometrics uses centroid size from Procrustes superposition (see eq. 2.1) for size normalization. Here, we use the volume of the closed surface as a size measure, because it is a unique measure, independent of the number of landmarks.

First, the original surfaces M_i are size-normalized by scaling all vertices such that the volume becomes 1

$$M_i^{norm} = \frac{M_i}{\sqrt[3]{volume(M_i)}}. \tag{4.1}$$

Landmark-variability is then reduced by minimizing the sum of squared distances (GLS fitting, see appendix B.1).

4.2 Semilandmarks

The consistent homology-calibrated spherical parameterization defines a mapping for any position on the sphere to corresponding positions on every surface. In geometric morphometrics, such corresponding points are commonly called *semilandmarks*. Throughout this and the following sections, the term indicates that the 3D coordinates, i.e., the representation in Euclidean space, of the points are used (rather than the representation in Fourier space). Both sampling schemes introduced in section 3.1.3 define reasonable semilandmark distributions. However, because of the quasi-equal point distribution, the subdivided icosahedron sampling pattern described in section 3.1.3 is preferred in general.

4.2.1 Analysis of Shape Variability

Once the original surfaces are aligned, they are consistently remeshed as described in section 3.1.3. The resulting $\mathbf{p}_k^i$, where k is the vertex number and i the index of the shape, are corresponding points and can directly be used for statistical analysis. For such purposes, it is convenient to use a matrix form notation. Let $\mathbf{X}_i$ be a $3 \times N_v$ matrix with the 3D coordinates of N_v semilandmarks of surface i.

The average (or consensus) shape of N shapes is simply the arithmetic mean

$$\mathbf{C} = \frac{1}{N} \sum_{i=1}^{N} \mathbf{X}_i, \tag{4.2}$$

and the linear difference between two shapes is the matrix difference. The difference from an individual to the consensus shape is

$$\mathbf{V}_i = \mathbf{X}_i - \mathbf{C}. \tag{4.3}$$

A principal components analysis (PCA, see appendix B.3) to measure shape variability in the sample can be applied as follows:

1. Build the observation matrix $\mathbf{D}$:

$$\mathbf{D}^T = \begin{bmatrix} \mathbf{V}_{1_1} & \mathbf{V}_{1_2} & \mathbf{V}_{1_3} \\ \dots & \dots & \dots \\ \mathbf{V}_{i_1} & \mathbf{V}_{i_2} & \mathbf{V}_{i_3} \\ \dots & \dots & \dots \\ \mathbf{V}_{N_1} & \mathbf{V}_{N_2} & \mathbf{V}_{N_3} \end{bmatrix}, \tag{4.4}$$

   where $\mathbf{V}_{i_1}$ is the first row of $\mathbf{V}_i$. Row i of $\mathbf{D}^T$ contains all measures for specimen i ("specimen vector"), and $\mathbf{D}$ is a $3N_v \times N$ matrix.

2. Build the within-sample covariance matrix:

$$\mathbf{S} = \mathbf{D}\mathbf{D}^T. \tag{4.5}$$

3. Calculate the eigendecomposition with eigenvectors $\mathbf{E}$ and eigenvalues Λ

$$\mathbf{S} = \mathbf{E}\Lambda\mathbf{E}^T. \tag{4.6}$$

The $3N_v$ eigenvectors are the columns of the $3N_v \times 3N_v$ matrix $\mathbf{E}$.

4. Project the shapes onto the eigenvectors to find the PC scores:

$$\mathbf{P} = \mathbf{E}\mathbf{D}, \tag{4.7}$$

Element $\mathbf{P}_{ij}$ contains the score of shape j for eigenvector, or *principal component* (PC) i.

While all the above is similar to landmark-only shape space analysis, let us point out the advantages of our method:

Level-of-detail control. The number of semilandmarks, and therefore the level-of-detail or the amount of geometric information in the analysis, is controlled by a single parameter, the subdivision level (or bandwidth, respectively) of the spherical sampling scheme.

Full surface reconstruction. It is possible to *directly* transform a point $\mathbf{Q}$ from PC space back to a shape $\mathbf{R}$ in real space:

$$\mathbf{R} = \mathbf{C} + \mathbf{Q}\mathbf{E}^T, \tag{4.8}$$

i.e., no *a posteriori* surface interpolation (such as TPS interpolation) is necessary (the surface defined by the semilandmarks in $\mathbf{R}$ has the same connectivity as the sampling scheme).

4.2.2 Visualization of Shape Difference

A key issue in modern geometric morphometrics is visualization of results, notably differences between shapes, or patterns of shape variation. Our quantification allows for application of a number of powerful visualization algorithms. A fundamental advantage is the fact that the whole surface is quantified, i.e., the real-space projection of any point in high-dimensional PC space yields a complete surface.

Which visualization method is appropriate also depends on the medium available. For static media such as research papers, important results must be captured in a few pictures, while the additional dimension of time can be exploited for interactive tools in the form of animations. For instance, trajectories in PC space can be mapped to a 3D shape and rendered in real-time.

In this section, we present concepts for such visualizations. They will be applied on actual data in chapter 6.

Drawing a Consistent Coordinate System on the Surfaces and Texturing

Once a consistent parameterization for a set of surfaces is obtained, a coordinate system can be drawn on the parameterization domain and mapped to the surfaces. Corresponding points on each surface have the same spherical coordinates (θ, ϕ). Drawing an equiangular coordinate system on the sphere produces spherical quadrangles with spherical angles approaching right angles ("orthogonal coordinate system"). A conformal map to a surface preserves the angles and produces approximations to rectangles on the surface. The stronger the (biologically defined) deformation $\mathbf{d}_i$ (eq. 3.5), the larger the deviation from conformality; this is observable in the non-linear deformation of the grid on the surface, which resembles Thompson's deformation grids.

Spherical coordinates can be drawn on the surfaces as a wireframe on top of the surface. Using texture mapping as a more general approach, any rectangular image can be used to texture the surface since the spherical coordinates of the vertices can directly be used as texture coordinates:

$$u = \frac{\phi}{2\pi}, \qquad v = \frac{\theta}{\pi}. \tag{4.9}$$

The positions of the M_i^{norm} and the spherical coordinate system are important for the visual appearance of the deformation grid. If a subset of the landmarks defines a symmetry plane, we can use them to position the M_i^{norm} in a canonical way : We rotate all surfaces such that the symmetry plane of the average surface lies in the xz-plane.

We usually position the coordinate system such that the poles are on the z-axis, the 0-meridian passes through (1, 0, 0), and the equator lies in the xy-plane However, the poles of the spherical coordinate system are problematic areas for visualization. When there is no need for a specific position of the coordinate system in space, we can fix the spherical grid to the camera such that the poles are always on top and bottom. In practice, if we look at a surface in a 3D viewer and rotate the object relative to the camera with rotation matrix A, we transform the texture coordinates with A^T. This is equivalent to the projective texture mapping technique where a (planar) image is projected onto a 3D scene, like a slide projection.

Morphing

Our parameterization permits the definition of a morphing function from the surface M_{from} to surface M_{to} by linear vertex interpolation. In matrix notation this looks as follows:

$$\mathbf{X}_{inter} = (1-t) \cdot \mathbf{X}_{from} + t \cdot \mathbf{X}_{to}, \qquad t \in [0, 1]. \tag{4.10}$$

Combined with displaying an orthogonal coordinate system on the surface, interactive blending between the shapes is a powerful way to interactively explore shape difference. Actually, linear combination of shapes is not limited to just two shapes. It is straight-forward to build a weighted sum of any number of shapes.

Visualization of Relative Shape Transformation on the Surface

From the consistent parameterizations, scalar or vector fields can be calculated and visualized directly on the surface. The method for visualizing shape variation proposed in (Zollikofer and Ponce de León, 2002) was implemented.

Direction and magnitude of shape transformation: To compare a surface M_i^{norm} to a reference surface M_R^{norm}, the displacement vector $\mathbf{d}^k$ for every spherical sampling position (θ_k, ϕ_k) is calculated:

$$\mathbf{d}^k = \mathbf{p}_i^k - \mathbf{p}_R^k. \tag{4.11}$$

The displacement vector $\mathbf{d}^k$ is then decomposed into its normal and tangential components (relative to the surface in $\mathbf{p}_R^k$):

$$\mathbf{d}^k = \mathbf{d}_\perp^k + \mathbf{d}_{||}^k. \tag{4.12}$$

$\mathbf{d}_{||}^k$ is visualized as an arrow glyph attached to $\mathbf{p}_i^k$, and the length and direction of $\mathbf{d}_\perp^k$ is color-coded on the surface.

Local growth: Local relative growth at vertex $\mathbf{p}^k$ on the surface can be calculated by comparing triangle areas:

$$b^k = \log\left(\frac{A_i^k}{A_R^k}\right), \tag{4.13}$$

with A_i^k the area of the 1-ring of $\mathbf{p}^k$ on M_i^{norm} and A_R^k the corresponding area on M_R^{norm}. The scalars b^k are visualized by coloring the surface.

4.3 Fourier Descriptor

The spherical harmonics transform (SHT, see appendix A.1) expands a sampled spherical signal into a generalized Fourier series using the spherical harmonics as basis functions and therefore permits *harmonic analysis of surfaces*. As in the two-dimensional case, the analysis of outlines, the gain of transforming a quantitative shape description from Euclidean to frequency space lies in qualitative interpretation of the components (i.e. numbers) in the description.

The *degree* ℓ of a coefficient c_ℓ^m is basically its frequency. This forms a natural *level-of-detail ordering*: the higher the ℓ, the finer the detail described the according c_ℓ^m. The spherical harmonics have global support, therefore every coefficient contains global shape information.

In this section, we present a compact matrix representation of the Fourier descriptor for a 3D surface and define operations and analysis techniques on that representation.

4.3.1 Spherical Harmonic Transform of Surfaces

The SHT expands a spherical signal $f(\theta, \phi)$ into a generalized Fourier series using the spherical harmonics $Y_\ell^m(\theta, \phi)$ as basis functions. Sampling a surface actually results in a three-dimensional signal $\mathbf{f}$, which can be handled by independently processing each of its components as a scalar signal. Using the vector notation

$$\mathbf{f}(\theta, \phi) = \begin{pmatrix} x(\theta, \phi) \\ y(\theta, \phi) \\ z(\theta, \phi) \end{pmatrix}, \tag{4.14}$$

we can write the SHT as

$$\mathbf{f}(\theta, \phi) = \sum_{\ell \geq 0} \sum_{|m| \leq \ell} \mathbf{c}_\ell^m Y_\ell^m(\theta, \phi) \tag{4.15}$$

where ℓ is the *degree* and m the *order* of the spherical harmonic function, and

$$\mathbf{c}_l^m = \begin{pmatrix} c_{lx}^m \\ c_{ly}^m \\ c_{lz}^m \end{pmatrix}. \tag{4.16}$$

The complex coefficients $\mathbf{c}_\ell^m$ of the SHT form the SPHARM descriptor of the surface $\mathbf{f}$ and express the same surface as the spatial coordinates $\mathbf{f}(\theta, \phi)$ of the vertices on the equiangular sampling grid on the original mesh, but in the frequency domain. This means the influence of a coefficient on the shape defined by the whole descriptor can be qualified. The number of coefficients in a frequency band increases with increasing ℓ. This leads to a pyramid-like structure of complex coefficients in three dimensions, see table A.1.

The total number of spherical harmonic coefficients directly depends on the bandwidth B of the spherical function $\mathbf{f}$ or the number of sampling points on the equiangular sampling grid, respectively (see appendix A.1). The spherical function is sampled using an equiangular sampling grid with $4B^2$ sampling points, as described in section 3.1.3. For every degree ℓ, $0 \leq \ell < B$, there are $1 + 2\ell$ complex coefficients for each spatial dimension, see table A.1.

For convenience, we use the real and imaginary parts of the complex numbers as independent real numbers. This means the $4B^2$ sampling values can be reconstructed from $2B^2$ real numbers (i.e., from $\sum_{\ell=0}^{B-1} 1 + 2\ell = B^2$ complex values). However, some properties of the spherical harmonic coefficients $\mathbf{c}_\ell^m$ can be exploited to further reduce the storage needs. Because of the redundancy

$$Y_\ell^{-m} = (-1)^m Y_\ell^{m*}, \qquad m \geq 1, \tag{4.17}$$

(see (A.2) in appendix A.1), the coefficients $\mathbf{c}_\ell^{-m}$ (i.e., the coefficients with negative order) are not necessary to describe the signal accurately and can be discarded. However, we need to scale the $\mathbf{c}_\ell^m, m > 0$ with $\sqrt{2}$ because the set of orthogonal functions

$\{Y_\ell^0, \mathrm{Re}(Y_\ell^1), \mathrm{Im}(Y_\ell^1), ...\}$ are not normalized (Brechbühler, 1995). Further, each $\mathbf{c}_\ell^0$ is a real-valued vector, i.e., the imaginary part is zero. Therefore, using the SHT, a scalar spherical signal $f(\theta, \phi)$ with bandwidth B can be expressed by

$$\sum_{\ell=0}^{B-1} 1 + 2\ell = B^2 \tag{4.18}$$

real values. For a surface, the SHT transforms $4B^2 \cdot 3 = 12B^2$ real-valued values to $3B^2$ real-valued coefficients. Note the significant data reduction.

Therefore, the spherical harmonic coefficients can be written in the compact form of a $3 \times (B^2 + B)$ matrix

$$\mathbf{S} = \begin{bmatrix} \mathbf{a}_0^0 & \mathbf{b}_0^0 & \mathbf{a}_1^0 & \mathbf{b}_1^0 & \mathbf{a}_1^1 & \mathbf{b}_1^1 & \dots & \mathbf{a}_{B-1}^{B-1} & \mathbf{b}_{B-1}^{B-1}, \end{bmatrix} \tag{4.19}$$

where $\mathbf{a}_\ell^m$ and $\mathbf{b}_\ell^m$ are three-valued vectors containing the real and imaginary parts of $\mathbf{c}_\ell^m$:

$$\mathbf{a}_\ell^m = k \begin{bmatrix} \mathrm{Re}(c_{\ell x}^m) \\ \mathrm{Re}(c_{\ell y}^m) \\ \mathrm{Re}(c_{\ell z}^m) \end{bmatrix}, \qquad \mathbf{b}_\ell^m = k \begin{bmatrix} \mathrm{Im}(c_{\ell x}^m) \\ \mathrm{Im}(c_{\ell y}^m) \\ \mathrm{Im}(c_{\ell z}^m) \end{bmatrix}, \qquad k = \begin{cases} 1, & \text{if } m = 0 \\ \sqrt{2}, & \text{else} \end{cases} \tag{4.20}$$

Note that we kept the the B $\mathbf{b}_\ell^0$, which are all zero, in order to simplify the indexing scheme. The indices of $\mathbf{a}_\ell^m$ and $\mathbf{b}_\ell^m$ are $\ell^2 + \ell + 2m$, and $\ell^2 + \ell + 2m + 1$, respectively.

Concluding, we can write the SHT in matrix form:

$$\mathrm{SHT}(\mathbf{M}) = \mathbf{S}, \tag{4.21}$$

where $\mathbf{M}$ is a $3 \times 4B^2$ matrix with the Euclidean coordinates of the (sampled) surface, and $\mathbf{S}$ as defined above.

4.3.2 Analysis of Shape Variability

The matrix form permits an elegant formal definition of a set of powerful operations on the shapes. Because the SHT is a linear transformation (because c_l^m is defined by an integral (see eq. A.6), and the integral is a linear operator),

$$\mathrm{SHT}(\mathbf{M}_1 + \mathbf{M}_2) = \mathbf{S}_1 + \mathbf{S}_2 \tag{4.22}$$

and

$$\mathrm{SHT}(\alpha \cdot \mathbf{M}) = \alpha \cdot \mathbf{S} \tag{4.23}$$

hold. Therefore, the difference between two surfaces $\mathbf{S}_1$ and $\mathbf{S}_2$ is

$$\mathbf{M}_1 - \mathbf{M}_2 = \mathrm{SHT}^{-1}(\mathbf{S}_1 - \mathbf{S}_2), \tag{4.24}$$

and their mean

$$\frac{1}{2}(\mathbf{M}_1 + \mathbf{M}_2) = \mathrm{SHT}^{-1}\left(\frac{1}{2}(\mathbf{S}_1 + \mathbf{S}_2)\right). \tag{4.25}$$

Filtering

Filters are important for analysis because they permit to restrict the analysis to a certain area of the spectrum. It is straight-forward to apply filters in the frequency domain. The basic idea is to scale all coefficients of degree ℓ to amplify or dampen the components with a given frequency. This can be written by a matrix multiplication:

$$\mathbf{S}' = \mathbf{SF} = \mathbf{S} \begin{bmatrix} f_0 & 0 & . & . & . & 0 \\ 0 & f_1 & . & . & . & 0 \\ . & . & . & & & . \\ . & . & & . & & . \\ . & . & & & . & . \\ 0 & 0 & . & . & . & f_{B^2+B} \end{bmatrix}, \tag{4.26}$$

where $\mathbf{S}'$ contains the coefficients of the filtered Surface and the $(B^2 + B) \times (B^2 + B)$ *filter matrix* $\mathbf{F}$ contains the scaling factors on the diagonal. In order to change components of degree ℓ, the coefficients $f_{\ell^2+\ell}, ..., f_{(\ell+1)^2+\ell}$ need to be set to the scaling factor.

Low pass filter To cut all frequencies (degrees) above L_{lp}, we set

$$f_i = \begin{cases} 1, & \text{if } i < L_{lp}^2 + L_{lp} \\ 0, & \text{if } i \geq L_{lp}^2 + L_{lp}. \end{cases} \tag{4.27}$$

High pass filter To cut all frequencies (degrees) below L_{hp}, we set

$$f_i = \begin{cases} 0, & \text{if } i < L_{hp}^2 + L_{hp} \\ 1, & \text{if } i \geq L_{hp}^2 + L_{hp}. \end{cases} \tag{4.28}$$

Band pass filter To only allow frequencies within range $[L_a, L_b[$ to pass, we set

$$f_i = \begin{cases} 1, & \text{if } L_a^2 + L_a \leq i < L_b^2 + L_b \\ 0, & \text{else.} \end{cases} \tag{4.29}$$

In the same way, stop-band filters can be designed. To enhance a frequency range, a scaling factor larger than 1 is used.

Distance calculation

Distance metrics, such as the Hausdorff distance used in section 3.2 to measure precision, can be used to express the similarity of two objects with a single number. Parseval's theorem, which basically says that the integral of the square of a function is equal to the integral of the square of its transform, holds for the SHT because of the orthogonality of the spherical harmonic basis functions. This allows us to compute the Root Mean Squared (RMS) Distance ($\sqrt{MSD}$) between two objects directly from their coefficients

via a difference calculation. Gerig et al. (2001) write the MSD between two surfaces described by SPHARM descriptors $\mathbf{c}_1$ and $\mathbf{c}_2$, respectively, as

$$MSD = \frac{1}{4\pi} \cdot \sum_{\ell=0}^{B-1} \sum_{m=-\ell}^{l} |\mathbf{c}_{1,\ell}^m - \mathbf{c}_{2,\ell}^m|^2 \tag{4.30}$$

where $\frac{1}{4\pi}$ is a correction term, necessary because the squared spherical harmonics basis functions integrate to 4π rather than to 1. Using our matrix notation, (4.30) can be expressed as

$$MSD = \frac{1}{4\pi} \cdot ||\mathbf{S}_1 - \mathbf{S}_2||_F^2 \tag{4.31}$$

where $||\mathbf{S}||_F$ is the *Frobenius norm* (or Euclidean norm) of matrix $\mathbf{S}$.

Distance matrix Distances between a set of objects can be used to build a *distance matrix* and perform a cluster analysis to construct a *dendrogram*. While this can be done directly with the aligned original surface meshes, the calculation in (4.31) can be applied in conjunction with filters, thus allowing the exploration of the similarity between objects in subregions of their spectrum.

Energy spectrum

Since the spherical harmonics Y_ℓ^m for a non-negative integer ℓ and and integer m with $|m| \leqslant \ell$ span a rotation-invariant subspace of $L^2(S^2)$, a descriptor can be built with the L^2 norms, which is invariant to rotations in original space (Kazhdan et al., 2003; Gu et al., 2004):

$$p_\ell = \sum_{i=1}^{3} \sum_{|m| \leq \ell} |c_{\ell i}^m|^2 \tag{4.32}$$

where $c_{\ell i}^m$ are the spherical harmonics coefficients of the 3-valued spherical signal and i is the index of the coordinate axis. Using the matrix notation

$$p_\ell = \sum_{i=\ell^2+\ell}^{\ell^2+3\ell+1} |\mathbf{S}_i|^2, \qquad \ell \in [0, B[, \tag{4.33}$$

where $\mathbf{S}_i$ is the i^{th} column of $\mathbf{S}$.

Because of this rotation-invariance, the shape descriptor formed by vector $\mathbf{p}$ actually permits the comparison of surfaces *without any alignment in object and parameter space*. Only size-normalization is needed, which can be done by normalizing the volume, or the length of the main axis of the first-order ellipsoid. Therefore, no landmarks would be necessary to perform that kind of analysis. However, it is not possible to reconstruct the original surface from its energy spectrum, which excludes its use for advanced visualization purposes.

PCA

To apply a PCA on the frequency spectrum of N surfaces, we fill the descriptors $\mathbf{S}^i$ into a matrix $\mathbf{X}$ such that row i contains all coefficients of the i-th surface:

$$\mathbf{X} = \begin{bmatrix} \mathbf{S}_1^{1T} & \mathbf{S}_2^{1T} & ... & \mathbf{S}_{B^2+B}^{1T} \\ ... & ... & ... & \\ \mathbf{S}_1^{NT} & \mathbf{S}_2^{NT} & ... & \mathbf{S}_{B^2+B}^{NT} \end{bmatrix}, \tag{4.34}$$

where $\mathbf{S}_k^1$ is the k-th column of $\mathbf{S}^1$, resulting in a $(N \times 3(B^2 + B))$ matrix. Each row is of the form

$$\begin{bmatrix} \mathbf{a}_{0,0}^0 & \mathbf{a}_{0,1}^0 & \mathbf{a}_{0,2}^0 & \mathbf{b}_{0,0}^0 & \mathbf{b}_{0,1}^0 & \mathbf{b}_{0,2}^0 & ... & \mathbf{b}_{B-1,0}^{B-1} & \mathbf{b}_{B-1,1}^{B-1} & \mathbf{b}_{B-1,2}^{B-1} \end{bmatrix} \tag{4.35}$$

The PCA is then applied as described in appendix B.3. The result is the same as the PCA on the semilandmarks, and the decomposition of the eigenvectors permits calculation of a "influence spectrum" which measures the contribution of a frequency toward that eigenvector. Each eigenvector $\mathbf{e}_j$ defines a direction in the high-dimensional space of all $3B^2+3B$ spherical harmonics basis functions and can be projected into every subspace of degree ℓ, analogous to (4.32). The squared length $d_{j\ell}$ of the projection

$$d_{j\ell} = \sum_{i=3\ell^2+3\ell}^{3\ell^2+9\ell+5} e_{ij}^2, \tag{4.36}$$

where the e are the elements of the matrix $\mathbf{E}$ containing the j^{th} eigenvector $\mathbf{e}_j$ in the j^{th} column (see eq. B.11), measures the relative contribution of degree ℓ. $\sum_\ell d_{j\ell} = 1$ for all j because the eigenvectors are normalized.

4.3.3 Visualization of Shape Difference

The inverse spherical harmonics transform (SHT^{-1}) is used to transform spherical harmonic coefficients to a surface, therefore enabling observation of the effects or results of the operations and methods introduced above in real space. For instance, the loss of detail when applying a low-pass filter can be monitored (fig. 6.4). This is especially important when interpreting patterns of shape variation detected by the PCA. Because any (synthetic) point p in PC space can be transformed to a set of spherical harmonic coefficients, the corresponding surface can be constructed using the SHT^{-1}. Thus, we can draw both the spectrum and the 3D surface connected to p. This is especially interesting for interactive explorative data analysis, as we will see in the next chapter.

Chapter 5

Implementation

The implementation of the theory presented in the last two sections has been carried out in two parts (see figure 5.1). First, the methods for spherical mesh parameterization and sampling to a consistent mesh described in chapter 3 have been implemented as a set of short standalone programs and shell scripts. Second, the statistical analysis techniques and visualization paradigms from chapter 4 have been implemented as a set of classes for the MorphoTools application framework described in section 2.5.

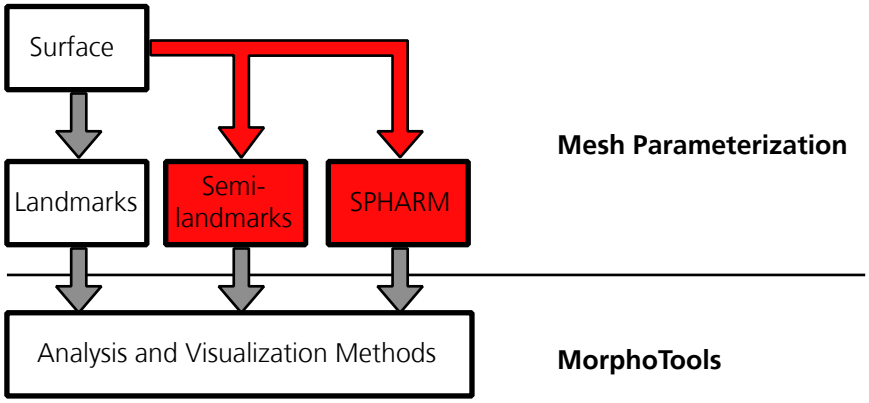

Figure 5.1: Implementation.The algorithms for mesh parameterization are implemented separately. For analysis and visualization, extensions for the MorphoTools framework were written.

This chapter first gives implementation details of the software components used for the mesh parameterization step. The results of this step are the semilandmark and SPHARM representations of the original surface. Next, an overview of the architecture of MorphoTools is given. Finally, the extensions of MorphoTools, which permit interactive handling of the new surface representations, are described.

5.1 Mesh Parameterization and Sampling

The OpenMesh[1] library (Botsch et al., 2002) was used to implement the mesh processing algorithms. OpenMesh provides convenient and efficient access to polygon meshes through the use of template concepts of the C++ programming language and implements the so-called *halfedge data structure* (sometimes also called *doubly-connected edge list* (de Berg et al., 2000) or *directed edges* (Campagna et al., 1998), see (Kettner, 1999) for an overview and comparison) to store the mesh entities such as vertices, faces, edges and their connectivity information. We mainly used the available features to iterate through all mesh vertices (or faces) and its neighbors. The functionality of the classes documented below was then used to write simple programs which can read, process and write triangle meshes. Our format of choice is the .obj file format introduced by Alias|Wavefront. Certain formats, such as STL, are not appropriate because vertex-ids are not guaranteed to be retained on load/store operations.

5.1.1 Spherical Parameterization

Figure 5.2 shows the hierarchy of the classes implemented for spherical mesh parameterization.

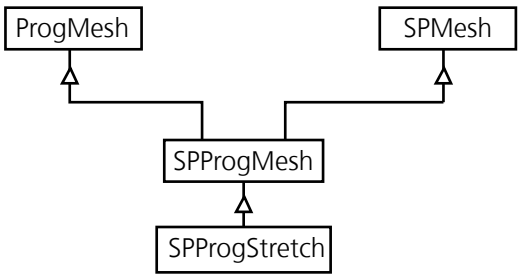

Figure 5.2: `SPMesh` class hierarchy.

The class `SPMesh` was defined as a starting point for the implementation of the spherical parameterization techniques. It provides a set of convenience methods for spherical geometry (see listing 5.1):

Listing 5.1: SPMesh provides convenience methods for spherical geometry.

```
class SPMesh : public TriangleMesh
{
  double angBetUnitVect(Point u,v);
  double calcSTAngle(Point C,A,B);
```

[1] See `http://www.openmesh.org` for more information.

```
  bool findIntersectingPoints(Point& p1,p2, Point v,R,A,B);
  Point pointOnGC(Point V,R, double ang);

  list<Point> listPoints calcKernel(VertexHandle v);
};
```

Angles. Angles play an important role in spherical geometry. `angBetUnitVect()` calculates the angle (arc length) between two unit vectors (i.e., two points on the sphere), and `calcSTAngle()` calculates the angle in point A between the tangents of the great circles AC, AB.

Great circles. A standard scenario is to find the two points where two great circles intersect, therefore the method `findIntersectingPoints()`. To find a point in a given distance in a given direction on the sphere, the method `pointOnGC()` can be used.

Spherical polygon kernel. The *kernel* of a spherical polygon is defined as the intersection of the open hemispheres defined by the polygon edges. Finding the kernel of a spherical polygon is essential for the spherical parameterization algorithm described in the next section. The method `calcKernel()` calculates the kernel.

`ProgMesh` is a simple progressive mesh (Hoppe, 1996) implementation. OpenMesh contains a progressive mesh file format and example code for decimation (edge collapses) and reconstruction (vertex splits). The decimation example was used to decimate the input mesh to a tetrahedron and construct the progressive mesh. `ProgMesh` provides code to read a progressive mesh structure (base mesh and vertex split information) and successively insert the vertices until the original mesh is reconstructed.

`SPProgMesh` is derived from both `SPMesh` and `ProgMesh` to implement the spherical parameterization algorithm proposed by Praun and Hoppe (2003). Listing 5.2 shows the algorithm to calculate a spherical embedding.

Listing 5.2: Coarse-to-fine spherical parameterization code.

```
project the tetrahedron to the unit sphere;
int n0 = 4;
int n = n0;
do {
  v = vertexsplit();
  k = calcNeighbourKernel(v);
  v = centerOfGravity(k);
  optimizePoint(v);
  for(w is neighbor of v) {
    optimizePoint(w);
  }
  n++;
  if(n == 2*n0) {
```

```
    do {
      for(Vertex v=vertices.begin(); v!=vertices.end(); v++) {
        optimizeVertex(v);
      }
    } while(largest vertex change < threshold);
    n0 = n;
  }
} while(not all vertices inserted);
```

The coarse-to-fine vertex insertion strategy, and the fact that inserted vertices always lie in the polygon kernel of its neighbors, guarantee a valid spherical embedding at any time of execution of the algorithm. Because of this robustness, the algorithm is well-suited for combination with various triangle distortion metrics. The distortion metric is used to optimize the position of a vertex in its 1-ring-kernel such that the (area-weighted) sum of all triangle distortions in the 1-ring becomes minimal, see listing 5.3. The `SPProgMesh.optimizeVertex()` method is virtual and implemented in the subclasses. We only implemented the original spherical stretch metric (Praun and Hoppe, 2003) resulting in the classes `SPProgStretch`.

Listing 5.3: Optimizing a vertex position.

```
void SPMesh::optimizeVertex(VertexHandle &v, int Nd) {
  k = calcKernel(v);
  double d = calc1RingDistortion(v);
  double distortions[Nd];
  Point positions[Nd];
  for(int i=0; i<Nd, i++) {
    Point R = (RND, RND, RND);
    R.normalize();
    Point p1=-v, p2=-v;
    // find arc segment of VR within kernel
    for(each edge AB in k) {
      Point q1, q2;
      findIntersectingPoints(q1, q2,  v, R, A, B);
      if(angBetUnitVect(v,q1) < angBetUnitVect(v,p1)) p1 = q1;
      if(angBetUnitVect(v-q2) < angBetUnitVect(v-p2)) p2 = q2;
    }
    double d1 = calc1RingDistortion(p1);
    double d2 = calc1RingDistortion(p2);

    fitParabola(distortions[i],positions[i], v,d,p1,d1,p2,d2);
  }
  find j with minimal distortions[j] and move v to positions[j]
}
```

Global Conformal Parameterization

The algorithm to calculate the global conformal spherical parameterization is from Gu et al. (2004) and starts with a valid spherical (Tutte) embedding and then iteratively optimizes vertex positions until the harmonic energy converges. We use the algorithm above (listing 5.2) to calculate the starting embedding. Implementation of the rest of the algorithm from the original paper is straight-forward using OpenMesh, see listing 5.4.

Listing 5.4: Global conformal parameterization.

```
void calcGlobConfPararam(Mesh morlg,msph) {
  double k[nEdges] = calcWeights(morig);
  double E = harmonicEnergy(msph, k);
  double E0;
  do {
    E0 = E;
    for(Vertex v=msph.vertices.begin(); v!=msph.vertices.end();
        v++) {
      calculate absolute derivative D(v);
    }
    for(Vertex v=msph.vertices.begin(); v!=msph.vertices.end();
        v++) {
      v = v - D(v)*dT;
    }
    Point c = msph.massCenter();
    for(Vertex v=msph.vertices.begin(); v!=msph.vertices.end();
        v++) {
      v = v - c;
      v.normalize();
    }
    E = harmonicEnergy(msph, k);
  } while(E0 - E > threshold);
}
```

5.1.2 Sampling on the Sphere

Figure 5.3 shows the hierarchy of the classes used for sampling on the spherical domain. The actual sampling is performed in the `Sampler` class which has references to the original mesh and a sampling scheme and contains the embedding of the original mesh on the sphere. The `Sampler.sample()` method finds a position on the original mesh for every vertex of the sampling scheme using barycentric coordinates, see listing 5.5.

Listing 5.5: Spherical sampling.

```
PolygonMesh Sampler::sample() {
  PolygonMesh ms = sscheme;
  for(VertexIterator vit=sscheme.vertices_begin(); vit!=sscheme.
      vertices_end(); ++vit) {
```

```
    Face tri = findClosestTriangle(vit);
    double u,v,w;
    findBarycentricCoordinates(u,v,w, tri,vit);
    Point v0, v1, v2;
    getOriginalVertices(v0,v1,v2, vit);
    ms.vertex(vit) = w*v0 + u*v1 + v*v2;
  }
  return ms;
}
```

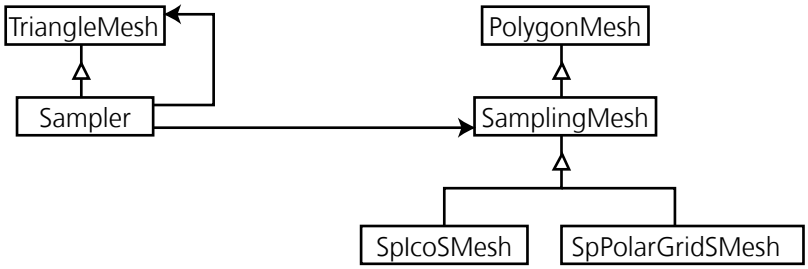

Figure 5.3: Hierarchy of the classes used for sampling on the spherical domain.

5.1.3 Alignment

For GLS alignment of the meshes and landmark configurations, the `vtkProcrustesAligmentFilter` class from the Visualization Toolkit (VTK, see next section) was used. Based on `vtkProcrustesAligmentFilter`, a rotation-only variant for alignment on the sphere was implemented, as described in appendix B.1.1. For the SPHARM descriptor, the landmark-free canonical positioning based on the first-order ellipsoid was implemented in C++, as described in appendix A.2.

5.1.4 Deformation on the Sphere

Dr. Joan Glaunés kindly provided his original C++ code to calculate the deformations on the sphere (see section 2.3.2). His code was embedded into our framework by implementing conversion tools from .obj files to his ASCII format (which is basically a discrete set of positions on the sphere) and back to .obj.

5.1.5 Spherical Harmonic Transform

The freely available *S2kit*[2] is used to calculate the SPHARM descriptor from the sampled surfaces. It implements the theory from (Healy et al., 2003).

[2]See `http://www.cs.dartmouth.edu/~geelong/sphere/` for more information.

5.2 The MorphoTools Framework for Shape Analysis and Visualization

Once the semilandmarks or the spherical harmonics, respectively, are calculated, established methods from multivariate statistics and scientific visualization can be used. The MorphoTools application framework proved to be especially suitable for this task because of its object-oriented design. Basic application classes take care of file-IO, sample selection and grouping and other elementary tasks. MorphoTools was extended to permit handling of the new samplings.

5.2.1 The MorphoTools Architecture

MorphoTools is an application framework which allows advanced scientific data visualization and exploration in the context of geometric morphometrics. At the core, it uses the Visualization Toolkit (VTK)[3] (Schroeder et al., 2003), which provides an extensive collection of visualization and data processing algorithms in the form of processing objects. These processing objects can be connected to build *visualization pipelines*.

Figure 5.4 shows the MorphoTools interface hierarchy. While the application itself is written in Java, additional VTK processing objects were written in C++. VTK compiles on all major platforms, and MorphoTools currently runs on Linux and Windows.

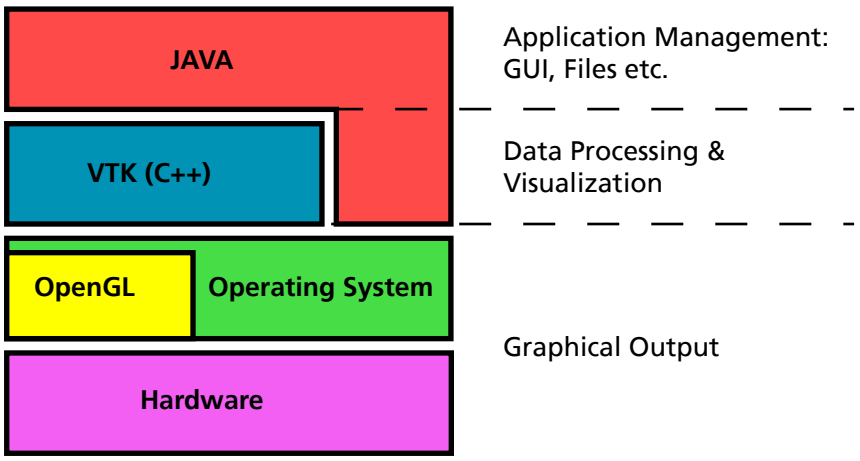

Figure 5.4: MorphoTools interface hierarchy.

[3] See `http://www.vtk.org` for more information.

Typical tasks occurring in a geometric morphometric analysis, such as loading a sample from disk, selecting specimens to be in- or excluded in the analysis etc., i.e., the *application logic*, are provided by the main application classes.

Figure 5.5 gives an overview over the interactions between the most important components in the MorphoTools application framework. The `Sample` class provides an interface to the actual data. It reads a *sample file* (the file format is defined in appendix D.1) from disk and instantiates the necessary classes using the MorphoTools object Factory. The main purpose of the `Factory` class is to map type names (i.e., strings) to actual classes. This facilitates extension of MorphoTools, because the knowledge about a specific data format is in the corresponding subclass, and both the basic GUI for selecting specimens, opening and closing views as well as the `Sample` class does not need to be changed.

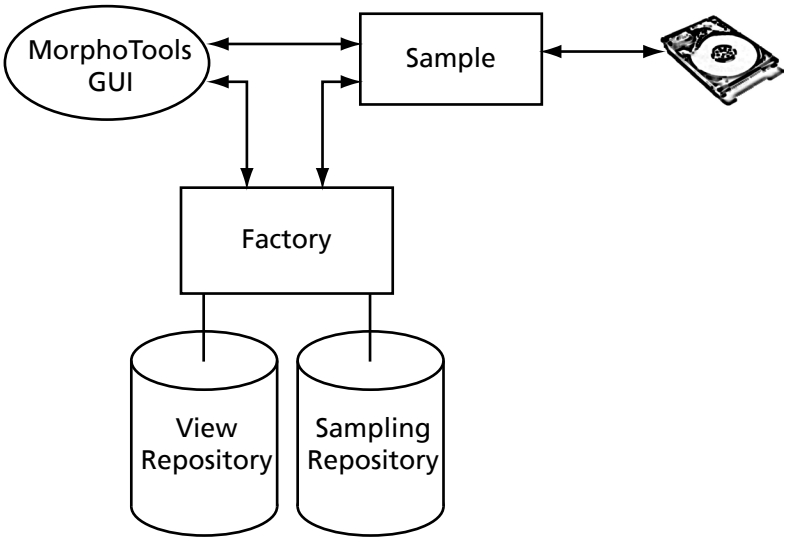

Figure 5.5: MorphoTools basic application logic and interaction diagram. The `Sample` class reads a sample file from disk and instantiates the necessary classes via the `Factory` class. The various parts of the GUI also interact with `Factory` to open user-selected views on the data and perform geometric morphometric analyses on a selected set of specimens.

The most important methods of the `Sample` and the `Factory` classes as well as the `Factable` interface are shown in fig. 5.6. The data contained in a sample file is basically a list of specimens, represented in one or several sampling styles, and additional properties such as *attributes* and *groups*. Attributes denote scalars such as “weight” or “age”, and groups denote discrete sets as “sex”, “species” etc. `Sample` contains the names of the at-

tributes and groups; the actual values are provided by the individual `Specimen` instances. The abstract `Specimen` class denotes acquired data about an individual prior to sampling, as well as one or more instances of `Sampling` subclasses. So far, the only implementation of `Specimen` is a specialization to contain a 3D `Surface`. Possible extensions are 2D outlines and images or 3D volumes.

Classes derived from `Sample`, `Sampling`, `SamplingView` and `AnalysisView` contain a unique type identifier (a string), which is used for interaction with `Factory`. The type naming scheme is straight-forward and permits to simply define classes to be instantiated in text files (see appendix D.1). The methods in `Factory` either create an instance defined by a type identifier or return a set of type identifiers for a given category. Java's `Cloneable` interface is used to define the `Factable` interface (see fig. 5.6), used in conjunction with `Factory`.

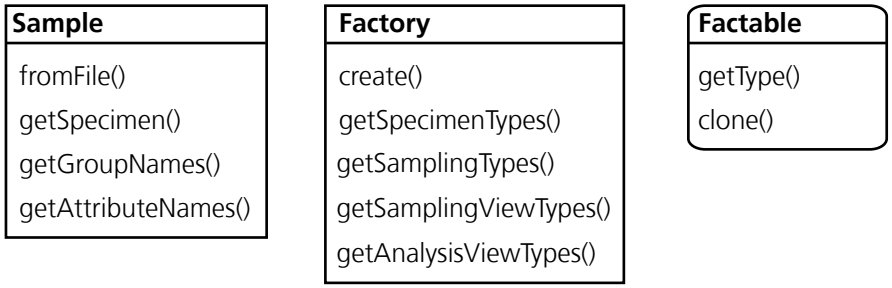

Figure 5.6: Most important public methods of the `Group` and the `Factory` classes and the `Factable` interface.

Once a sample is defined and loaded, a set of analysis and visualization paradigms can be applied on the data, each one being an implementation of an abstract `View` class. A `View` implementation typically consists of a VTK visualization pipeline and a GUI, and realizes a specific geometric morphometrics analysis pipeline. Therefore, researchers wishing to extend MorphoTools with a specific analysis or visualization paradigm only need to implement one subclass of `View`. They can concentrate on mapping their formal geometric morphometrics pipeline into a VTK processing object pipeline and designing a GUI using Swing components. The main application logic is provided by MorphoTools (see fig. 5.5).

The architecture of the MorphoTools application framework is based on the Model/View/Controller (MVC) paradigm (Krasner and Pope, 1988), see fig. 5.7. A specimen, in our case a 3D surface, can be represented in the form of various samplings. A sampling of a surface is a *Model* on which various *Views* can be opened. *Controllers* are used to change the data in a Model. Upon changes in a Model, all open Views get notified and updated. Java's `Observable/Observer` mechanism was used to implement the MVC paradigm.

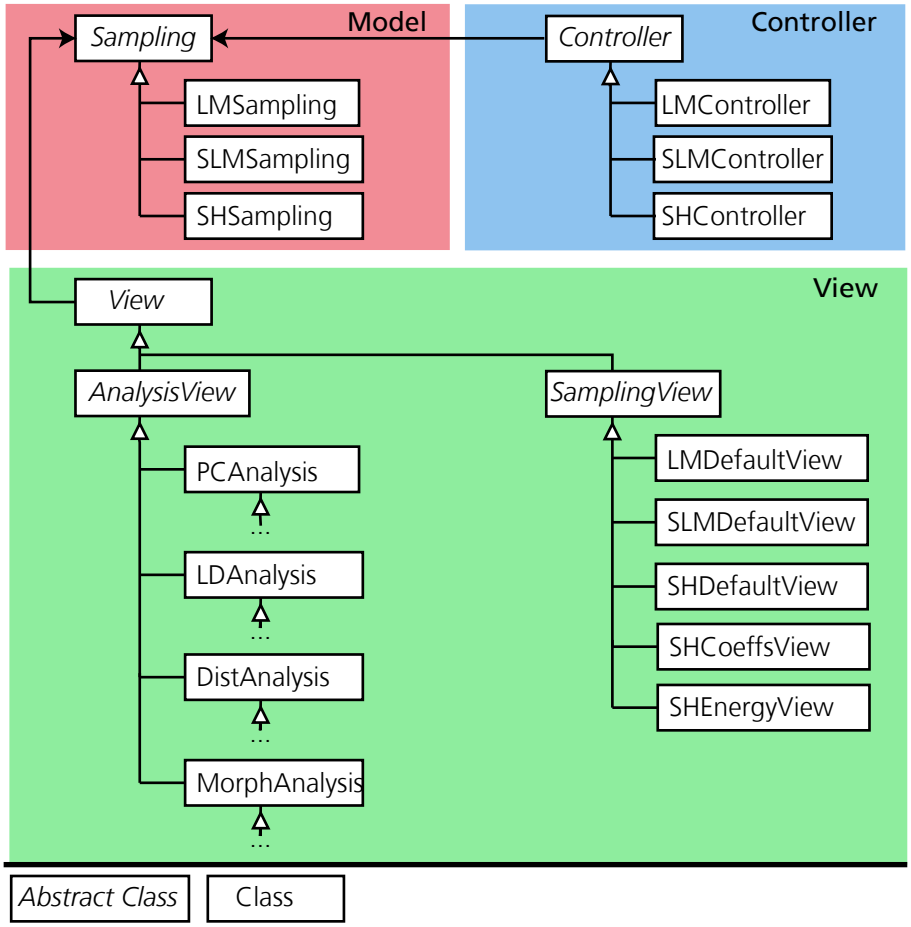

Figure 5.7: The hierarchy of the most important MorphoTools classes. The Model/View/-Controller paradigm is used.

The abstract `Sampling` class (see fig. 5.8) defines a generic interface to morphometric data, and concrete implementations (currently landmarks, semilandmarks and SPHARM) define how to read data from disk and transform it to (and from) instances of `vtkPointSet` for making it available for VTK pipelines.

The specializations contain methods to manipulate the data in the model, via dedicated `Controller` specializations (which are just GUIs for conveniently accessing these methods). For instance, the `LMController` allows to include or exclude landmarks from the analyses, the number of semilandmarks can be controlled with the `SLMController` and the frequency spectrum of the shape can be manipulated (i.e., filtered) with the `SHController`. Note that classes specialized for one particular sampling have a cor-

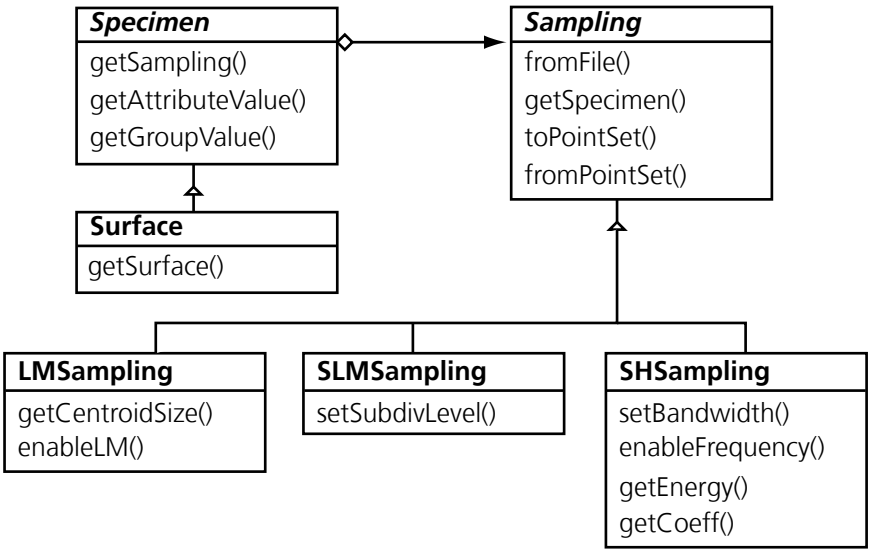

Figure 5.8: Relevant public methods of the `Specimen` and `Sampling` classes and subclasses.

responding prefix in their name ("`LM`" for LandMarks, "`SLM`" for SemiLandMarks and "`SH`" for Spherical Harmonics).

Most work has been done on writing the classes of the View package. There are two different types of views:

SamplingView A sampling view gives a visualization of one sampling instance, typically in a 3D viewer, possibly augmented with the original surface. Rendering parameters, such as camera position, lighting and more specific parameters like subdivision level etc., can be controlled through a GUI based on Swing components. Instances of `SamplingView` are often reused in `AnalysisView`.

AnalysisView An analysis view takes a set of samplings as input, performs some analysis on it and visualizes the results. This can be simple tables, 2D plots or complex 3D visualizations. A dedicated GUI provides parameter control. Implementations of `AnalysisView` can produce new `Sampling` instances, such as real-space projections from positions in feature space. Some `View` implementations, such as `PCAnalysis`, can be opened on any specialization of `Sampling`. However, often it is necessary to treat different samplings differently (e.g., when rendering), and specializations need to be written for the individual samplings.

Listing 5.6 shows the definition of the relevant parts of the `View`, `SamplingView` and `AnalysisView` classes (Java-based pseudo code). Upon instantiation, a `View` registers itself in the `Factory` with its type identifier. The type string uniquely identifies the `View` and which `Sampling` it handles. For instance, `view.sampling.sphericalharmonics.energy` defines a `SamplingView` for the SPHARM sampling, named "energy". The most important method in the Views is `update()`, which contains the actual implementation of a specialization; the different signatures directly reflect the difference between the `SamplingView`, which really is a view on one model, and `AnalysisView`, which is a view on a set of models.

All implementations of `AnalysisView` also support exporting the results to text files (comma-separated values, CSV). A list of currently implemented classes can be found in appendix A.2.

Listing 5.6: `View`, `SamplingView` and `AnalysisView` class definitions.

```
abstract public class View extends JPanel implements Factable,
    Observer {

  public String getType() { return _type; }
  public String getSamplingType() { return _samplingType; }

  // recalc & repaint
  public abstract void update();

  // Factable interface
  public String getType();
  public Object clone() ;

  // Observer interface
  public abstract void update(Observable o, Object arg);
}

abstract public class SamplingView extends View {
  public SamplingView(String type)
  {
    // find sampling type to handle:
    // type is view.sampling.<samplingtype>.<guiname>
    // build samplingtype = sampling.<samplingtype>
    int toindex = type.indexOf(".", 14);
    _samplingType = "sampling." + type.substring(14, toindex);
    _type = type;
    Factory.register((Factable)this);
  }
```

```
  // observer interface
  public void update(Observable o, Object arg) {
    _sampling = (Sampling)o;
    update();
  }
}


abstract public class AnalysisView extends View {
  public AnalysisView(String type)
  {
    // find sampling type to handle:
    // type is view.analysis.<samplingtype>.<guiname>
    // build samplingtype = sampling.<samplingtype>
    int toindex = type.indexOf(".", 14);
    _samplingType = "sampling." + type.substring(14, toindex);
    _type = type;
    Factory.register((Factable)this);
  }

  public void update(Sample[] samples) {
    // store all involved models and call update()
    _models = new SamplingModel[samples.length];
    for (int i = 0; i < samples.length; i++) {
      _models[i] = samples[i].getSampling(_samplingType).getModel
          ();
    }
    update();
  }

  // observer interface
  public void update(Observable o, Object arg) {
    update();
  }
}
```

5.2.2 VTK Pipelines for the Viewer Classes

In most implementations of the `View` class, VTK pipelines are created (figure 5.9). The OpenGL rendering context is integrated into the Java Swing components with the `vtkPanel` provided by the VTK package. Important input parameters of VTK processing objects are mapped to Swing components such as sliders, check boxes, combo boxes, edit fields, etc.

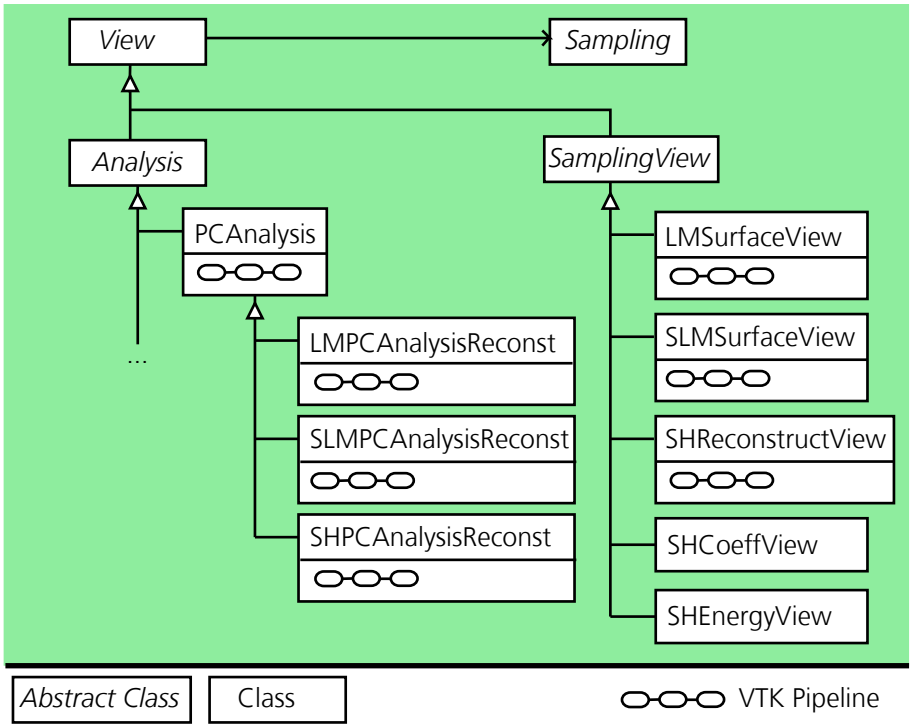

Figure 5.9: The class hierarchy of the analysis and visualization classes. Most implementations of the abstract `View` superclass contain a VTK pipeline. Implementations of `SamplingView` usually only make sense when specialized for one specific sampling, while some implementations of `AnalysisView` are generic, i.e., can handle any `Sampling` subclass (e.g., `PCAnalysis`). Implementations requiring more advanced visualizations often demand a sampling-specific specialization (e.g., `LMPCAnalysisReconst`, `SLMPCAnalysisReconst`, `SHPCAnalysisReconst`).

For instance, figure 5.10 shows the VTK pipeline of the `LMSurfaceView`. The landmarks, represented as a `vtkPointSet`, define where spherical glyphs are drawn as small spheres by the `vtkGlyph3D`. The `vtkPolyDataMapper` then translates the polygonal data to (OpenGL) graphics primitives, which are combined to an entity by a `vtkActor`.

Finally, the `vtkRenderer` renders the whole scene to an OpenGL context. The second branch of the pipeline renders the original surface, in order to put the landmarks in context of the biological structure.

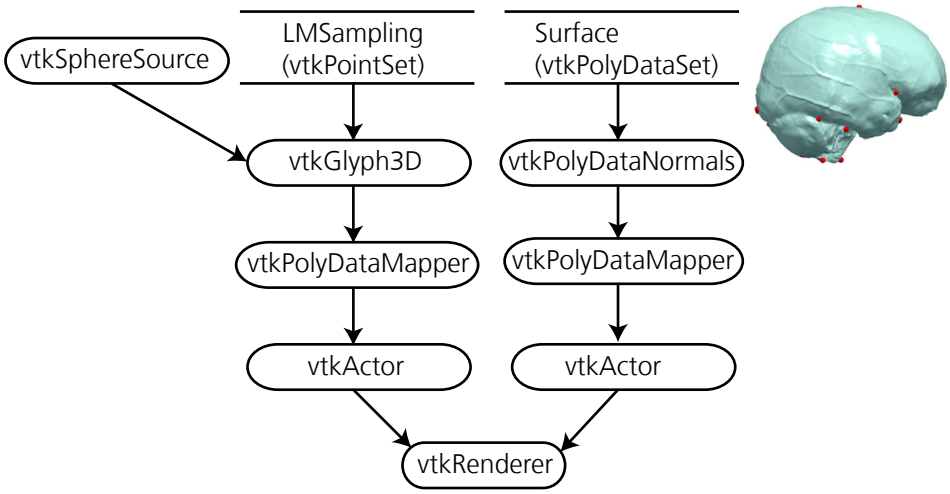

Figure 5.10: VTK pipeline for LMSurfaceView.

For the new samplings specific filters were implemented in C++ and added to the VTK repository to permit enhanced visualization. In the case of the semilandmarks (`SLMSurfaceView`, pipeline see fig. 5.11), it is not necessary to draw the original surface, because the semilandmarks are actually vertices of a Loop-subdivided icosahedron, i.e., the connectivity of the icosahedron can be used to construct a surface. A nice feature for visualization is to draw the mesh edges as a wireframe on top of the surface. However, in practice, it is usually desirable for the solid surface to be as detailed as possible, while the wireframe quickly clutter up the scene with increasing subdivision levels. Therefore we implemented the `vtkExtractIcoSubdivEdges` class which draws the edges of a (selectable) lower subdivision level with the accuracy of the higher subdivision level used for the surface.

Fig. 5.12 shows the pipeline for `SHReconstructView`. Since the spherical SPHARM coefficients are not in euclidean space, they must be transformed with the inverse SHT to obtain a (quadrilateral) surface. This is done by the `vtkSHCoeffsToPolyData` class. It also has a second output, with a coarser sampling grid at the full surface resolution. This allows again for a coarser wireframe annotation on the surface.

Subclasses of `AnalysisView` take a set of several `Sampling` instances as input. Figure 5.13 (left) shows the pipeline for the `PCAnalysis` class. Using the `Sampling.toPointSet()` method, the inputs are converted to `vtkPointSet`s. A PCA is applied and a scatterplot of the scores of two user-selectable PCs is rendered using `vtkXYPlotActor`. Thus `PCAnalysis` is generic in the sense that it can handle any `Sampling` specialization.

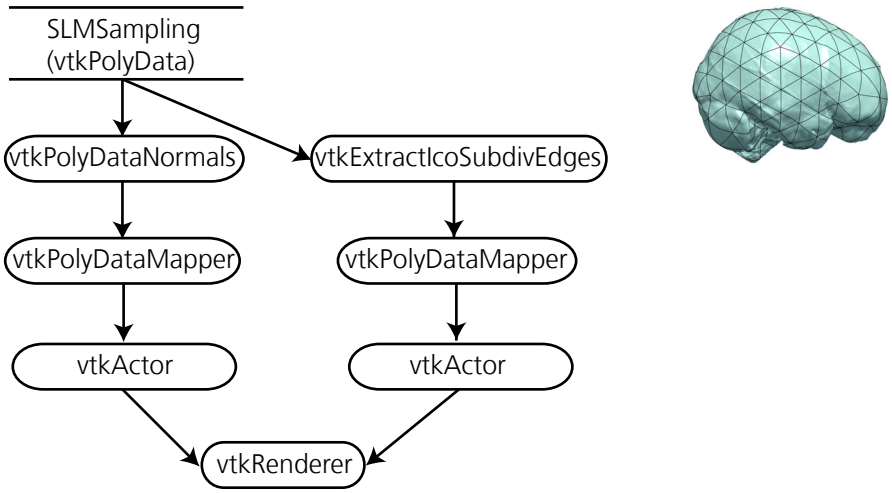

Figure 5.11: VTK pipeline for SLMSurfaceView.

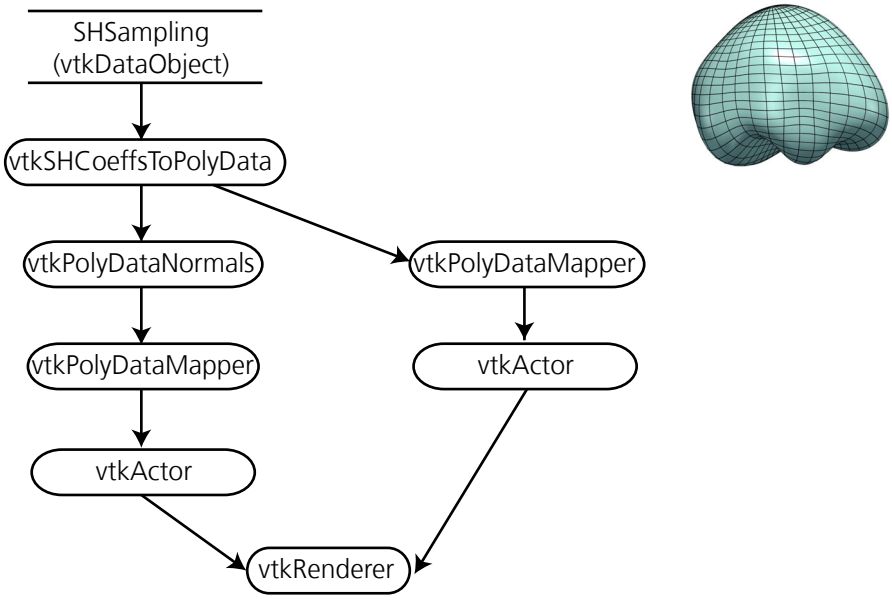

Figure 5.12: VTK pipeline for SHReconstructView.

However, for advanced visualizations, more knowledge about how to handle the information represented by a `vtkPointSet` (which can by constructed from a user defined position in PC space by `vtkPCAnalysis`) is necessary. Figure 5.13 (right) shows the extension for `SLMPCAnalysisReconst`: the `Sampling.fromPointSet()` method is used to obtain an instance of `SLMSampling`), and a `SLMSurfaceView`, which itself contains a VTK pipeline, is used to provide a real-space representation of the position in PC space. Specializations for landmark and SPHARM samplings are implemented in an analogous way, using `vtkTPSDeform` (TPS) and `vtkSHCoeffsToPolyData`, respectively.

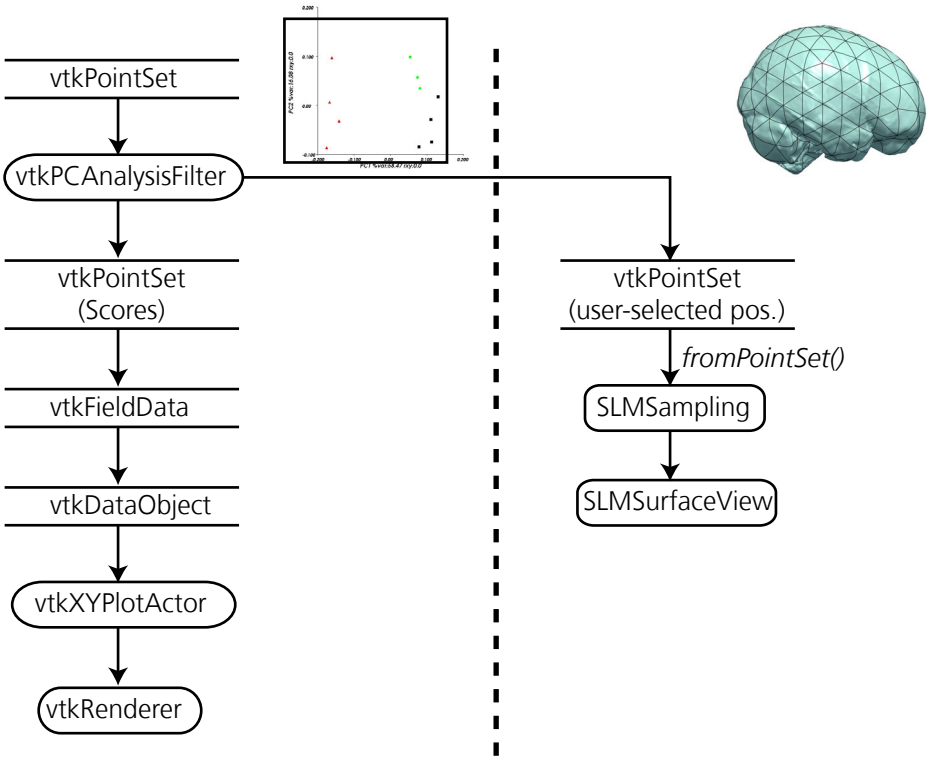

Figure 5.13: VTK pipeline for `PCAnalysis` (left) and extension to `SLMPCAnalysisMorph` (right). `PCAnalysis` operates on a number of `vtkPointSet` instances and thus can handle any `Sampling`. `SLMPCAnalysisMorph` is based on the same pipeline, but adds functionality to project a user-defined position in PC-space to real space (i.e., a `vtkPointSet`) and construct a `SLMSampling` (i.e., a surface) using `SLMSampling.fromPointSet()`. An instance of `SLMSurfaceView`, which contains a VTK pipeline itself, is then used to render the surface. Note that the extension is specific to semilandmark samplings, therefore, generality is lost.

Chapter 6

Application to Endocasts of Hominoids

This chapter considers how the methods developed in chapters 3 and 4 can be applied to quantitatively analyze shape variation in endocranial surfaces.

In the review in section 2.4, it was pointed out that morphometric analysis of the endocast is of high interest, and that there has been a lack of methods to efficiently assess the shape variation in endocranial surfaces.

The first section describes the materials and methods used. In the following sections, a set of case studies is carried out. First, shape variation within humans and great apes is measured using the consistent homology-calibrated spherical parameterization and Fourier analysis (i.e., the SPHARM descriptor). A comparison with a landmark-only method is given to validate the new approach, and the potential of Fourier analysis for visualization and interpretation is demonstrated. Next, the data is searched for patterns of left/right-asymmetry. Interactive tools are used to find and decompose patterns indicating frontal and occipital *petalia*. In the last section, visualization of shape transformation from the mean chimpanzee to the mean human endocast is examined, and a comparison to landmark-based TPS deformation is presented.

6.1 Materials and Methods

6.1.1 Sample

The sample consists of CT-based endocranial surfaces of adult modern humans (*Homo sapiens*), chimpanzees (*Pan troglodytes*), bonobos (*Pan paniscus*) and gorillas (*Gorilla gorilla*). Each species is represented by 2 male and 2 female endocasts. This sample was chosen to permit verification of the method and exploration of patterns of shape variability. Figure 6.1 shows all 16 endocranial surfaces, their names and the sex of the specimens, and table 6.1 lists the specimens' names in the database of the Morpholab of the Anthropological Institute of the University of Zürich.

Readers with limited expertise in taxonomy are referred to appendix C.1.

Species	**Short id**	**Sex**	**Collection id**	Collection
Homo sapiens	H1	female	BD1191	Natural History Museum, London
	H2	male	BMNH1025.4	
	H3	male	BMNH1915	
	H4	female	ONA1933	
Pan paniscus	P1	male	MRAC26939	Musée Royal de l'Afrique Centrale, Tervuren
	P2	male	MRAC26945	
	P3	female	MRAC29040	
	P4	female	MRAC29045	
Pan troglodytes	T1	male	AM6839	Collection of the Anthropological Institute, University of Zürich
	T2	male	AM7008	
	T3	female	AM7127	
	T4	female	AM7688	
Gorilla gorilla	G1	female	AM5563	
	G2	male	AM7406	
	G3	female	AM7420	
	G4	male	AM7666	

Table 6.1: Sample composition.

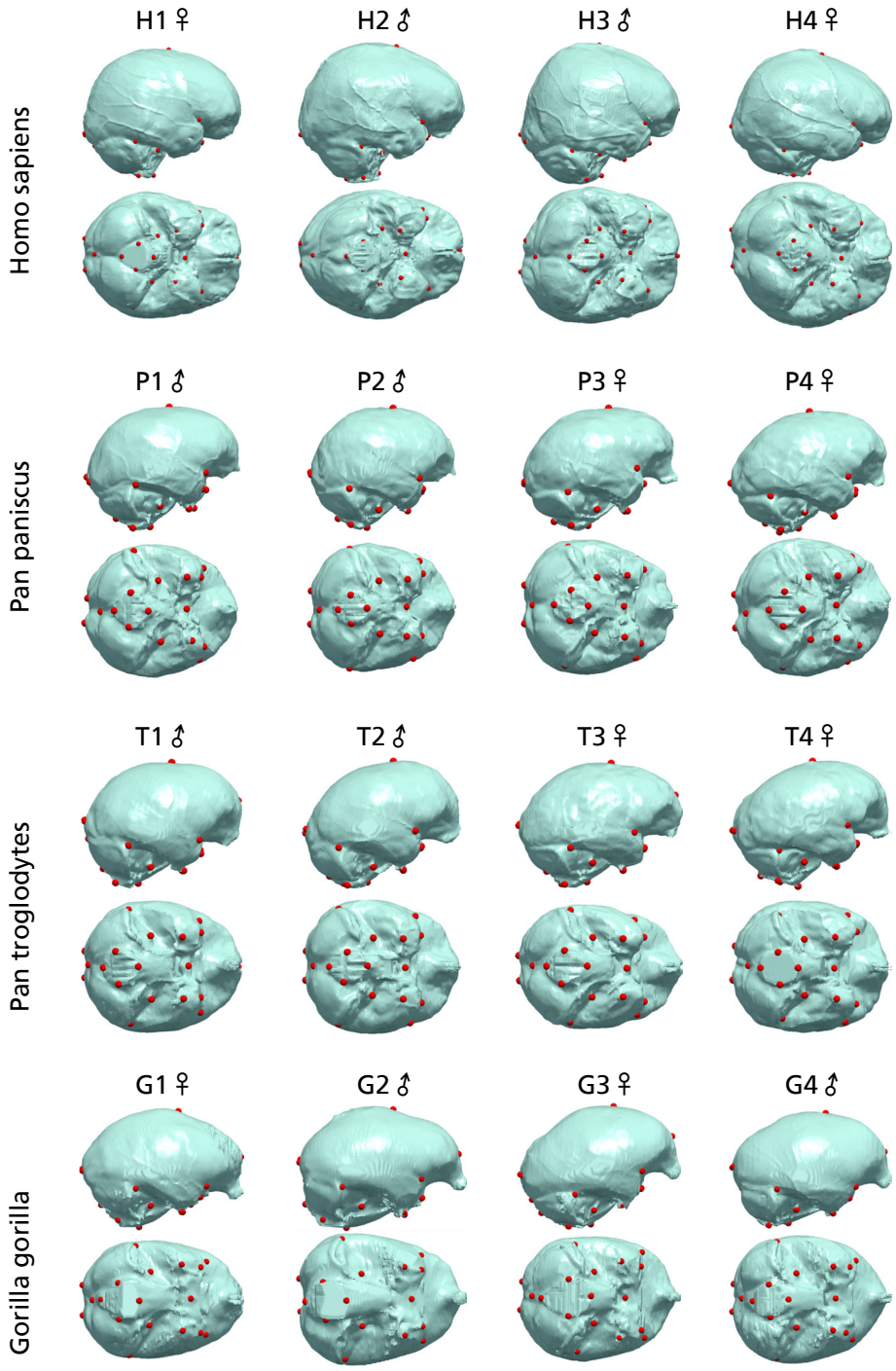

Figure 6.1: Sample of endocranial surfaces (see table 6.1). Volumes are normalized.

6.1.2 Endocranial Surface Extraction and Definition of Endocranial Landmarks

Triangle meshes were manually segmented from volumetric CT scans using the software Amira[1]. Depending on the resolution of the scanner, the meshes contained 100K to 700K vertices.

The endocranial surface of each individual was manually annotated with (K=20) homologous landmarks (see table 6.2). Six landmarks are located in the midsagittal plane and the 14 others in seven bilateral pairs. Figure 6.2 gives a detailed view on a human endocast (H3, male) with all landmarks.

Some of the landmarks are difficult to locate, and therefore error-prone. Therefore, a subset L_7 with (K=7) landmarks located at clearly recognizable foramina in the cranial base, and on well-defined points along the midplane of the braincase was defined. It consists of landmarks $\{1, 2, 3, 9, 10, 11, 12\}$.

Readers with no knowledge of anatomical terms are referred to appendix C.2 for a visual explanation of the basic expressions used in the following case studies to describe locations on the endocranial surface.

	Nr.	**Description**	**Remarks**
midsagittal	1	frontalmost point on endocranial surface	NOT on fossa anterior
	2	endobregma	skeletal landmark
	3	sinus sigmoideus at deepest point	cortex-cerebellum separation
	4	posteriormost point on foramen magnum	skeletal landmark
	5	anteriormost point on foramen magnum	skeletal landmark
	6	sella (inferiormost point)	hypophysis
bilateral	7,8	lateralmost points on foramen magnum	skeletal landmark
	9,10	porus acusticus internus	brainstem
	11,12	foramen ovale	brainstem
	13,14	anteriormost point on temporal lobe	cortex
	15,16	points on lateral fissure	cortex
	17,18	points on anterior edge of sinus sigmoideus	cortex
	19,20	occipital poles	cortex

Table 6.2: Endocranial landmarks.

[1] See `http://www.amiravis.com` for more information.

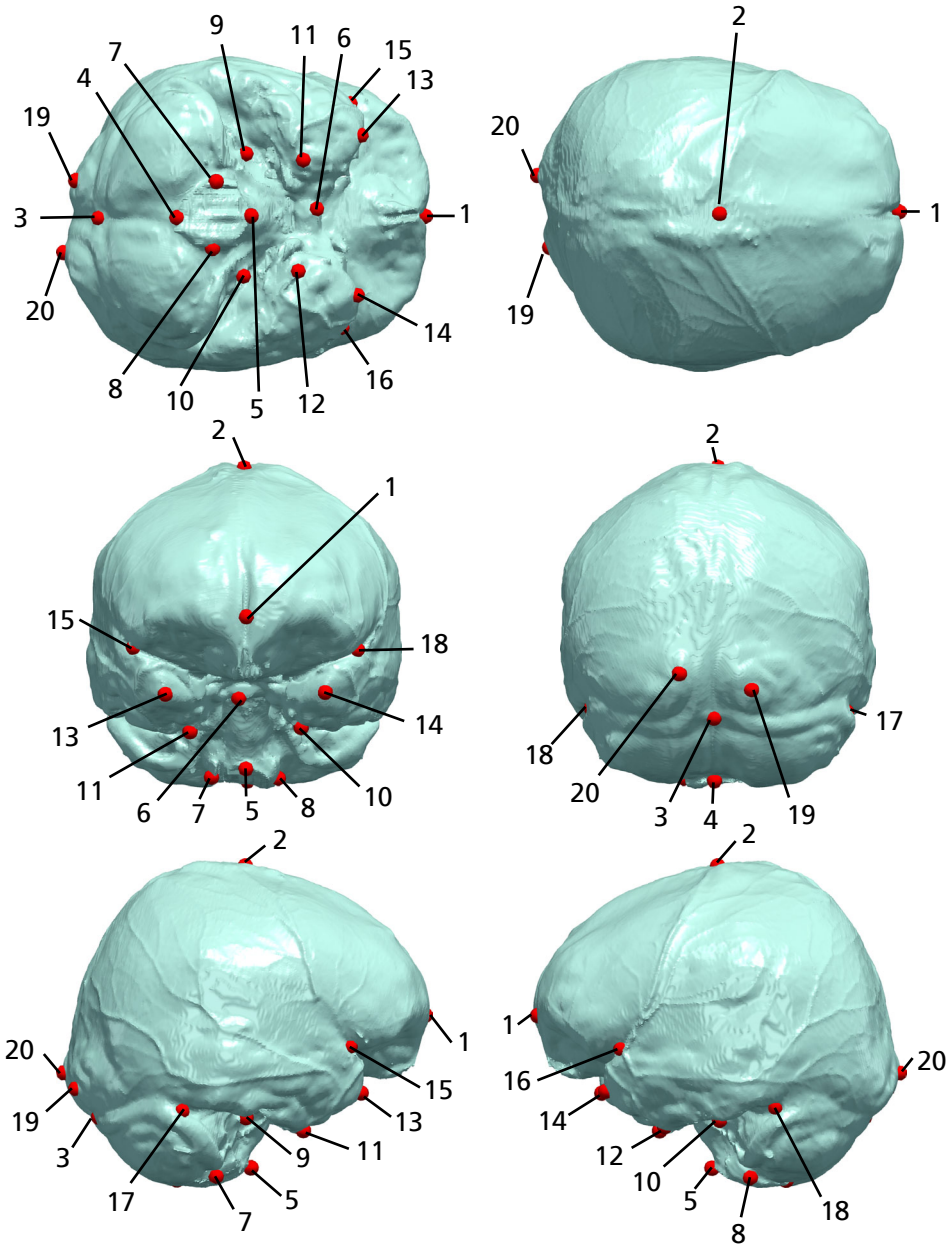

Figure 6.2: Endocranial landmarks. The surface is from a male human (H3).

6.1.3 Surface Parameterization and Sampling

The tool ReMESH (Attene and Falcidieno, 2006) was used to remove topological noise (i.e., remove handles and close holes to make sure the meshes are genus-0) and to simplify the surfaces to 50K vertices prior to parameterization. Figures 6.3**A**,**B** show the surface of a male human (H3) before and after simplification. The simplified surfaces were consistently parameterized on the sphere and deformed to match the spherical landmark consensus as described in chapter 3 (figures 6.3 **C**,**D**) and sampled using both the quasi-equidistant sampling scheme, resulting in semilandmarks, and an equiangular sampling grid (figures 6.3**E**,**F**).

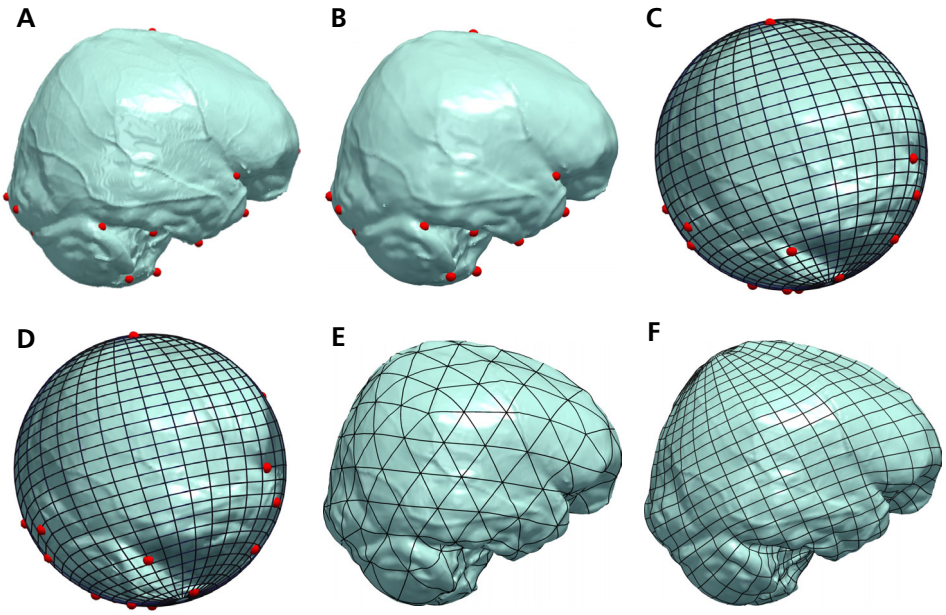

Figure 6.3: Surface simplification, parameterization and sampling. **A,B**: The surface of a male human (H3) after segmentation (**A**, 720K vertices) and after simplification to 50K vertices (**B**). **C,D**: Spherical conformal parameterization (**C**) and quasi-conformal (deformed) spherical parameterization (**D**). **E**: Quasi-equidistant sampling (semilandmarks). The reduced surface is sampled with a level 7 spherical icosahedron (164K vertices), overlaid with a subdivision level 2 wireframe. **F**: Equiangular sampling grid (for spherical harmonics transform). The reduced surface is sampled with a $B = 256$ grid (262K vertices), overlaid with a $B = 16$ wireframe.

6.2 Results

6.2.1 Case Study 1: Fourier Analysis to Measure Endocranial Shape Variability in Hominoids

Once the spherical harmonic coefficients $\mathbf{S}_i$ are calculated for every surface i, it is possible to analyze shape variation in the frequency domain. Figure 6.4**A** shows a human endocranium, low-pass filtered at various frequencies. It demonstrates that coefficients with low degree ℓ contain global large-scale shape components, while coefficients with higher degrees ℓ contain the fine details of the shape. Figure 6.4**B** shows the energy spectrum of the surface. The energy decreases rapidly with ascending degree.

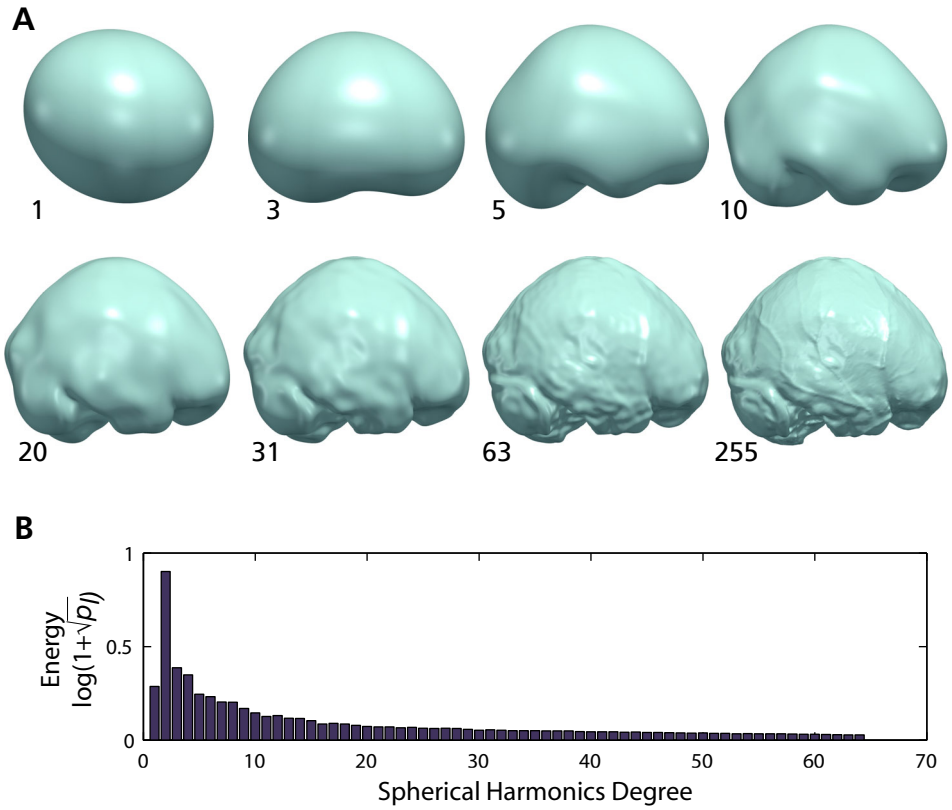

Figure 6.4: Fourier descriptor (SPHARM). **A**: Reconstructions of an endocast of a male human (H3) at various frequencies. The numbers indicate the maximum degree ℓ in the partial sum. More and more details show up as higher frequency components are added. **B**: The energy spectrum of the surface. The energy $\log(1 + \sqrt{p_\ell})$ (see equation 4.32) is plotted against the degree ℓ.

Validation: Biology versus Geometry

In order to validate the fitness of the SPHARM descriptor based on the homology-calibrated parameterization for shape analysis, three methods of shape quantification are going to be compared. These are:

1. Landmarks
2. SPHARM descriptor (based on the homology-calibrated parameterization)
3. Pure geometry

For all three methods, distance measures between the shapes can be defined. The Procrustes distance (see eq. 2.2) is commonly used to measure distances between landmark configurations and is therefore completely based on biology. Shape distances purely defined by geometry are the symmetric Hausdorff distance and the symmetric root-mean-square distances, respectively (see appendix B.2). Here, the symmetric root mean square (eq. B.5) was used, because it is analogous to the Fourier-based distance below.

The description based on the homology-calibrated parameterization is located in-between the biology-only and geometry-only approaches, in the sense that all geometric information is included in the analysis but biological knowledge is used to calibrate the parameter domain. The function to measure distance between two surface descriptions based on the homology-calibrated spherical parameterization depends on the used sampling scheme. For semilandmarks (i.e., Euclidean coordinates), the Procrustes distance between the semilandmark configurations can be calculated. Another option is the root-mean-squared distance (RMSD) between corresponding vertices. In contrast to the Procrustes distance, its magnitude is not dependent on the number of semilandmarks involved. The corresponding measure in the frequency domain is the RMSD defined in eq. 4.31. Numerical experiments proved the equivalence. Because in this section we concentrate on Fourier analysis, the RMSD calculated from the spherical harmonics coefficients is used to measure distance between two surface descriptions based on the homology-calibrated spherical parameterization.

Two landmark sets were investigated: the full set of all 20 landmarks listed in table 6.2 and a set of three landmarks in the midsagittal plane, consisting of landmarks $\{1,2,3\}$. The landmarks were used to GLS-align the surfaces prior to distance calculation. Thus, the distance measures for all three methods of shape quantification are affected by the choice of the landmarks. For both landmark configurations, three distance matrices were calculated, with the distance measures discussed above. The distance matrices were then used to construct dendrograms (figure 6.5). Matlab's *linkage* function with the *average* method, i.e., the average distance between all pairs of objects in two clusters, was used.

The results of using the full landmark set (figure 6.5, top row) indicate that all three distance definitions separate the humans from the great apes. Within the great apes, *Gorilla* are separated from *Pan*, with the exception of one *Pan troglodytes* specimen (T3), which is grouped together with the gorillas in the pure geometry case. An interpretation

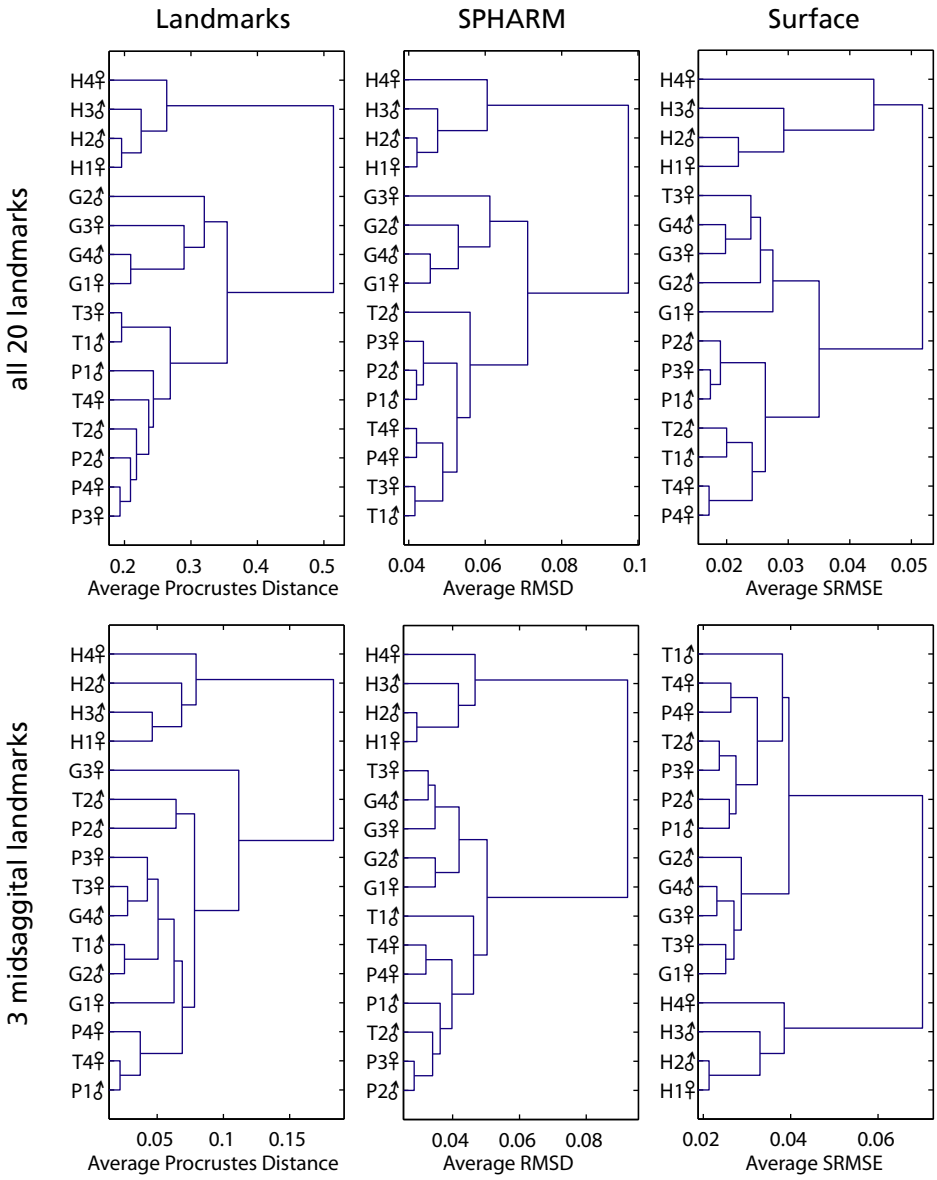

Figure 6.5: Dendrograms of various distance matrices of the endocranial sample. Left column: Procrustes distances of the landmark configurations; center: RMS distance (RMSD) of the spherical harmonics coefficients obtained from the homology-calibrated spherical parameterization; right column: symmetric RMS error (SRMSE) between the landmark-aligned surfaces. Top row: all 20 landmarks listed in table 6.2 were used; bottom row: only the 3 landmarks $\{1,2,3\}$ in the midsagittal plane were used.

of this observation is that the geometry without biological constraints can be insufficient to distinct between species. All three approaches are not capable to separate the two *Pan* species. Because description based on the homology-calibrated parameterization includes all biological and geometric information in the analysis, the quality of the corresponding clustering is comparable to the one based on biology only.

Using only three landmarks inverts the scenario. The dendrograms (figure 6.5, bottom row) still show the humans and the great apes in two separate groups. The Procrustes distance can not separate *Gorilla* from *Pan*. However, the geometry-based distance (with exception of T3) separate them. The three top clusters comprise the same specimens as in the above case with all landmarks. The description based on the homology-calibrated parameterization becomes inferior compared to the all-landmarks case in the sense that *Pan troglodytes* T3 is in the *Gorilla* group as well.

Note that for both landmark sets, the description based on the homology-calibrated parameterization performs as well as the better one of the descriptions based purely on biology and geometry, respectively.

This indicates that the approach to use both the biological and the geometric information available indeed delivers the best of both worlds. It scales well even to a very small number of landmarks. The results confirm the suitability of our parameterization for shape analysis. However, the true potential lies in the prospects for visualization as we shall see in the following sections.

To conclude this section, let us point out some questions which arise looking at the dendrograms in figure 6.5. One interesting point is the classification of T3 closer to the *Gorilla* than to the other *Pan* in the more geometry-based analyses. I did not see an obvious reason for that, and I think it would be an interesting starting point for an in-depth analysis. The same issue applies to the question why the two *Pan* species are not separated.

The Power of Fourier Analysis: Decomposing Patterns of Shape Variation

In order to further explore shape variation within the sample, we apply a PC analysis on the spherical harmonics coefficients $\mathbf{S}_i$. Figure 6.6**A** shows the result. PC1 explains 45.85% of the shape variability and separates humans from the great apes. Moving along PC1 shows the shape transformation which characterizes this separation. The pictures of "mean *Homo*" and "mean *Pan/Gorilla*" braincases suggest that the frontal lobe extends farther downward in humans than it does in other great apes, and that the mid-cranium is higher in humans. PC2 explains 20.44% of shape variability and sets apart *Pan* from *Gorilla*.

A PC is defined by an eigenvector in the high dimensional space of the data, i.e., the orthogonal space of the spherical harmonics. By projecting the eigenvectors associated with PC1/PC2 onto each subspace defined by a certain degree ℓ, the contribution of the coefficients of degree ℓ to the shape transformation along PC1/PC2 can be measured (see eq. 4.36). The corresponding spectra are shown in figure 6.6**B**. The energy spectrum for PC1 shows that coefficients of degree 2 account for most of the difference between hu-

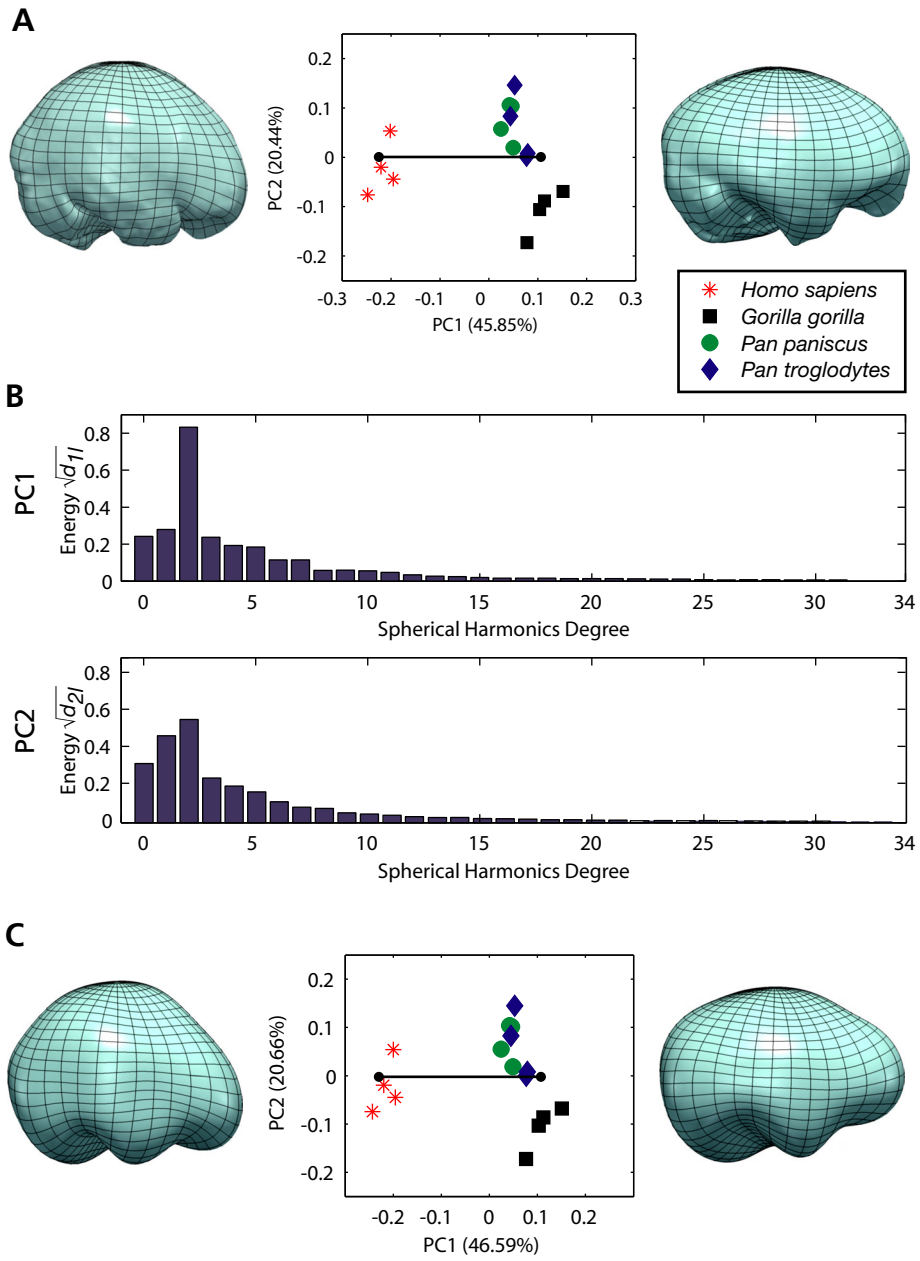

Figure 6.6: Shape variability in Hominoids. **A**: PC analysis of the spherical harmonics coefficients of the endocranial sample. Reconstructed surfaces for moving along PC1 (black horizontal line) are appended ("mean *Homo*" on the left and "mean *Pan/Gorilla*" on the right). **B**: Energy spectrum of eigenvectors associated with PC1 and PC2. Energy $\sqrt{d_\ell}$ (see equation 4.36) is plotted against the degree ℓ. Degree 2 contributes by far the most to PC1, and the main contributions for PC2 are in the first three sub-bands. For degrees higher than 7, respective contributions to PC1 are below 1%. **C**: PCA of low-pass filtered endocranial surfaces. Analogous to figure **A**, but only the coefficients of the lowest 8 degrees ($\ell \in [0, 7]$) are used for the analysis. Note the smoother surfaces.

man and great ape braincases. For PC2, degree 2 also accounts for most energy, but the difference to the first two degrees is smaller than for PC1. An interesting observation is that in both eigenvectors, a considerable amount of energy is contributed by the degree 0 subspace. Spherical harmonics of degree 0 describe translations. This means that the centroid of the landmark configurations, which was used for GLS alignment, is considerably different than the mass center of the surfaces. Note that this effect is not visible in the figure (the surface pictures are aligned).

The respective contributions of subspaces with degree higher than 7 are below 1% and therefore not significant for both distinctions. This interpretation is asserted by applying a PC analysis on only the coefficients of degree $\ell < 8$. The resulting graph, shown in figure 6.6**C**, is nearly identical to the one obtained from the PCA of the full frequency range. The reconstructed "mean *Homo*" and "mean *Pan/Gorilla*" surfaces are smoother than the ones in fig. 6.6**A**, because coefficients with $\ell > 7$ are ignored (i.e., set to zero), but still visualize well the shape difference.

It is also possible to visualize shape variability corresponding to specific degrees of spherical harmonics. The marked peak in the energy spectrum for PC1 (and to a smaller extent in PC2) at degree $\ell = 2$ (figure 6.6**B**) raises the question how shape variability in only that subspace appears. Figure 6.7**A** graphs the PCA on the $\ell = 2$ subspace (which consist of only 15 real-valued coefficients). The plot looks very similar to the one obtained from the PCA on the full frequency range, and the reconstructed surfaces are ellipsoid-like, because coefficients with $\ell > 2$ were ignored and coefficients with $\ell = 1$ were set to their sample-average (i.e., the "average first-order ellipsoid") in order to obtain a meaningful surface. One difference in the PCA plot is the reduced separation between Pan and Gorilla along PC2. This is because coefficients of degree 2 contribute less to PC2 than they contribute to PC1 (i.e., the peak in the spectrum at $\ell = 2$ is higher for PC1 than for PC2).

This is supported by looking at the shape variability contained in only the first two frequency bands (figure 6.7**B**). Here, PC1 separates *Gorilla* from *Homo* and *Pan*, and PC2 separates *Homo* from *Pan*, i.,e., the patterns described by PC1 and PC2 are swapped. This makes sense because the energies in the first two bands are higher for PC2 than for PC1 (in the PCA on the full spectrum). The corresponding first-order ellipsoids are more sphere-like for *Homo/Pan* than for *Gorilla*.

In this section, it was demonstrated how the Fourier description can be used to decompose patterns of shape variation detected by PCA. It was shown that higher frequencies are not significant for separating the endocranial surfaces of Homo, Pan and Gorilla, and the basic differences in shape were presented.

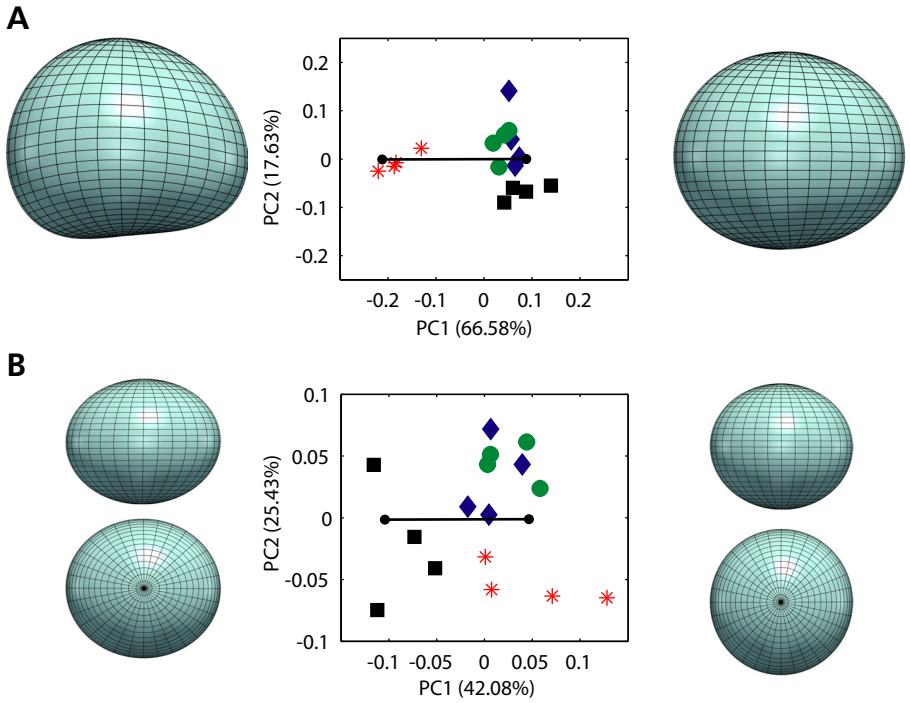

Figure 6.7: Decomposition of principal components. **A**: PCA on the band-pass filtered endocranial surfaces. Only the 15 coefficients of degree $\ell = 2$ are used for the analysis. For the reconstructed "mean *Homo*" and "mean *Pan/Gorilla*" surfaces shown on the left and on the right, respectively, the average coefficients of the $\ell = 1$ band ("mean first-order ellipsoid" are added to obtain a meaningful surface. **B**: PCA on the first two frequency bands. The patterns described by PC1 and PC2 are swapped. "Mean *Gorilla*" and "mean *Homo/Pan*" first-order ellipsoids are shown on the left and on the right of the PCA plot, respectively.

6.2.2 Case Study 2: Patterns of Endocranial Asymmetry in Hominoids

Human brains have structural and functional asymmetries. Often, structural asymmetries can be mapped to functional ones. For instance, Geschwind and Levitsky (1968) discovered a structural asymmetry which could be mapped to a long-known functional asymmetry, a left-hemisphere specialization for language (Broca, 1861). Other well-known asymmetries are the so-called frontal and occipital "petalia", i.e., the extension of the frontal lobe, typically of the right hemisphere, and the occipital lobe typically of the left hemisphere (Lemay, 1977; Chui and Damasio, 1980; Falk et al., 1991; Watkins et al., 2001). Pilcher et al. (2001) reviewed work on non-human primate brains and compared the brains of New and Old World monkeys. They found that the same right side frontal and left side occipital pattern of asymmetry known from humans is also present in the brains of great apes. The study of such asymmetries, notably when they appear during evolution and development, is important for paleoanthropology.

In this section we demonstrate how semilandmarks obtained from the homology-calibrated spherical parameterization can be used to detect patterns of asymmetry in the hominoid endocranial sample. This is done by studying at shape variability in a sample combining the original endocranial surfaces with their mirror images. The mirror images are constructed as follows:

1. Each original surface (including its landmarks) is scaled by a factor of -1.0 along the y axis, followed by inversion of the face normals.

2. All bilateral landmarks are relabeled to their opposite side.

Conformal maps to the sphere were calculated for all 32 surfaces, and all 20 landmarks (see table 6.2) were used to calibrate the spherical parameterizations. The quasi-equally spaced sampling-scheme was used to obtain semilandmarks of subdivision levels 7 (i.e., 164K semilandmarks). In order to minimize positional differences, the surfaces were GLS aligned using all semilandmarks. A PC analysis was then applied on the semilandmarks, and the PCs scanned for patterns separating the mirrored from the original surfaces.

The first few PCs of the PCA give a very similar result to the one presented in section 6.2.1 (i.e., PC1 separates *Homo* from great apes), and the mirrored samples lie at positions identical to their originals. The first PC to separate the original specimens from their mirror image is PC8 (fig. 6.8). The visualization techniques described in section 4.2.2 can be used to visualize the associated shape transformation relative to the (symmetric) consensus shape (i.e., the origin in PC space). The right hemisphere has a larger superior, lateral and occipital surface area, while the left hemisphere has a larger inferior and frontal surface area. The pattern revealed by direction and magnitude of the shape transformation describes expansion normal to the surface in the parietal and occipital area as well as in most inferior areas of the left hemisphere. The right hemisphere has a larger normal expansion in the infero-lateral, infero-lateral frontal and the mid-occipital areas. Note that the patterns described by the surface area and normal expansion are quite different, most notably laterally and inferiorally. The shape transformation tangential to the surface,

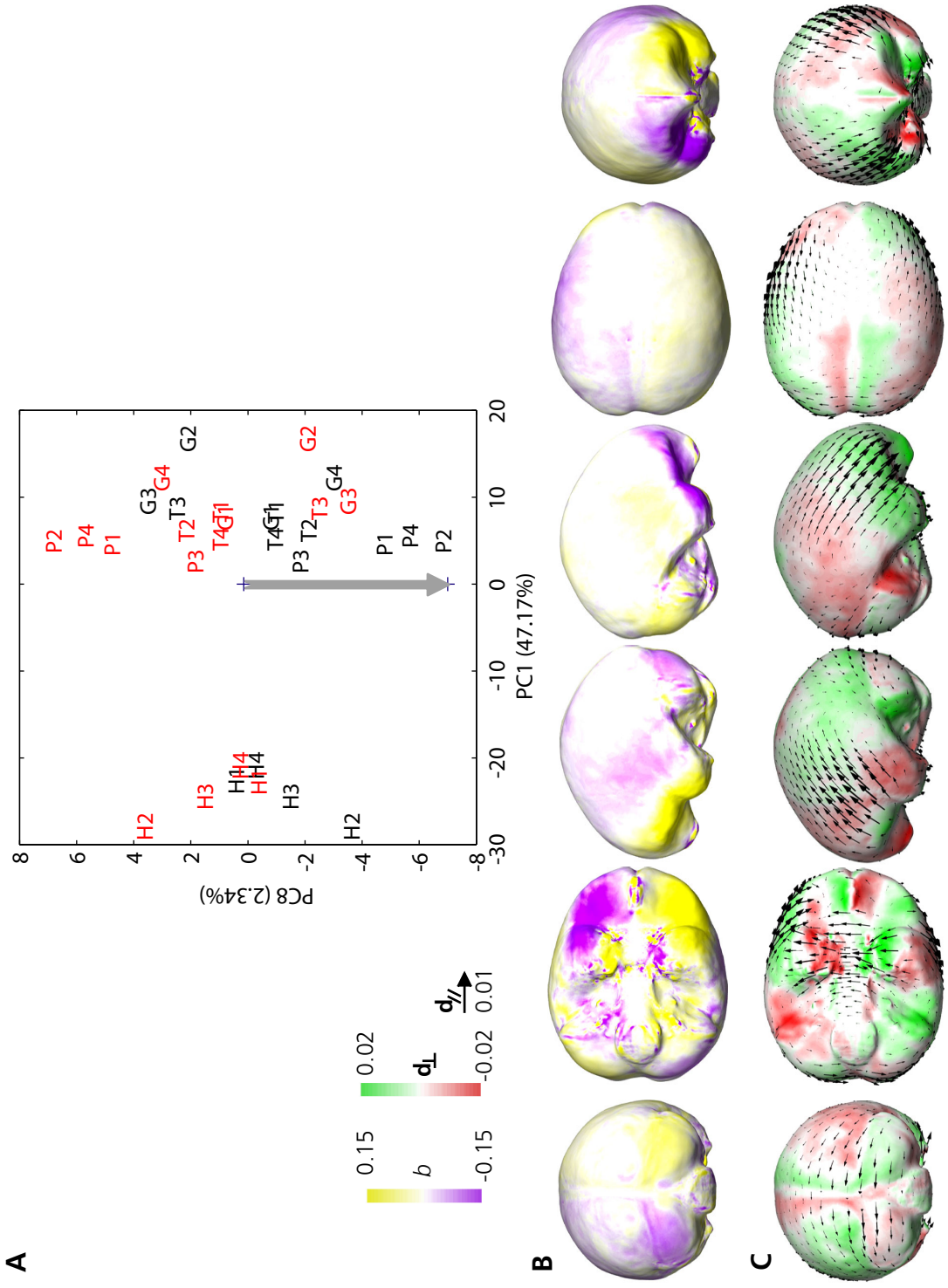

Figure 6.8: Pattern of asymmetry along PC8. **A**: PC analysis. PC8 is plotted against PC1. Original specimens are black and their mirror images are red. **B**: Relative surface area growth along the arrow in the PCA plot (from the origin to PC8=-7). Colors indicate the shape transformation necessary to reach the target shape. **C**: Movement normal (green/red) and tangential (arrows) to the surface. Volume-normalized space units are used. Arrows $\mathbf{d}_{\parallel}$ are scaled by factor 5 for better visibility.

shown by the arrows in figure 6.8**C**, indicates movement towards the infero-frontal area on the right and the left parietal area. It is strongest laterally and reminds one of the petalia pattern. A strong left-right fluctuation exists on the bottom. Three of the four humans and nine of the twelve great apes specimens in the sample show this pattern. The other specimens show the inverse pattern.

The next PC which shows a pattern of asymmetry is PC10 (see figure 6.9). Nine of the twelve great apes show this pattern, but it is only present in one of the four humans (two show the inverse pattern). The visualization reveals a rightward frontal and leftward occipital pattern of asymmetry which again reminds of the petalia pattern. Interestingly, the coronal sutures are visible and they delimit outward from inward movement. Note the shape transformation tangential to the surface: in the superior area, it describes an anti-clockwise rotation, and a clockwise rotation on both sides. The left parietal area is a source and the right parietal area a sink of movement.

PC12 reveals another pattern of asymmetry (figure 6.10). Eight great apes, but only one human share this structure. The relative surface area asymmetry looks similar to the one associated with PC10, but the the movement normal to the surface is inverted. Again, the coronal sutures are visible, and here, they also denote a border between relative surface area growth and shrinkage.

Principal components higher than PC13 explain less than 1% of the variance in the sample and are not discussed here. Note that PC8 seems to describe *size* difference patterns between the two hemispheres, while PCs 10 and 12 describe *shape* difference patterns between the left and the right hemispheres.

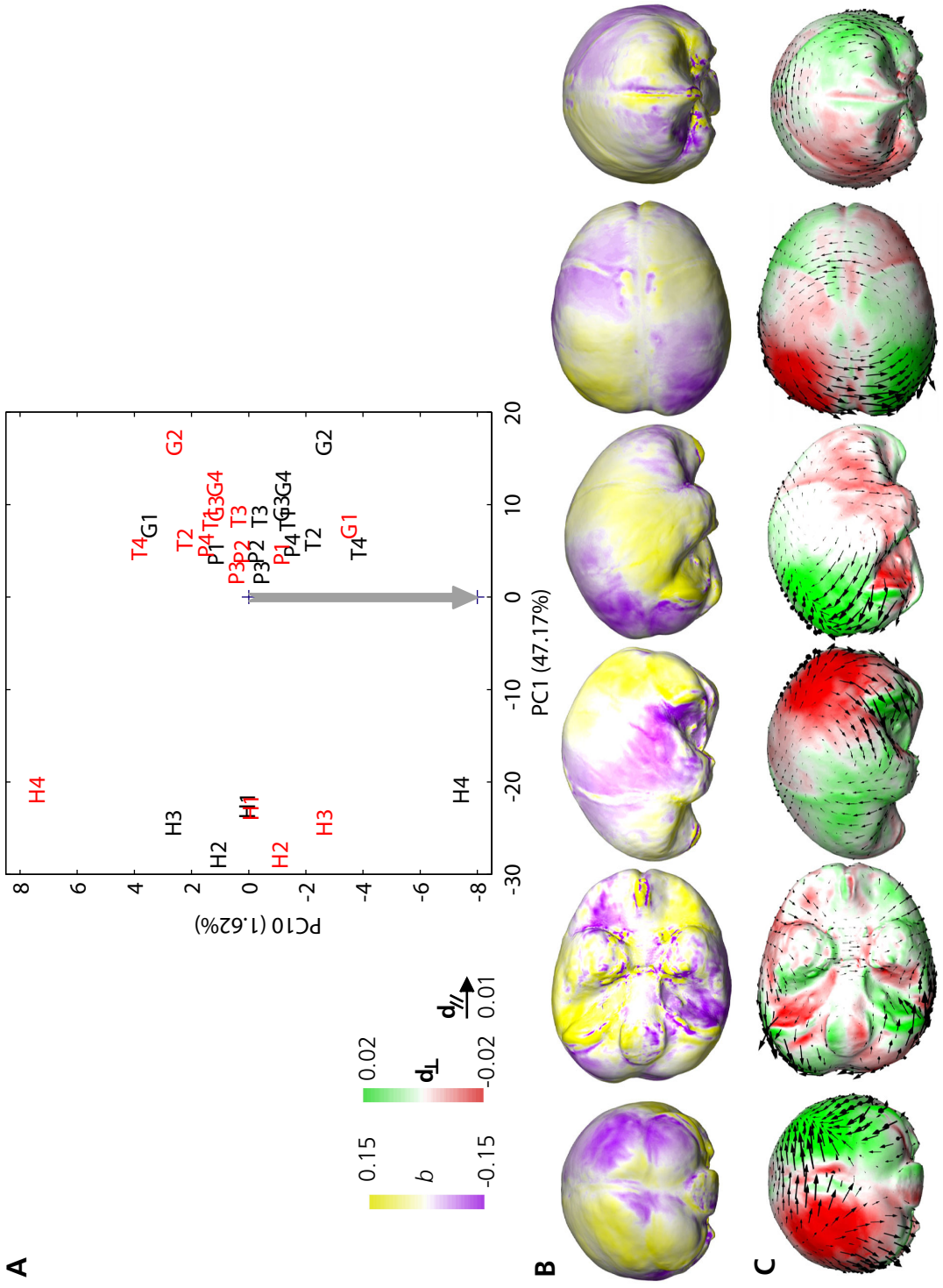

Figure 6.9: Pattern of asymmetry along PC10. **A**: PC analysis. PC10 is plotted against PC1. Original specimens are black and their mirror images are red. **B**: Relative surface area growth along the arrow in the PCA plot (from the origin to PC10=-8). Colors indicate the shape transformation necessary to reach the target shape. **C**: Movement normal (green/red) and tangential (arrows) to the surface. Volume-normalized space units are used. Arrows $\mathbf{d}_{\shortparallel}$ are scaled by factor 5 for better visibility. Note the visibility of the coronal suture.

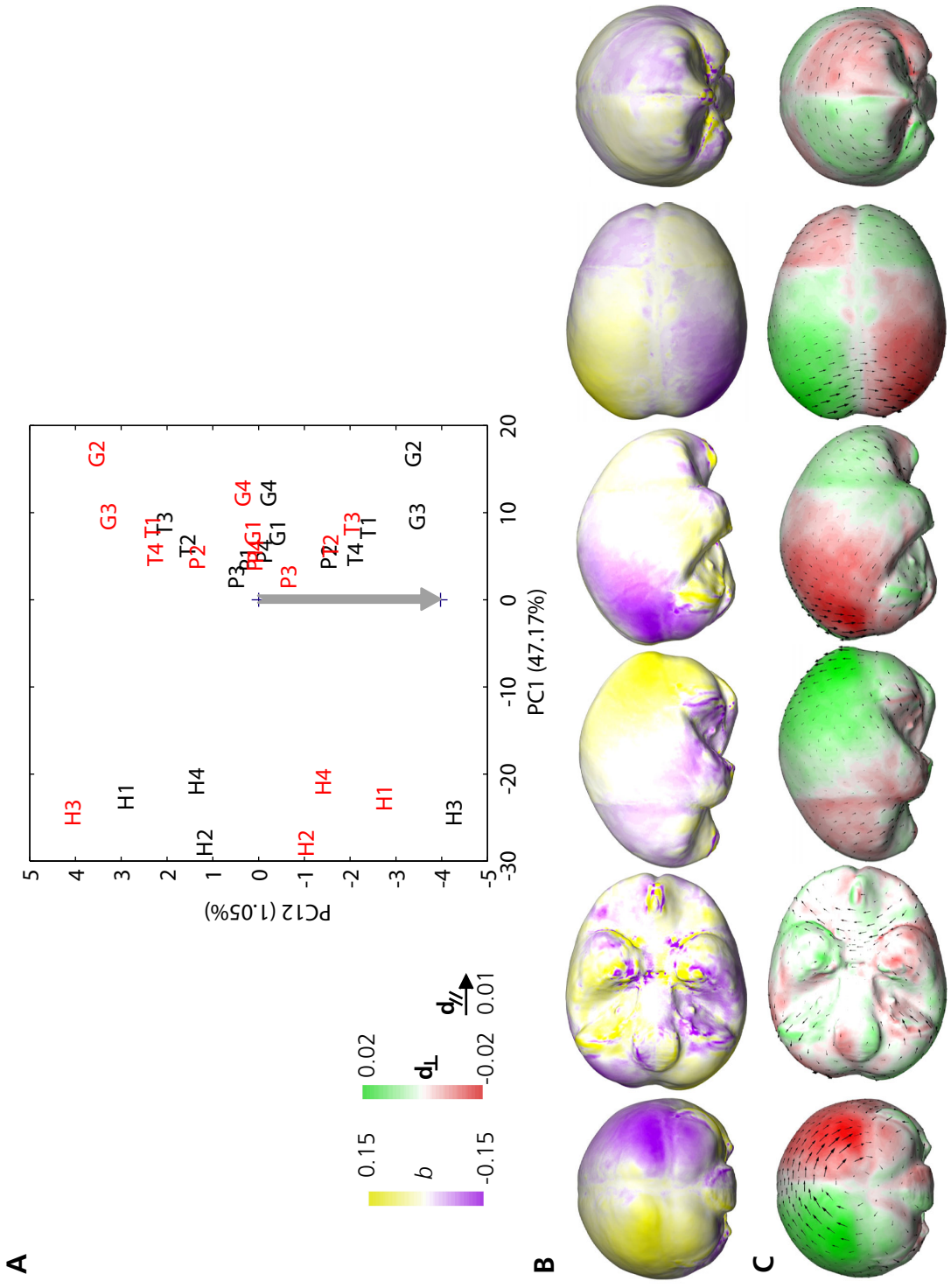

Figure 6.10: Pattern of asymmetry along PC12. **A**: PC analysis. PC12 is plotted against PC1. Original specimens are black and their mirror images are red. **B**: Relative surface area growth along the arrow in the PCA plot (from the origin to PC8=-4). Colors indicate the shape transformation necessary to reach the target shape. **C**: Movement normal (green/red) and tangential (arrows) to the surface. Volume-normalized space units are used. Arrows $\mathbf{d}_{\shortparallel}$ are scaled by factor 5 for better visibility. Note the visibility of the coronal suture.

6.2.3 Case Study 3: Visualizing Shape Transformation between Chimpanzee and Human Braincases

Let us look more closely at how human braincases are different from the ones of our closest living relatives, the chimpanzees (*Pan troglodytes*). For this study, the landmarkset L_7 with seven landmarks at clearly recognizable locations was used. The landmarks were used to GLS-align the size-normalized surfaces of *Homo* and *Pan troglodytes* and compute the quasi-consistent homology-calibrated spherical parameterization prior to sampling. The parameterizations were sampled with a level 7 spherical icosahedron (see section 3.1.3) resulting in 164K consistent vertices (semilandmarks).

Since all vertices are consistent, PCA can be used to measure the shape variance in the sample set. The first PC, which comprises 82.13% of the total shape variation, distinguishes human from chimpanzee endocasts (see figure 6.11). In the following, we visualize the transformation from the mean chimpanzee to the mean human.

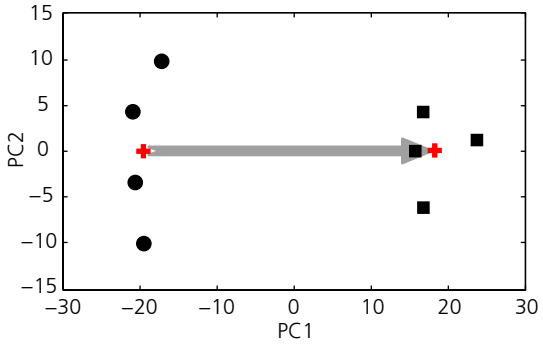

Figure 6.11: Principal Component Analysis of the consistent remesh (163'842 semilandmarks). Squares: humans; Circles: chimpanzees; the red crosses and the arrow indicate the shape transformation along PC1 from the mean chimpanzee to the mean human. PC1 comprises 82.13% of the total shape variation.

First, the performance of the new method for morphing a chimpanzee endocast into a human endocast is compared to classical TPS-based morphing (figure 6.12). The figure clearly shows the advantage of our method for such landmark-depleted forms: The thin-plate spline, defined purely by the landmarks, deforms the mean chimpanzee surface such that the landmarks match the ones of the mean human. Since no landmarks are defined on the lateral parts, the TPS grossly misses the target surface in these areas (bottom row). Clear differences can also be observed in the superior part of the parietal areas and the frontal bec. Our method, in contrast, defines corresponding points everywhere on the actual surfaces, which results in a much more natural shape blending. This shape transformation is visualized using the techniques described in section 4.2.2 and shown in

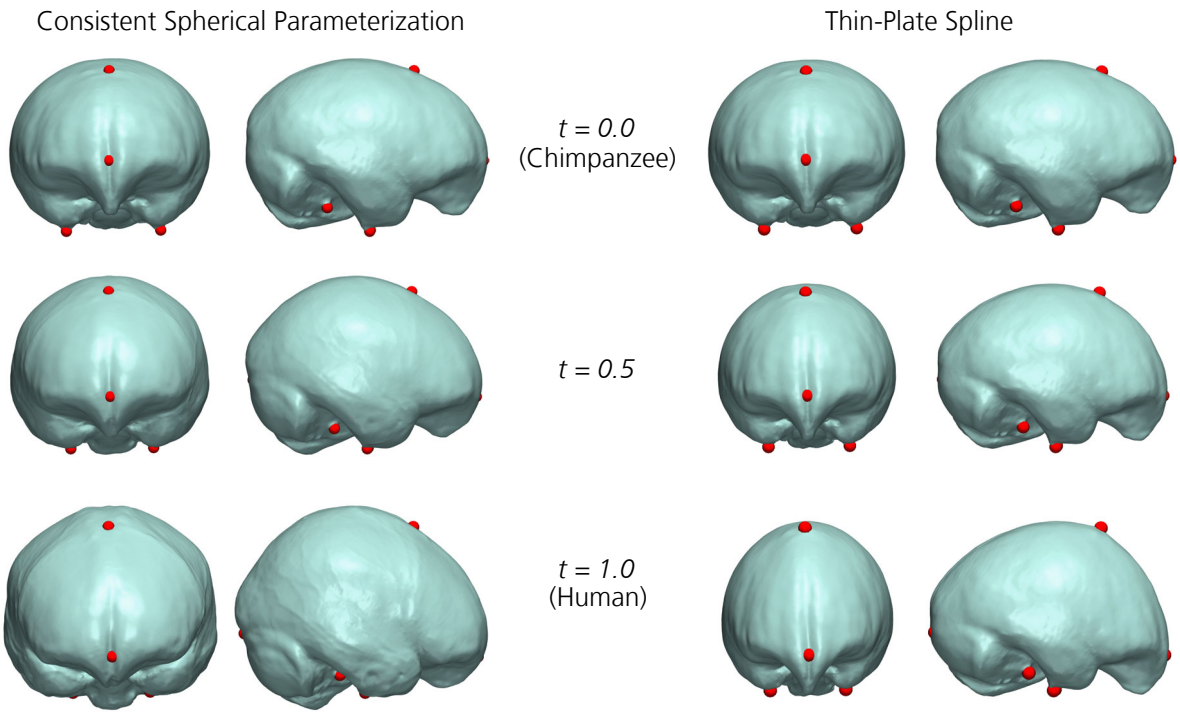

Figure 6.12: Morphing from the mean chimpanzee (top row) to the mean human (bottom row). Consistent Spherical parameterization (left), which defines corresponding points everywhere on the surfaces, is compared to thin-plate splines (right) which are defined by the seven landmarks only.

figure 6.13. The surface of the frontal, superior and occipital areas and the cerebellum and the temporal lobes is expanded and the inferior and lateral areas contracted. There is a strong outwards movement normal to the surface in the parietal, occipital and most inferior areas, while the frontal and lateral areas move inwards. Movement tangential to the surface indicate a current from the superior frontal area towards sella (i.e., landmark 6 in table 6.2; however, landmark 6 was *not* used in this analysis). Note the descent of the frontal area, thus narrowing of the cranial base angle, in the human endocast relative to the chimpanzee endocast (best visible in fig. 6.13**C**).

The pictures show that the spherical conformal parameterization, constrained with biological information, is well suited to measure and visualize shape transformation of biological surfaces. Only a few landmarks are used but the patterns revealed are relatively complex and are clearly driven by geometric features of the endocranial surface between the landmarks.

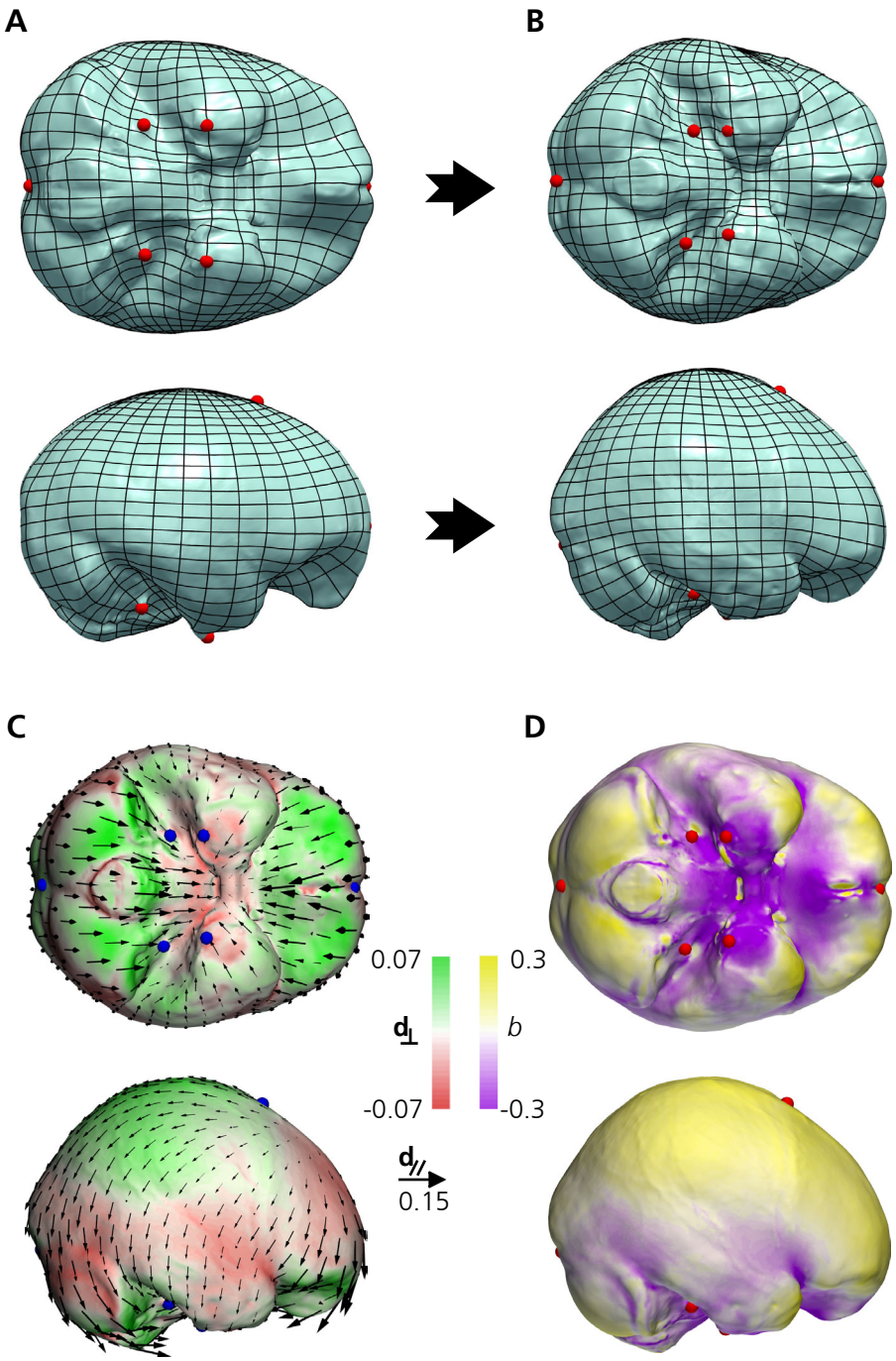

Figure 6.13: Visualizing shape transformation from chimpanzee to human braincase. **A**: the source surface (mean chimpanzee braincase); **B**: the target surface (mean human braincase) (both are overlaid with consistent spherical coordinate grids). **C**, **D**: false-color map representation of the same transformation as in **A**, **B**. Graphs show mean human braincase, red/green indicate the direction (inward/outward) and magnitude of shape transformation perpendicular to the surface; arrows indicate shape change parallel to the surface. Yellow/purple indicate relative area expansion/contraction that was necessary to attain human shape.

Chapter 7

Conclusion and Future Work

This thesis proposed a new method for quantitative analysis of genus-0 surfaces such as the braincase. Free-form surfaces in the form of triangle meshes were transformed into a comparable numerical representation in the spherical domain, which is defined by the geometry of the whole endocranial surface, plus manually annotated biological information in the form of homologous landmarks. This parameterization permits analysis, comparison and visualization of entire endocranial surfaces in either Euclidean or Fourier space.

The proposed approach combines geometric morphometrics and computer graphics. Due to its multi-disciplinary nature, this chapter is split into two sections. First, the method developed in this thesis is recapitulated and discussed from a technical point of view, and possible future work is suggested. Second, the gains of the new methods for endocast analysis are discussed from a biological point of view using the three case studies presented in chapter 6 (see also Specht et al., 2007). Finally, potential starting points for further studies are given.

7.1 Technical Discussion

By combining conformal (i.e., angle-preserving) spherical mesh parameterization with smooth energy-minimizing deformations on the sphere, a method to compute homology-calibrated, quasi-consistent bijective and piecewise linear spherical parameterizations for a set of triangle meshes was presented. In other words, a method to calculate consistent spherical parameterizations, with anatomical landmarks being the feature points, was developed. Compared to previous methods of consistent spherical mesh parameterization, the main contribution of this work is the uniqueness of the parameterizations. Therefore, a position on the sphere is mapped to a well-defined, corresponding point on every surface. A thorough review of mesh parameterization theory was the key to this result, and an empirical verification comparing the stretch-minimizing spherical parameterization with the global conformal parameterization confirmed the expectations, which were (1) the conformal parameterization is more precise and (2) the stretch-minimizing parameterization is more accurate.

The homology-calibrated parameterization was then exploited to define novel geometric morphometric methods. A new approach to define semilandmarks on a genus-0 surface was presented. The advantage compared to previous methods lies in the utilization of a well-defined parameter domain, i.e., the unit sphere, rather than ad-hoc criteria to place the semilandmarks.

The spherical parameter domain permits quantification of the surfaces by a Fourier series based on the spherical harmonic transform, therefore introducing Fourier analysis of surfaces to geometric morphometrics. In contrast to previous approaches from computer vision and medical imaging, the new method uses homology information in the form of landmarks to increase the biological significance of the description. Fourier analysis of surfaces has been an open problem in geometric morphometrics. This work closes this gap by complementing the geometric morphometric toolbox with tools for spherical Fourier analysis.

Semilandmarks resulting from consistent mesh parameterization and Fourier descriptors are just different numerical representations for the same data set. Semilandmarks permit localization (and therefore editing) in Euclidean space, while Fourier descriptors permit application of filter operations such as low-pass, band-pass etc. The choice of representation depends on the underlying hypothesis (a biological hypothesis can be formulated in either one of the spaces). Further applications of Fourier series are information reduction, i.e., cutting the series at a given frequency, thus ignoring high-frequency detail, and only keeping the low-frequency harmonics. Another application is progressive shape transmission: global large-scale features of the shape are delivered first, followed by finer and finer details of the shape.

Because the parameterizations are consistent, it is straight-forward to apply established methods to visualize shape deformation. Further, because the sphere is a well-defined domain, and because the parameterizations are quasi-conformal, orthogonal spherical coordinate grids can be projected onto the surfaces. The resulting 3D visualizations of shape deformation are a novel approach to extend 2D deformation grids (Thompson, 1917; Bookstein, 1989a) to 3D.

The theory was implemented in two parts. The mesh parameterization and sampling parts were implemented in C++, and the statistical analysis and visualization parts were incorporated in the MorphoTools framework, written in C++ and Java.

7.1.1 Limitations

The price paid for the well-defined spherical parameter domain is the limitation to genus-0 surfaces, i.e., surfaces without holes, which can be transformed into a sphere without self-intersection. Many biological forms are of higher topological complexity and are difficult to be approximated with a genus-0 surface. Another limitation is the restriction to data without extreme extrusions (such as the braincase), because the area distortion in the conformal map might become unacceptable. Jin et al. (2004) suggested topological modification for such cases.

The algorithm used to compute the conformal maps is not guaranteed to find a bijective mapping if the input mesh contains obtuse angles. Fortunately, most meshes encountered in our application consist of mostly "well-shaped" triangles (with all three angles being acute, i.e., all three angles $< \frac{\pi}{2}$). Recently, an algorithm to approximate an input mesh with a guaranteed nonobtuse mesh has been proposed (Li and Zhang, 2006).

7.1.2 Future Work

It would be interesting to investigate how geometry images, i.e., rectangular mappings of the spherical parameterizations (Gu et al., 2002; Praun and Hoppe, 2003), could be used for geometric morphometric purposes. Mapping the surface to a planar domain permits application of imaging techniques such as the 2D Fourier transform. However, angular and area distortion might become a serious issue.

A promising extension would be to exploit the spherical parameterization for interactive region-of-interest selection. Areas of interest could be marked on the "globe", and different areas could be weighted differently for the proceeding analyses, thus providing for spatial filtering.

7.2 Biological Discussion

The new method was applied to quantify the surfaces of the braincase of great apes (chimpanzees, bonobos and gorillas) and humans. To my knowledge, this is the first fully quantitative approach to compare complete endocranial surfaces. Thus, this is a new methodology that can be considered fundamental for paleontological research, since it permits biologists to assess and compare the shape of the braincase in quantitative terms, and to explore patterns of shape difference in an interactive way.

In case study 1, the usefulness of the 3D Fourier descriptor based on the homology-calibrated parameterization for shape analysis was validated. A set of cluster analyses based on different shape distance measures confirmed the biological significance of the 3D Fourier descriptor even for small sets of landmarks, and showed that it increases with the addition of more landmarks. The specimens were grouped according to their genus (i.e., *Homo*, *Pan* and *Gorilla*). However, the two *Pan* species were not separated.

Measuring shape variability with a PCA led to a similar result. PC1 separates *Homo* from the great apes, and PC2 separates *Pan* from *Gorilla*. It was shown that these separations are driven by the lower frequency components (i.e., the global large-scale components) of the shapes. The patterns of distinction were further decomposed, showing that lowest frequency components are more significant for separation of *Gorilla* from *Homo/Pan*, and slightly higher frequency components are more significant to separate *Homo* from the great apes. Reconstructed surfaces were presented at all stages of the analyses to provide visual feedback. Overall, this case study proved the suitability and power of the 3D Fourier descriptor based on the homology-calibrated, quasi-consistent spherical parameterization for geometric morphometric analysis. This is especially true for visualization of results.

Case study 2 tested the suitability of the homology-calibrated parameterization for detection of patterns of asymmetry in the endocranial surface. The sample was augmented with the mirror images of all specimens. Semilandmarks were computed and analyzed with PCA. A set of PCs separating original from mirrored specimens was found. Three of them explain more than 1% of shape variability in the sample. These patterns were analyzed by visualizing the corresponding relative change of surface area and the magnitude and direction of the deformation fields. While some of the detected patterns of asymmetry resembled the frontal and occipital "petalia" asymmetries, their biological meaning need further clarification. However, an interesting aspect of this analysis is the fact that left-/right *size* difference patterns are separated form left/right *shape* difference patterns. The ability to assess patterns of symmetry in endocranial surfaces has a potential for paleoanthropological studies. Previously, such analyses were very limited because no adequate quantification of the surface was available.

The shape transformation between chimpanzee and human braincases was looked at in detail in case study 3. Morphing the mean chimpanzee to the mean human endocast using semilandmarks (i.e., consistent remeshes) was compared to morphing using TPS. Because only K=7 landmarks were used (due to the difficulty to precisely set landmarks on the endocranial surface), the new method yielded a better result than the TPS. Finally, visualizing shape differences by drawing an orthogonal deformation grid on the surfaces was visually compared to relative surface area and deformation-field based color/coding and glyph annotation. Both visualizations indicate expansion of the parietal-superior area, the cerebellum and the temporal lobes and descent of the frontal area, thus narrowing of the cranial base angle, in the human endocast relative to the chimpanzee endocast.

7.2.1 Future Work

This thesis focused on development and implementation of new methods for the quantitative comparative analysis of endocranial shape variability. The applications of these methods to a small sample of hominoid endocasts represent just a first step. They demonstrate that the proposed methods are well suited to detect differences between endocranial shapes at global scale as well as at local scales. The obvious next step is the analysis of larger samples with the new methods. Using more specimens will permit to obtain results with high statistical significance. The analyses described above are good starting points for building and testing future biological hypotheses.

The optimal landmark set for analysis of the endocranial surface needs further investigation. It is clear that the significance of the results increases with the amount of biological information included in the analysis. However, because many endocranial landmarks are difficult to locate, the effects of landmark placement errors and of the choice of landmarks needs to be analyzed in further detail. Here, the proposed iterative workflow of sampling, analysis, visualization of results and hypothesis refinement can be expected to yield new insights into the biological validity of endocranial landmarks.

A topic of particular interest will be to explore a large set of *Pan troglodytes* and *Pan paniscus* specimens. This will permit answering questions as to whether intraspecific shape variability is smaller than interspecific shape variability between these two sister taxa. These insights can then be used to study fossil data.

Finally, the new methods could also be applied to quantify other biological forms of spherical topology, notably when landmarks are scarce. Examples are isolated bones (e.g., the clavicle), conodonts, pollens etc. More complex structures, like the entire skull, could be approximated by a closed genus-0 mesh ("rubber wrap"), on which the methods could be applied as well.

Appendix A

Spherical Harmonics

This appendix provides technical details of the spherical harmonics functions, the spherical harmonics transform, and how surfaces described by a set of spherical harmonics coefficients can be aligned using the first-order ellipsoid.

A.1 Spherical Harmonic Transform

Similar to the Fourier transform for Euclidean spaces, there exists the spherical harmonic transform (SHT) for signals on the spherical domain. Therefore, the SHT is also called the *Fourier transform on the sphere*. The SHT expands a spherical signal $f(\theta, \phi)$ into a generalized Fourier series using the spherical harmonics basis functions Y_ℓ^m. For any non-negative integer ℓ and integer m, $|m| \leq \ell$, the spherical harmonic Y_ℓ^m is a harmonic homogeneous polynomial of degree ℓ. Using spherical polar coordinates $\theta \in [0, \pi]$ and $\phi \in [0, 2\pi[$ (see figure 3.4 and section 3.1.3), the spherical harmonics are defined as (Vilenkin, 1968; Arfken, 1985; Brechbühler, 1995)

$$Y_\ell^m(\theta, \phi) = \sqrt{\frac{2\ell+1}{4\pi}\frac{(\ell-m)!}{(\ell+m)!}} P_\ell^m(cos\theta) e^{im\phi} \tag{A.1}$$

$$Y_\ell^{-m}(\theta, \phi) = (-1)^m Y_\ell^{m*}(\theta, \phi) \tag{A.2}$$

where Y_ℓ^{m*} is the complex conjugate of Y_ℓ^m and P_ℓ^m is the associated Legendre polynomial

$$P_\ell^m(w) = \frac{(-1)^m}{2^\ell \ell!}(1-w^2)^{\frac{m}{2}} \frac{d^{m+\ell}}{dw^{m+\ell}}(w^2-1)^\ell. \tag{A.3}$$

The first few spherical harmonics are plotted in figure A.1.

Let S^2 denote the surface of the unit sphere. The Y_ℓ^m construct an orthonormal basis of the Hilbert Space $L^2(S^2)$ of square integrable functions on S^2, with the inner product

$$< f, g >= \int_0^\pi \left[\int_0^{2\pi} f(\theta, \phi) \cdot g^*(\theta, \phi) d\phi \right] \sin\theta d\theta. \tag{A.4}$$

					c_0^0					
				c_1^{-1}	c_1^0	c_1^1				
			c_2^{-2}	c_2^{-1}	c_2^0	c_2^1	c_2^2			
		c_3^{-3}	c_3^{-2}	c_3^{-1}	c_3^0	c_3^1	c_3^2	c_3^3		
	...	...	...	...	...	...	...	...	...	
c_{B-1}^{-B+1}	...	...	...	...	c_{B-1}^0	...	...	...	...	c_{B-1}^{B-1}

Table A.1: Pyramid structure of spherical harmonics.

The harmonics of degree ℓ span a subspace of $L^2(S^2)$ of dimension $2\ell + 1$, which is invariant under the rotations of the sphere.

Let $f \in L^2(S^2)$ be a spherical function. The expansion of f in terms of spherical harmonics can be written as

$$f(\theta, \phi) = \sum_{\ell \geq 0} \sum_{|m| \leq \ell} c_\ell^m Y_\ell^m(\theta, \phi) \tag{A.5}$$

where the complex coefficients c_ℓ^m denote the *Fourier coefficients*, and

$$c_\ell^m =< f, Y_\ell^m >= \int_0^\pi \int_0^{2\pi} f(\theta, \phi) Y_\ell^m(\theta, \phi) d\phi \sin\theta d\theta. \tag{A.6}$$

We call $f \in L^2(S^2)$ *band-limited* with *bandwidth* $B \geq 0$ if $c_\ell^m = 0 \; \forall \ell \geq B$. Healy et al. (2003) show that the equiangular grid, defined as $\theta_j = \frac{\pi(2j+1)}{4B}, \phi_k = \frac{2\pi k}{2B}$, constitutes a sampling pattern which is adequate to sample f (see also section 3.1.3). With this sampling patterns, the discretized version of equation A.6 is

$$c_\ell^m = \frac{\sqrt{2\pi}}{2B} \sum_{j=0}^{2B-1} \sum_{k=0}^{2B-1} f(\theta_j, \phi_k) Y(\theta_j, \phi_k). \tag{A.7}$$

Therefore, a function f with bandwidth B is defined by the B^2 complex coefficients of its spherical harmonic expansion. The coefficients form a pyramid, see table A.1.

Likewise, a set of complex coefficients c_ℓ^m can be transformed into a set of sample values by the *inverse SHT* (SHT^{-1}):

$$f(\theta_j, \phi_k) = \sum_{\ell=0}^{B-1} \sum_{|m| \leq \ell} c_\ell^m Y_\ell^m(\theta_j, \phi_k). \tag{A.8}$$

Efficient implementations with a complexity of only $O(B^2 log^2 B)$, instead of $O(B^4)$ suggested by (A.7), exist for both the SHT and the inverse (Healy et al., 2003).

In the above, a spherical scalar signal $f(\theta, \phi)$ was considered. A high dimensional signal (such as a surface in 3D) can be handled by independently processing each of its components as a scalar signal.

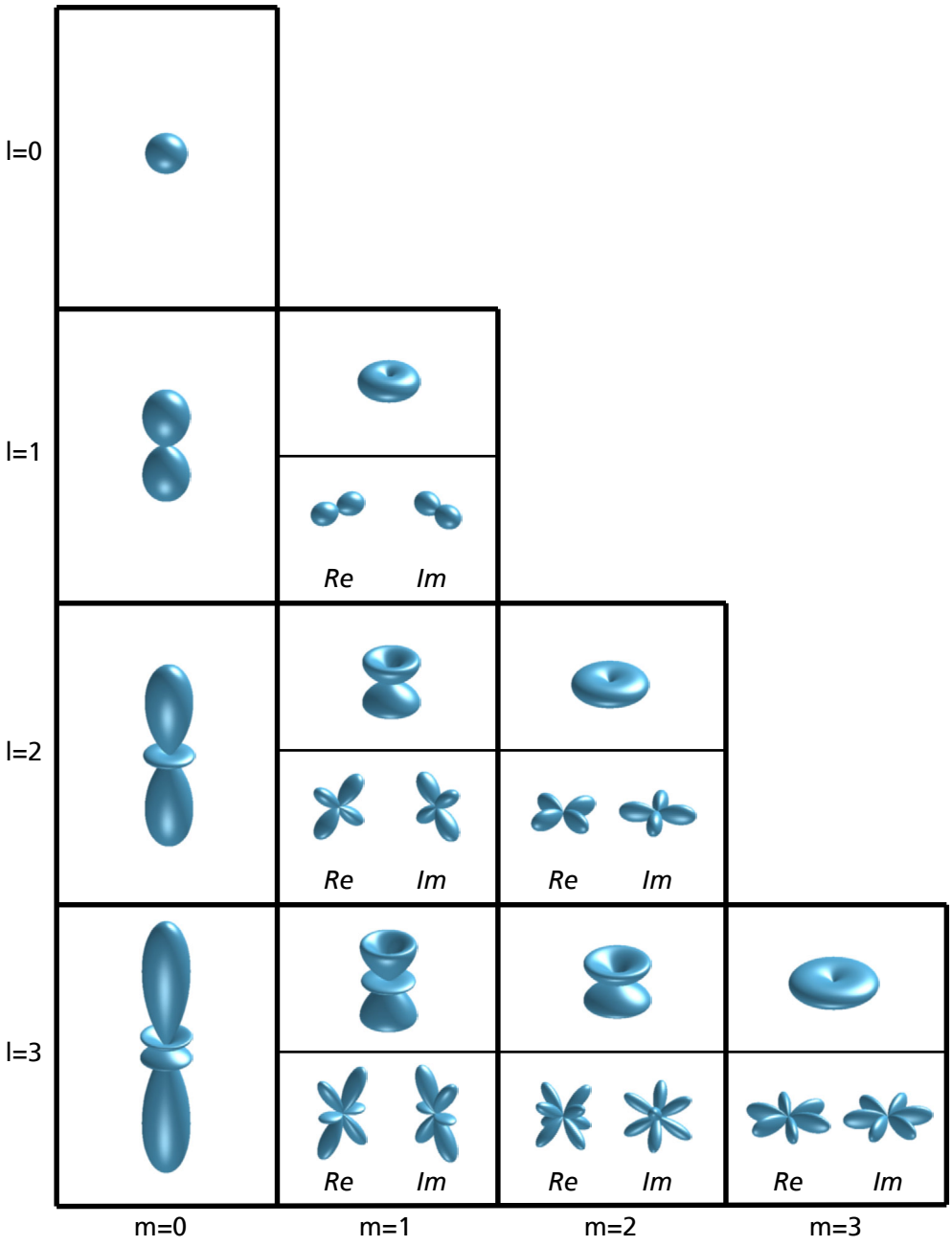

Figure A.1: Spherical Harmonics. $|Y_\ell^m|^2$ are plotted with ℓ growing from 0 (top) to 3 (bottom), and m ranging from 0 (left) to 3 (right). For $m \geq 1$, $Re(Y_\ell^m)^2$ and $Im(Y_\ell^m)^2$ are shown below.

A.2 Canonical Positioning via First-Order Ellipsoid

Brechbühler et al. (1992) describe a way to canonically position objects described by the SPHARM shape descriptor. The procedure is visualized in figure 2.12. First, the original surface is parameterized and sampled on the sphere, followed by a SHT to obtain the coefficients $\mathbf{c}$. The first-order ellipsoid is defined by $\mathbf{c}_1^m$ of the spherical harmonics of degree $\ell = 1$. In Euclidean space, the ellipsoid is defined by

$$\mathbf{f}_1(\theta, \phi) = \sum_{|m| \leq 1} \mathbf{c}_\ell^m Y_\ell^m(\theta, \phi). \tag{A.9}$$

Using Cartesian coordinates

$$u_0 = \sin\theta\cos\phi, \tag{A.10}$$
$$u_1 = \sin\theta\cos\theta, \tag{A.11}$$
$$u_2 = \cos\theta, \tag{A.12}$$

the involved basis functions can be written as explicit expressions:

$$Y_1^{-1} = \frac{\sqrt{3}}{2\sqrt{2\pi}}(u_0 - iu_1), \tag{A.13}$$
$$Y_1^0 = \frac{\sqrt{3}}{2\sqrt{\pi}}u_2, \tag{A.14}$$
$$Y_1^1 = -\frac{\sqrt{3}}{2\sqrt{2\pi}}(u_0 + iu_1). \tag{A.15}$$

f_1 describes an ellipsoid. It can be rotated such that the north pole ($\theta = 0$, on the u_2 axis) will be at one end of the shortest main axis and the point where the Greenwich meridian ($\phi = 0$) crosses the equator ($\theta = \frac{\pi}{2}$, on the u_0 axis) is at one end of the longest main axis. Equation A.9 can be rewritten with the Y_1^m :

$$\mathbf{f}_1(\mathbf{u}) = A\mathbf{u} = A\left(\begin{pmatrix} u_0 \\ u_1 \\ u_2 \end{pmatrix}\right) = \mathbf{a}_1 u_0 + \mathbf{a}_2 u_1 + \mathbf{a}_3 u_2 \tag{A.16}$$

with

$$\mathbf{A} = (\mathbf{a}_1, \mathbf{a}_2, \mathbf{a}_3) = \frac{\sqrt{3}}{2\sqrt{2\pi}}(\mathbf{c}_1^{-1} - \mathbf{c}_1^1, -i(\mathbf{c}_1^{-1} + \mathbf{c}_1^1), \sqrt{2}\mathbf{c}_1^0). \tag{A.17}$$

The three (normalized) eigenvectors $\mathbf{e}_1, \mathbf{e}_2, \mathbf{e}_3$ of the matrix $\mathbf{A}^T\mathbf{A}$, sorted according to their eigenvalues $|\lambda_1| > |\lambda_2| > |\lambda_3|$, build the parameter space rotation matrix $\mathbf{R}_u^T = (\mathbf{e}_1, \mathbf{e}_2, \mathbf{e}_3)$. The spherical mesh parameterization can be rotated to the desired standard position by transforming each vertex with $\mathbf{R}_u$.

For the object space transformation, the main axes of the first-order ellipsoid are needed. Applying $\mathbf{R}_u$ on the coefficients $\mathbf{c}_1^m$ give the new coefficient matrix $\mathbf{A}' = \mathbf{A}\mathbf{R}_u$;

its three column vectors $\mathbf{a}'_1, \mathbf{a}'_2$ and $\mathbf{a}'_3$ are the main axes of the first order ellipsoid. The matrix $\mathbf{A}_n^T$, defined by the orthonormal basis $(\frac{\mathbf{a}'_1}{|\mathbf{a}'_1|}, \frac{\mathbf{a}'_2}{|\mathbf{a}'_2|}, \frac{\mathbf{a}'_3}{|\mathbf{a}'_3|})$, leads to the rotation matrix $\mathbf{A}_n$, which, applied on the original object, positions it such that (after resampling and recalculating the SHT) its first order ellipsoid has the desired canonical position.

Appendix B

Geometry and Statistics

In this appendix, definitions and technical details for a number of operations involving geometry and statistics are given.

B.1 Generalized Least Squares Fitting

To align N_S sets L_i of N_L points such that the sum of squared distances

$$d_i = \sum_{j=1}^{N_L} (L_i(j) - C(j))^2,$$

where $L_i(j)$ is the j^{th} point of L_i, is minimal for all point sets L_i with respect to their mutual mean C, which is called the *consensus*, is an elementary problem for comparative analysis. A popular way to solve it is Gower's algorithm (Gower, 1975), which consists of following steps:

1. All L_i are translated such that each one's center of gravity is at $(0, 0, 0)$.

2. Choose an arbitrary specimen (e.g., L_1) and take it as consensus.

3. Fit all other specimens to the consensus, for instance by applying the algorithm by Horn (1987).

4. Evaluate the consensus as the arithmetic mean of all fitted specimens.

5. Repeat steps 3 and 4 until convergence.

B.1.1 Extension to the Sphere

On the unit sphere, three modifications are necessary:

1. The translation step is dropped.

2. The distances are not euclidean anymore but the length of a great arc segment between the two points.

3. The *spherical consensus* is not the arithmetic mean of the L_i but its projection to the sphere.

In practice, the euclidean distance was used as an approximation of the arc lengths in step 2, and it worked fine.

B.2 Distances Between two Surfaces

In this appendix, two measures for the distance between two discrete 3D surfaces S and S', represented by triangle meshes, are defined. The definitions are based on (Aspert et al., 2002), and their tool MESH[1] was used to measure those distances. The distance $d(p, S')$ between a point p on S and S' is defined as:

$$d(p, S') = \min_{p' \in S'} |p - p'|, \tag{B.1}$$

where $|.|$ is the standard Euclidean norm.

B.2.1 Hausdorff Distance

With the distance function defined above, the *Hausdorff distance* $d_H(S, S')$ is given by:

$$d(S, S') = \max_{p \in S} d(p, S'), \tag{B.2}$$

In general, this distance is not symmetric, i.e., $d(S, S') \neq d(S', S)$. Therefore, the *symmetric Hausdorff distance* is defined as

$$d_{sH}(S, S') = \max[d(S, S'), d(S', S)]. \tag{B.3}$$

It is convenient to express the distance relative to the diagonal of the bounding box of the original surface.

[1] See `http://mesh.epfl.ch` for more information.

B.2.2 Root Mean Square Error

The *root mean square error* $d_{rmse}(S, S')$ between two surfaces S and S' is defined as

$$d_{rmse}(S, S') = \sqrt{\frac{1}{|S|} \iint_{p \in S} d(p, S)^2 dS}. \tag{B.4}$$

Again, a symmetric version, the *symmetric root mean square error*, is defined as

$$d_{srmse}(S, S') = \max[d_{rmse}(S, S'), d_{rmse}(S', S)]. \tag{B.5}$$

B.3 Principal Components Analysis

A common tool to analyze high dimensional data is the principal components analysis (PCA) Jolliffe (1986) which transforms the data into an orthogonal coordinate system such that the greatest variance of the data is along the first coordinate, the second greatest variance along the second coordinate and so on. The coordinates are called *first principal component* (PC1), *second principal component* (PC2) etc. Dimensions which only explain little variance of the sample can be selectively ignored, therefore the PCA is a great tool for dimension reduction and data compression. The first few components typically suffice to visually assess statistically relevant patterns of variation in a sample. However, often it is not easy to understand which geometric features drive the PC in question. A great aid is to invert the coordinate system transformation for points along a PC, therefore visualizing of the patterns of shape change along that PC.

A set of N objects is measured with K measurements. These values are filled into a matrix $\mathbf{X}$ such that each row contains all measurements for one object:

$$\mathbf{X} = \begin{bmatrix} x_{11} & x_{12} & \dots & x_{1K} \\ x_{21} & x_{22} & \dots & x_{2K} \\ \dots & \dots & \dots & \dots \\ x_{N1} & x_{N2} & \dots & x_{NK} \end{bmatrix}. \tag{B.6}$$

$\mathbf{C}$ is a $(N \times K)$ matrix and contains the column-means $\overline{x_i}$ from $\mathbf{X}$

$$\mathbf{C} = \begin{bmatrix} \overline{x_1} & \overline{x_2} & \dots & \overline{x_K} \\ \overline{x_1} & \overline{x_2} & \dots & \overline{x_K} \\ \dots & \dots & \dots & \dots \\ \overline{x_1} & \overline{x_2} & \dots & \overline{x_K} \end{bmatrix}, \tag{B.7}$$

and $\mathbf{D}$ is the "column-centered" version of $\mathbf{X}$ (each column is translated such that the mean of the column becomes zero):

$$\mathbf{D} = \mathbf{X} - \mathbf{C}. \tag{B.8}$$

$\mathbf{D}$ is also called the *observation matrix*. Next, the $(K \times K)$ variance-covariance matrix $\mathbf{S}$ is built

$$\mathbf{S} = \frac{1}{N} \mathbf{D}^T \mathbf{D}. \tag{B.9}$$

Using the eigendecomposition, **S** can be written with eigenvectors **E** and eigenvalues Λ

$$\mathbf{S} = \mathbf{E}\Lambda\mathbf{E}^T. \tag{B.10}$$

The K eigenvectors $\mathbf{e}_k$ are the columns of the $K \times K$ matrix **E**, and Λ is a diagonal matrix:

$$\mathbf{E} = \begin{bmatrix} e_{11} & e_{12} & ... & e_{1K} \\ e_{21} & e_{22} & ... & e_{2K} \\ ... & ... & ... & ... \\ e_{K1} & e_{K2} & ... & e_{KK} \end{bmatrix}; \Lambda = \begin{bmatrix} \lambda_1 & 0 & ... & 0 \\ 0 & \lambda_2 & ... & 0 \\ ... & ... & ... & ... \\ 0 & 0 & ... & \lambda_K \end{bmatrix}. \tag{B.11}$$

The eigenvalues λ_i are ordered such that $\lambda_1 > \lambda_2 > ... > \lambda_K$. The variance explained by PC i is $\frac{\lambda_i^2}{\sum \lambda_i^2}$.

The objects can now be projected onto the eigenvectors to find the PC scores:

$$\mathbf{P} = \mathbf{E}\mathbf{D}^T, \tag{B.12}$$

Element $\mathbf{P}_{ij}$ contains the score of object j for eigenvector, or *Principal Component* (PC) i.

Any point **Q** in PC space can be transformed back to a object **R** in real space:

$$\mathbf{R} = \mathbf{C} + \mathbf{Q}\mathbf{E}^T, \tag{B.13}$$

Appendix C

Taxonomy and Anatomy

This appendix gives background information for non-biologists.

C.1 Family Tree of Hominoids

Figure C.1 shows the (simplified) taxonomic relationships of the four species used in endocranial shape analysis (chapter 6), *Homo sapiens* (modern human), *Pan troglodytes* (chimpanzee), *Pan paniscus* (bonobo) and *Gorilla gorilla* (gorilla). These four *species* belong to three different *genera*. Two species belong to genus *Pan*. Chimpanzees and bonobos are more closely related to each other than to gorillas and humans. Genetic data indicate that *Pan* and *Homo* are more closely related to each other than *Pan* and *Gorilla*.

C.2 Anatomical Expressions

Figure C.2 gives a visual explanation of some basic anatomical terms used to describe locations on the endocranial surface.

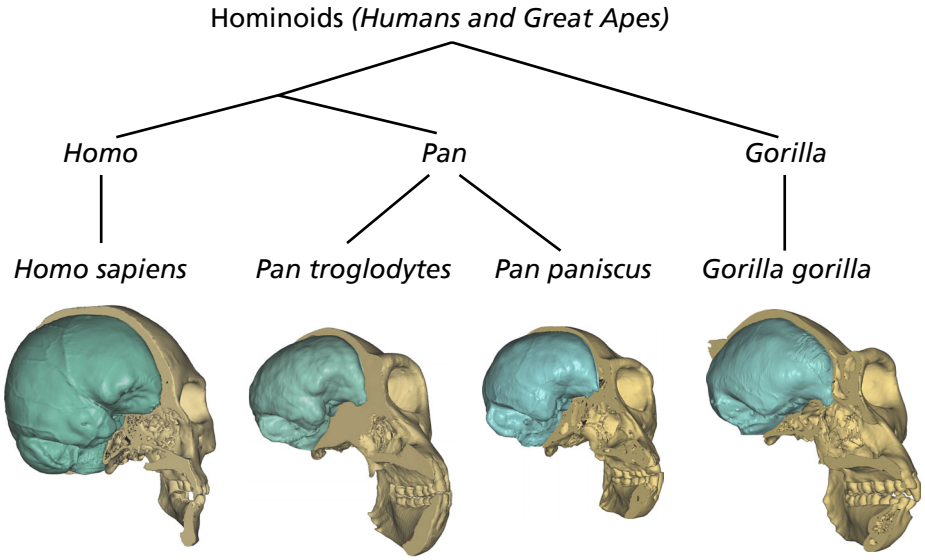

Figure C.1: Simplified diagram of hominoid taxonomy.

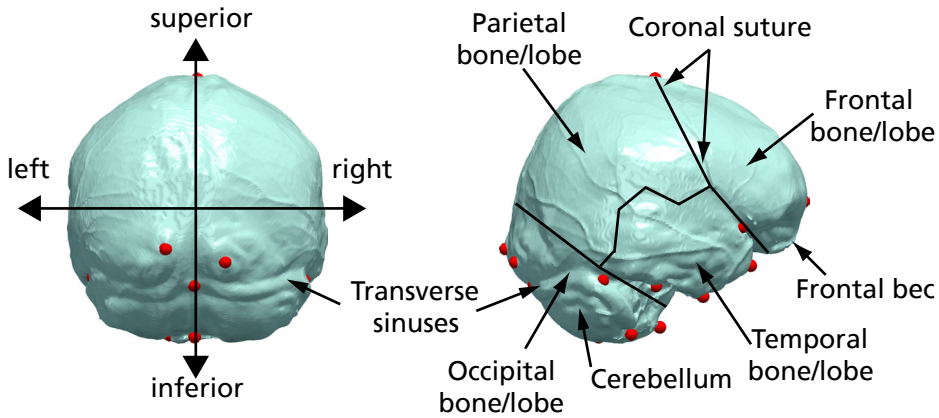

Figure C.2: Basic anatomical terms for describing endocranial positions. Left: Directions (back view). Right: Scheme of bones and some prominent parts.

Appendix D

MorphoTools

Here, some technical details to the MorphoTools framework are presented.

D.1 The MorphoTools Sample File Format

The file format for Morphotools sample files is very simple. It is an ASCII text file with following structure (EBNF-based pseudocode):

Header

```
<sample name>
specimen.type1
{ specimen.type...  }
sampling.  type1
{ sampling.type...  }
{ group <groupname> }
{ attribute <attribute-name> }
{ sattribute <sampling name> <attribut-name> }
```

The `specimen.type` and `sampling.type` are names of actual `Specimen` and `Sampling` implementations, i.e., they must be registered in the MorphoTools factory under the corresponding name. The optional group and attribute entries are defined only for this file. These entries define the structure of the subsequent data entries. The sattribute entries are dependent on the sampling (e.g., they are the names of landmarks).

Data

```
<specimen-name>
<path to specimen.type1 - file>
{ <path to specimen.type...  - file> }
<path to sampling.type1 - file>
{ <path to sampling....  - file> }
{ group-entry }
{ attribute-entry }
```

D.1.1 Example 1

This example demonstrates the usage of three different samplings of the specimens (landmarks, semilandmarks and SPHARM).

```
homo and great apes sample
specimen.surface
sampling.landmarks
sampling.semilandmarks
sampling.sphericalharmonics
group species
group sex
gorilla_AM5563
/morpho/bblower/lm_20/gorilla_AM5563.04.proc_can.obj
/morpho/bblower/lm_20/gorilla_AM5563.04.proc_can.VER
/morpho/bblower/lm_20/sampled/gorilla_AM5563.spherical_ico_lev
/morpho/bblower/lm_20/sampled/gorilla_AM5563.sht_0_255.coeffs
gorilla
female
homo_BD1191
/morpho/bblower/lm_20/homo_BD1191.04.proc_can.obj
/morpho/bblower/lm_20/homo_BD1191.04.proc_can.VER
/morpho/bblower/lm_20/sampled/homo_BD1191.spherical_ico_lev
/morpho/bblower/lm_20/sampled/homo_BD1191.sht_0_255.coeffs
homo
female
pan_paniscus_MRAC26945
/morpho/bblower/lm_20/paniscus_MRAC26945.04.proc_can.obj
/morpho/bblower/lm_20/paniscus_MRAC26945.04.proc_can.VER
/morpho/bblower/lm_20/sampled/paniscus_MRAC26945.spherical_ico_lev
/morpho/bblower/lm_20/sampled/paniscus_MRAC26945.sht_0_255.coeffs
paniscus
male
pan_troglo_AM6839
/morpho/bblower/lm_20/troglo_AM6839.04.proc_can.obj
/morpho/bblower/lm_20/troglo_AM6839.04.proc_can.VER
/morpho/bblower/lm_20/sampled/troglo_AM6839.spherical_ico_lev
/morpho/bblower/lm_20/sampled/troglo_AM6839.sht_0_255.coeffs
pantroglo
male
```

D.1.2 Example 2

Here, using sampling attributes (landmark names) is demonstrated.

```
skulltest
specimen.surface
sampling.landmarks
attribute size
attribute weight
group suborder
group family
group subfamily
sattribute sampling.landmarks   nasion
sattribute sampling.landmarks   mid_nasion-bregma
sattribute sampling.landmarks   bregmaC
sattribute sampling.landmarks   bregmaR
sattribute sampling.landmarks   bregmaL
sattribute sampling.landmarks   mid_bregma-lambdaC
sattribute sampling.landmarks   mid_bregma-lambdaR
Miopithecus talapoin
C:/Renaud/PCA/PCA_bin/Release/mskull/Cra30000.stl
C:/Renaud/PCA/PCA_bin/Release/mskull/_8_8_Miopithecus_scan_72.VER
200
1.2
Anthropoid
Catarhine
Cercopithecid
Avahi occidentalis
C:/Renaud/PCA/PCA_bin/Release/mskull/Avahiocc_skullpos30000.stl
C:/Renaud/PCA/PCA_bin/Release/mskull/_3_3_Avaocc_scan72.VER
331
1.4
Strepsirhine
Lemuriform
Lemur
Adapis parisiensis
C:/Renaud/PCA/PCA_bin/Release/mskull/Avahiocc_skullpos30000.stl
C:/Renaud/PCA/PCA_bin/Release/mskull/_1_1_Adapis_parisiensis_208b.VER
666
6.66
Strepsirhine
Adapiform
Adapine
Leptadapis magnus
```

D.2 Classes in the Repository

Note that these are not conventional classes, but MorphoTools type identifiers. In practice, some identifiers might be mapped to the same class. This is the case for generic classes such as `PCAnalysis`.

```
specimen.surface
sampling.landmarks
sampling.semilandmarks
sampling.sphericalharmonics
controller.sphericalharmonics
view.sampling.sphericalharmonics.reconstruct
view.sampling.sphericalharmonics.coefficients
view.sampling.sphericalharmonics.energy
view.analysis.sphericalharmonics.pca
view.analysis.sphericalharmonics.pcamix
view.analysis.sphericalharmonics.surfmorph
view.analysis.sphericalharmonics.dist
view.analysis.sphericalharmonics.lda
controller.landmarks
view.sampling.landmarks.surface
view.analysis.landmarks.tps
view.analysis.landmarks.pca
view.analysis.landmarks.lda
view.analysis.landmarks.asv
view.analysis.landmarks.shapeperm
view.analysis.landmarks.attrperm
view.analysis.landmarks.casvperm
view.analysis.landmarks.dist
controller.semilandmarks
view.sampling.semilandmarks.surface
view.analysis.semilandmarks.pca
view.analysis.semilandmarks.lda
view.analysis.semilandmarks.surfmorph
view.analysis.semilandmarks.dist
view.analysis.semilandmarks.pcamorph
```

Appendix E

Contents of the CD-ROM

The following documents are found in the top-level directory of the accompanying CD-ROM:

diss.pdf Browseable Acrobat PDF document of this thesis.

ssp Top-level directory containing the full C++ and Java source code for the mesh parameterization and sampling programs and bash scripts described in section 3.

MorphoTools Top-level directory containing the full Java source code of the MorphoTools application framework. Note that this code represents a snapshot as of August 2007.

cgi07 The publication (Specht et al., 2007), as well as the presentation at the Computer Graphics International 2007 conference, including some short movies, can be found in this directory.

References

Adams, D. C., Rohlf, F. J., and Slice, D. E. (2004). Geometric morphometrics: ten years of progress following the 'revolution'. *Italian Journal of Zoology*, 71(1):5–16.

Alexa, M. (2000). Merging polyhedral shapes with scattered features. *Visual Computer*, 16(1):26–37.

Alexa, M. (2002). Recent advances in mesh morphing. *Computer Graphics Forum*, 21(2):173–196.

Andresen, P., Bookstein, F. L., Conradsen, K., Ersboll, B. K., Marsh, J. L., and Kreiborg, S. (2000). Surface-bounded growth modeling applied to human mandibles. *IEEE Transactions on Medical Imaging*, 19(11):1053–1063.

Andresen, P. and Nielsen, M. (2001). Non-rigid registration by geometry-constrained diffusion. *Med. Image Anal.*, 5:81–88.

Arfken, G. B. (1985). *Mathematical Methods for Physicists*. Academic Press.

Asirvatham, A., Praun, E., and Hoppe, H. (2005). Consistent spherical parameterization. *Computational Science ICCS 2005, PT 2*, 3515:265–272.

Aspert, N., Santa-Cruz, D., and Ebrahimi, T. (2002). Mesh: Measuring errors between surfaces using the Hausdorff distance. In *Proceedings of the IEEE International Conference on Multimedia and Expo*, volume I, pages 705 – 708.

Attene, M. and Falcidieno, B. (2006). Remesh: An interactive environment to edit and repair triangle meshes. In *Shape Modeling and Applications, 2006. SMI 2006. IEEE International Conference on*, pages 271–276.

Baylac, M. and Friess, M. (2005). Fourier descriptors, Procrustes superimposition, and data dimensionality: An example of cranial shape analysis in modern human populations. In Slice, D. E., editor, *Modern Morphometrics in Physical Anthropology*, book chapter 6, pages 145–165. Kluwer Academic / Plenum.

Blackith, R. and Reyment, R. (1971). *Multivariate Morphometrics*. Academic Press Inc., U.S.

Bookstein, F. (1989a). Principal warps: Thin-plate splines and the decomposition of deformations. *IEEE Transactions on Pattern Analysis and Machine Intelligence*, 11(6):567–585.

Bookstein, F. (1990). Introduction to methods for landmark data. In Rohlf, F. and Bookstein, F., editors, *Proceedings of the Michigan Morphometrics Workshop*, pages 216–225. Univ. of Michigan Museum of Zoology (Special Publication no. 2).

Bookstein, F. (1996). Combining the tools of geometric morphometrics. In Marcus, L. F., Corti, M., Loy, A., Naylor, G. J. P., and Slice, D. E., editors, *Advances in Morphometrics (NATO Science Series: A:)*. Springer.

Bookstein, F. (1997). Landmark methods for forms without landmarks: morphometrics in group difference in outline shape. *Med. Image Anal*, 1:225–243.

Bookstein, F. (2005). After landmarks. In Slice, D. E., editor, *Modern Morphometrics in Physical Anthropology*, book chapter 2, pages 47–71. Kluwer Academic / Plenum.

Bookstein, F., Schafer, K., Prossinger, H., Seidler, H., Fieder, M., Stringer, C., Weber, G. W., Arsuaga, J. L., Slice, D. E., Rohlf, F. J., Recheis, W., Mariam, A. J., and Marcus, L. F. (1999). Comparing frontal cranial profiles in archaic and modern Homo by morphometric analysis. *Anatomical Record*, 257(6):217–224.

Bookstein, F. L. (1989b). Size and shape - a comment on semantics. *Systematic Zoology*, 38(2):173–180.

Bookstein, F. L. (1991). *Morphometric Tools for Landmark Data: Geometry and Biology*. Cambridge University Press.

Bookstein, F. L. and Green, W. D. K. (1994). Edgewarp: a flexible program package for biometric image warping in two dimensions. *Visualization in Biomedical Computing, Proc. SPIE*, 2359:135–147.

Botsch, M., Pauly, M., Rössl, C., Bischoff, S., and Kobbelt, L. (2006). Geometric modeling based on triangle meshes. In *SIGGRAPH '06: Proceedings of the conference on SIGGRAPH 2006 course notes*, page 148. ACM Press.

Botsch, M., Steinberg, S., Bischoff, S., and Kobbelt, L. (2002). Openmesh – a generic and efficient polygon mesh data structure. *OpenSG Symposium 2002.*

Brechbühler, C. (1995). *Describtion and analysis of 3-D shapes by parameterization of closed surfaces*. PhD thesis, Swiss Federal Institute of Technology (ETH).

Brechbühler, C., Gerig, G., and Kübler, O. (1992). Surface parametrization and shape description. In *Proc. Visualization in Biomedical Computing VBC'92, Chapel Hill, North-Carolina*, volume 1808, pages 80–89.

Broca, P. (1861). Perte de la parole. ramollisement chronique et destruction partielle du lobe antérieur gauche du cerveau. *Bull Soc Anthrop*, 2:235–238.

Bruner, E. (2004). Geometric morphometrics and paleoneurology: brain shape evolution in the genus Homo. *Journal of Human Evolution*, 47(5):279–303.

Bruner, E., Manzi, G., and Arsuaga, J. L. (2003). Encephalization and allometric trajectories in the genus Homo: Evidence from the Neandertal and modern lineages. *Proceedings of the National Academy of Sciences of the United States of America*, 100(26):15335–15340.

Campagna, S., Kobbelt, L., and Seidel, H.-P. (1998). Directed edges - a scalable representation for triangle meshes. *J. Graph. Tools*, 3(4):1–11.

Chui, H. C. and Damasio, A. R. (1980). Human cerebral asymmetries evaluated by computerized tomography. *Journal of Neurology Neurosurgery and Psychatry*, 43(10):873–878.

Connolly, C. J. (1950). *External morphology of the primate brain*. C.C. Thomas.

Conroy, G., Vannier, M., and Tobias, P. (1990). Endocranial features of australopithecus africanus revealed by 2- and 3-D computed tomography. *Science*, 247(4944):838–841.

Cutting, C., Dean, D., Bookstein, F., Haddad, B., Khorramabadi, D., Zonneveld, F., and McCarthy, J. (1995). A 3-dimensional smooth surface-analysis of untreated crouzons-syndrome in the adult. *Journal of craniofacial surgery*, 6(6):444–453.

de Berg, M., van Krefeld, M., Overmars, M., and Schwarzkopf, O. (2000). *Computational Geometry: Algorithms and Applications, Second Edition*. Springer.

Degener, P., Meseth, J., and Klein, R. (2003). An adaptable surface parameterization method.

Dryden, I. L. and Mardia, K. V. (1998). *Statistical Shape Analysis*. Wiley.

Duchon, J. (1976). Interpolation des fonctions de deux variables suivant le principe de la flexion des plaques minces. *J. R.A.I.R.O. Analyse Numeriques*, 10:5–12.

Eck, M., DeRose, T., Duchamp, T., Hoppe, H., Lounsbery, M., and Stuetzle, W. (1995). Multiresolution analysis of arbitrary meshes. In *Proceedings of ACM SIGGRAPH '95*, pages 173–182.

Falk, D. (1986). Endocranial casts and their significance for primate brain evolution. In Swindler, D. and Erwin, J., editors, *Comparative Primate Biology Vol. 1: Systematics, Evolution, and Anatomy*, pages 477–490. Alan R. Riss, New Yorks.

Falk, D. (1987). Hominid paleoneurology. *Annual Review of Anthropology*, 16:13–30.

Falk, D. (1992). Hominid paleoneurology. In Fleagle, J. and Ciochon, R., editors, *The Human Evolution Source Book*, pages 61–70. Prentice Hall.

Falk, D., Hildebolt, C., Cheverud, J., Kohn, L., Figiel, G., and Vannier, M. (1991). Human cortical asymmetries determined with 3D MRI technology. *Journal of Neuroscience Methods*, 39(2):185–191.

Floater, M. (1997). Parametrization and smooth approximation of surface triangulations. *Comp. Aided Geom. Design*, 14:231–250.

Floater, M. S. and Hormann, K. (2005). Surface parameterization: a tutorial and survey. In Dodgson, N. A., Floater, M. S., and Sabin, M. A., editors, *Advances in Multiresolution for Geometric Modelling*, Mathematics and Visualization, pages 157–186. Springer.

Friedel, I., Schröder, P., and Desbrun, M. (2005). Unconstrained spherical parameterization. In *SIGGRAPH '05: ACM SIGGRAPH 2005 Sketches*, page 134. ACM Press.

Friston, K. J. (1998). Imaging neuroscience: Principles or maps? *Proceedings of the National Academy of Sciences of the United States of America*, 95(3):796–802.

Gerig, G., Styner, M., Jones, D., Weinberger, D., and Lieberman, J. (2001). Shape analysis of brain ventricles using SPHARM. In *Mathematical Methods in Biomedical Image Analysis, 2001. MMBIA 2001. IEEE Workshop on*, pages 171–178.

Geschwind, N. and Levitsky, W. (1968). Human brain: Left-right asymmetries in temporal speech region. *Science*, 161(3837):186–187.

Glaunès, J., Vaillant, M., and Miller, M. I. (2004). Landmark matching via large deformation diffeomorphisms on the sphere. *J. Math. Imaging Vis.*, 20(1-2):179–200.

Gotsman, C., Gu, X., and Sheffer, A. (2003). Fundamentals of spherical parameterization for 3D meshes. *Proceedings of ACM SIGGRAPH '03*, 22(3):358–363.

Gower, J. C. (1975). Generalized Procrustes analysis. *Psychometrika*, 40(1).

Gu, X., Gortler, S. J., and Hoppe, H. (2002). Geometry images. In *SIGGRAPH '02: Proceedings of the 29th annual conference on Computer graphics and interactive techniques*, pages 355–361, New York, NY, USA. ACM Press.

Gu, X., Wang, Y., Chan, T. F., Thompson, P. M., and Yau, S.-T. (2004). Genus zero surface conformal mappings and its application to brain surface mapping. *IEEE Transactions on Medical Imaging*, 23(8):949–958.

Gu, X. and Yau, S. (2002). Computing conformal structures of surfaces. *Communications in Information and Systems*, 2:121–146.

Gu, X. and Yau, S.-T. (2003). Global conformal surface parameterization. In *SGP '03: Proceedings of the 2003 Eurographics/ACM SIGGRAPH symposium on Geometry processing*, pages 127–137.

Gunz, P., Mitteroecker, P., and Bookstein, F. L. (2005). Semilandmarks in three dimensions. In Slice, D. E., editor, *Modern Morphometrics in Physical Anthropology*, book chapter 3, pages 73–98. Kluwer Academic / Plenum.

Gutman, B., Wang, Y., Lui, L. M., Chan, T., and Thompson, P. (2006). Hippocampal surface analysis using spherical harmonic function applied to surface conformal mapping. In *Pattern Recognition, 2006. ICPR 2006. 18th International Conference on*, pages 994–967.

Haker, S., Angenent, S., Tannenbaum, A., Kikinis, R., Sapiro, G., and Halle, M. (2000). Conformal surface parameterization for texture mapping. *IEEE Transactions on Visualization and Computer Graphics*, 6(2):181–189.

Healy, D., Rockmore, D., Kostelec, P., and Moore, S. (2003). FFTs for the 2-sphere - improvements and variations. *The Journal of Fourier Analysis and Applications*, 9(4):341–385.

Hemmy, D., Zonnefeld, F., Lobregt, S., and Fukuta, K. (1994). A decade of clinical three-dimensional imaging: a review. Part I. Historical Development. *Invest. Radiol.*, 29:489–496.

Holloway, R. (1975). Early hominid endocasts: volumes, morphology, and significance for hominid evolution. In Tuttle, R. H., editor, *Primate Functional Morphology and Evolution (World Anthropology Series)*, pages 393–415. Walter De Gruyter Inc.

Holloway, R. (1978). The relevance of endocasts for studying primate brain evolution. In Noback, C., editor, *Sensory Systems of Primates*, pages 181–200. Plenum Press, New York.

Holloway, R. L. (1981). Exploring the dorsal surface of hominoid brain endocasts by stereoplotter and discriminant analysis. *Philosophical Transactions of the Royal Society of London. Series B, Biological Sciences*, 292(1057):155–166.

Holloway, R. L., Broadfield, D. C., Yuan, M. S., Schwartz, J. H., and Tattersall, I. (2004). *The Human Fossil Record, Brain Endocasts: The Paleoneurological Evidence, Volume 3*. Wiley-Liss.

Hoppe, H. (1996). Progressive meshes. In *SIGGRAPH '96: Proceedings of the 23rd annual conference on Computer graphics and interactive techniques*, pages 99–108. ACM Press.

Hormann, K. and Greiner, G. (2000). MIPS: An efficient global parametrization method. In Laurent, P.-J., Sablonnière, P., and Schumaker, L. L., editors, *Curve and Surface Design: Saint-Malo 1999*, Innovations in Applied Mathematics, pages 153–162. Vanderbilt University Press, Nashville, TN.

Horn, B. K. P. (1987). Closed-form solution of absolute orientation using unit quaternions. *Journal of the Optical Society of America. A*, 4(4):629–642.

Huang, H., Shen, L., Zhang, R., Makedon, F., Hettleman, B., and Pearlman, J. (2005). Surface alignment of 3D spherical harmonic models: Application to cardiac mri analysis. *Medical Image Computing and Computer-Assisted Intervention MICCAI 2005, PT 1*, 3749:67–74.

Jin, M., Wang, Y., Yau, S.-T., and Gu, X. (2004). Optimal global conformal surface parameterization. *vis*, 00:267–274.

Jolliffe, I. (1986). *Principal Component Analysis*. Springer.

Kazhdan, M., Funkhouser, T., and Rusinkiewicz, S. (2003). Rotation invariant spherical harmonic representation of 3D shape descriptors. In *SGP '03: Proceedings of the 2003 Eurographics/ACM SIGGRAPH symposium on Geometry processing*, pages 156–164. Eurographics Association.

Kelemen, A., Székely, G., and Gerig, G. (1997). Three-dimensional model-based segmentation. Technical Report 178, Image Science Lab, ETH Zürich.

Kendall, D. G. (1981). The statistics of shape. In Barnett, V., editor, *Interpreting Multivariate Data (Probability & Mathematical Statistics)*, pages 75–80. John Wiley and Sons Ltd.

Kendall, D. G. (1984). Shape manifolds, procrustean metrics, and complex projective spaces. *Bulletin of the London Mathematical Society*, 16(MAR):81–121.

Kendall, D. G. (1985). Exact distributions for shape of random triangles in convex sets. *Advances in Applied Probability*, 17(2):308–329.

Kettner, L. (1999). Using generic programming for designing a data structure for polyhedral surfaces. *Computational Geometry*, 13(1):65–90.

Klein, R., Liebich, G., and Straßer, W. (1996). Mesh reduction with error control. In *VIS '96: Proceedings of the 7th conference on Visualization '96*, pages 311–318, Los Alamitos, CA, USA. IEEE Computer Society Press.

Kraevoy, V. and Sheffer, A. (2004). Cross-parameterization and compatible remeshing of 3D models. In *Proceedings of ACM SIGGRAPH '04*, pages 861–869.

Krasner, G. E. and Pope, S. T. (1988). A cookbook for using the model-view-controller user interface paradigm in smalltalk-80. *Journal of Object-Oriented Programming*, 1(3):41–&.

Kreyszig, E. (1968). *Differentialgeometrie*. Akademische Verlagsges. Geest u. Portig.

Kuhl, F. P. and Giardina, C. R. (1982). Elliptic fourier features of a closed contour. *Computer Graphics and Image Processing*, 18(3):236–258.

Lambert, J. (1772). *Beyträge zum Gebrauche der Mathematik und deren Anwendung, Band 3*. Buchhandlung der Realschule, Berlin.

Lazarus, F. and Verroust, A. (1998). Three-dimensional metamorphosis: a survey. *Visual Computer*, 14(8-9):373–389.

Lele, S. and Richtsmeier, J. T. (1991). Euclidean distance matrix analysis - a coordinate-free approach for comapring biological shapes using landmark data. *American Journal of Physical Anthropology*, 86(3):415–427.

Lemay, M. (1977). Asymmetries of skull and handedness. Phrenology revisited. *Journal of Neurological Sciences*, 32(2):243–253.

Lestrel, P. E. (1997). *Fourier Descriptors and their Applications in Biology*. Cambridge University Press.

Li, J. and Zhang, H. (2006). Nonobtuse remeshing and decimation. In *Eurographics Symposium on Geometry Processing*, pages 235–238.

Lohmann, G. P. (1983). Eigenshape analysis of microfossils: A general morphometric procedure for describing changes in shape. *Mathematical Geology*, V15(6):659–672.

Loop, C. (1987). Smooth subdivision based on triangle meshes. Master's thesis, Department of Mathematics, University of Utah.

MacLeod, N. (1999). Generalizing and extending the eigenshape method of shape space visualization and analysis. *Paleobiology*, 25(1):107–138.

Maillot, J., Yahia, H., and Verroust, A. (1993). Interactive texture mapping. In *SIGGRAPH '93: Proceedings of the 20th annual conference on Computer graphics and interactive techniques*, pages 27–34, New York, NY, USA. ACM Press.

Meinguet, J. (1979). Multivariate interpolation at arbitrary points made simple. *Zeitschrift für angewandte Mathematik und Physik*, 30(2):292–304.

Mercator, G. (1569). *Nova et aucta orbis terrae descriptio ad usum navigantium emendate accommodata*. Duisburg.

Mosimann, J. (1988). Size and shape analysis. In Kotz, S. and Johnson, N., editors, *Encyclopedia of Statistical Sciences*, pages 219–239. New York: John Wiley & Sons.

Moyers, R. and Bookstein, F. (1979). Inappropriateness of conventional cephalometrics. *American Journal of Orthodontics and Dentofacial Orthopedics*, 75(6):599–617.

Nyquist, H. (2002). Certain topics in telegraph transmission theory. *Proceedings of the IEEE*, 90(2):280–305.

O'Higgins, P. and Jones, N. (1998). Facial growth in cercocebus torquatus: an application of three-dimensional geometric morphometric techniques to the study of morphological variation. *Journal of Anatomy*, 193:251–272.

Owen, R. (1843). *Lectures on Comparative Anatomy and Physiology of the Invertebrate Animals, Delivered at the Royal College of Surgeons in 1843*. London: Longman, Brown, Green & Longman.

Perez, S. I., Bernal, V., and Gonzalez, P. N. (2006). Differences between sliding semi-landmark methods in geometric morphomerics, with an application to human craniofacial and dental variation. *Journal of Anatomy*, 208(6):769–784.

Pilcher, D., Hammock, E., and Hopkins, W. (2001). Cerebral volumetric asymmetries in non-human primates: A magnetic resonance imaging study. *Laterality: Asymmetries of Body, Brain, and Cognition*, 6:165–179(15).

Ponce de León, M. S. and Zollikofer, C. P. E. (2001). Neanderthal cranial ontogeny and its implications for late hominid diversity. *Nature*, 412(6846):534–538.

Praun, E. and Hoppe, H. (2003). Spherical parametrization and remeshing. *Proceedings of ACM SIGGRAPH '03*, 22(3):340–349.

Praun, E., Sweldens, W., and Schröder, P. (2001). Consistent mesh parameterizations. In *Proceedings of ACM SIGGRAPH '01*, pages 179–184.

Ptolemy (1992). *The Geography*. Dover Publications Inc.

Quicken, M., Brechbühler, C., Hug, J., Blattmann, H., and Székely, G. (2000). Parameterization of closed surfaces for parametric surface description. In *IEEE Computer Society Conference on Computer Vision and Pattern Recognition CVPR 2000*, volume 1, pages 354–360. IEEE Computer Society.

Richtsmeier, J. (1993). Beyond morphing: visualisation to predict a child's skull growth. *Advanced Imaging*, July:24–27.

Richtsmeier, J. and Chevrud, J. (1986). Finite-element scaling analysis of human craniofacial growth. *Journal of Craniofacial Genetics and Development Biology*, 6(3):289–323.

Richtsmeier, J. and Lele, S. (1990). Analysis of craniofacial growth in crouzon syndrome using landmark data. *Journal of Craniofacial Genetics and Developmental Biology*, 10(1):39–62.

Richtsmeier, J. and Lele, S. (1993). A coordinate-free approach to the analysis of growth-patterns: models and theoretical considerations. *Biological Reviews of the Cambridge Philosophical Society*, 68(3):381–411.

Richtsmeier, J. T., Cole, T. M., Krovitz, G., Valeri, C. J., and Lele, S. (1998). Preoperative morphology and development in sagittal synostosis. *Journal of Craniofacial Genetics and Developmental Biology*, 18(2):64–78.

Richtsmeier, J. T. and Walker, A. (1993). A morphometric study of facial growth. In Walker, A. and Leakey, R., editors, *The Nariokotome Homo erectus Skeleton*. Cambridge: Harvard University Press.

Riemann, B. (1851). *Grundlagen für eine allgemeine Theorie der Functionen einer veränderlichen complexen Grösse*. PhD thesis, Universität Göttingen.

Rieppel, O. (1989). Homology, topology and typology: the history of modern debates. In Hall, B. K., editor, *Homology, the Hierarchical Basis of Comparative Biology*, pages 63–100. New York Academic Press.

Rohlf, F. J. (1986). Relationships among eigenshape analysis, Fourier analysis and analysis of coordinates. *Mathematical Geology*, 18(8):845–854.

Rohlf, F. J. (1990). Rotational fit (Procrustes) methods. In Rohlf, F. and Bookstein, F., editors, *Proceedings of the Michigan Morphometrics Workshop*, pages 227–236. Univ. of Michigan Museum of Zoology (Special Publication no. 2).

Rohlf, F. J. and Archie, J. W. (1984). A comparison of Fourier methods for the description of wing shape in mosquitos (diptera, culiciade). *Systematic Zoology*, 33(3):302–317.

Rohlf, F. J. and Marcus, L. F. (1993). A revolution in morphometrics. *Trends in Ecology & Evolution*, 8(4):129–132.

Rohlf, F. J. and Slice, D. (1990). Extensions of the Procrustes method for the optimal superposition of landmarks. *Systematic Zoology*, 39(1):40–59.

Saba, S., Yavneh, I., Gotsman, C., and Sheffer, A. (2005). Practical spherical embedding of manifold triangle meshes. In *Shape Modeling and Applications, 2005 International Conference*, pages 256–265.

Sander, P. V., Snyder, J., Gortler, S. J., and Hoppe, H. (2001). Texture mapping progressive meshes. In *Proceedings of ACM SIGGRAPH '01*, pages 409–416.

Schoenemann, P. T., Gee, J., Avants, B., Holloway, R. L., Monge, J., and Lewis, J. (2007). Validation of plaster endocast morphology through 3D CT image analysis. *American Journal of Physical Anthropology*, 132(2):183–192.

Schreiner, J., Asirvatham, A., Praun, E., and Hoppe, H. (2004). Inter-surface mapping. In *Proceedings of ACM SIGGRAPH '04*, pages 870–877.

Schröder, P., Sweldens, W., Curless, B., and Guskov, I. (2001). Digital geometry processing. In *SIGGRAPH '01: Proceedings of the conference on SIGGRAPH 2001 course notes*. ACM Press.

Schroeder, W., Martin, K., and Lorensen, B. (2003). *The Visualization Toolkit: An Object Oriented Approach to 3D Graphics 3rd Edition*. Kitware, Inc.

Sereno, M. I. (1998). Brain mapping in animals and humans. *Current Opinion in Neurobiology*, 8(2):188–194.

Sheffer, A. and de Sturler, E. (2001). Parameterization of faceted surfaces for meshing using angle-based flattening. *Engineering witth Computers*, 17(3):326–337.

Sheffer, A., Praun, E., and Rose, K. (2006). *Mesh Parameterization Methods and Their Applications*. Now Publishers.

Shen, L., Ford, J., Makedon, F., and Saykin, A. (2004). A surface-based approach for classification of 3D neuroanatomic structures. *Intelligent Data Analysis*, 8:519–542.

Shen, L., Saykin, A., McHugh, T., West, J., Rabin, L., Wishart, H., Chung, M. K., and Makedon, F. (2005). Morphometric analysis of 3D surfaces: appliction to hippocampal shape in mild cognitive impairment. In *6th International conference on computer vision, pattern recognition and image processing in conjunction with 8th joint conference on information sciences (CVPRIP).*

Specht, M., Lebrun, R., and Zollikofer, C. P. E. (2007). Visualizing shape transformation between chimpanzee and human braincases. *The Visual Computer*, 23(9-11):743–751.

Surazhsky, V. and Gotsman, C. (2003). Explicit surface remeshing. In *SGP '03: Proceedings of the 2003 Eurographics/ACM SIGGRAPH symposium on Geometry processing*, pages 20–30. Eurographics Association.

Symington, J. (1916). Endocranial casts and brain form: A criticism of some recent speculations. *Journal of Anatomy and Physiology*, 50:111–130.

Thompson, D. W. (1917). *On Growth and Form*. Cambridge University Press.

Tobias, P. V. (2001). Re-creating ancient-hominid virtual endocasts by CT-scanning. *Clinical Anatomy*, 14(2):134–141.

Toennies, K., Udupa, J., Herman, G., Wornom, I., and Buchman, S. (1990). Registration of 3D objects and surfaces. *Computer Graphics and Applications, IEEE*, 10(3):52–62.

Van Essen, D. (2002). Windows on the brain: the emerging role of atlases and databases in neuroscience. *Current Opinion in Neurobiology*, 12:574–579.

Vilenkin, N. (1968). *Special Functions and the Theory of Group Representations*. Amer Mathematical Society.

Wahba, G. (1990). *Spline Models for Observational Data (CBMS-NSF Regional Conference Series in Applied Mathematics)*. SIAM: Society for Industrial and Applied Mathematics.

Watkins, K., Paus, T., Lerch, J., Zijdenbos, A., Collins, D., Neelin, P., Taylor, J., Worsley, K., and Evans, A. (2001). Structural asymmetries in the human brain: a voxel-based statistical analysis of 142 MRI scans. *Cereb. Cortex*, 11(9):868–877.

Zahn, C. T. and Roskies, R. Z. (1972). Fourier descriptors for plane closed curves. *IEEE Transactions on Computers*, C 21(3):269–&.

Zhou, K., Bao, H., and Shi, J. (2004). 3D surface filtering using spherical harmonics. *Computer-Aided Design*, 36(4):363–375.

Zollikofer, C. P. E. and Ponce de León, M. (2002). Visualizing patterns of craniofacial shape variation in Homo sapiens. *Proceedings of the Royal Society of London B-Biological Sciences*, 269(1493).

Zollikofer, C. P. E. and Ponce de León, M. S. (2000). The brain and its case: computer-based case studies on the relation between software and hardware in living and fossil hominids. In P. V. Tobias, M. A. Raath, J. M.-C. and Doyle, G. A., editors, *Humanity from African Naissance to Coming Millennia*, pages 387–392. Florence University Press.

Zollikofer, C. P. E. and Ponce de León, M. S. (2005). *Virtual Reconstruction: A Primer in Computer-Assisted Paleontology and Biomedicine*. Wiley-Liss.

Zollikofer, C. P. E., Ponce De León, M. S., and Martin, R. D. (1998). Computer-assisted paleoanthropology. *Evolutionary Anthropology*, 6(2):41–54.

Zollikofer, C. P. E., Ponce De León, M. S., Martin, R. D., and Stucki, P. (1995). Neanderthal computer skulls. *Nature*, 375(6529):283–285.